UNIVERSITY OF CALIFORNIA, SAN DIEGO

Ocean dynamics and thermodynamics in the tropical Indo-Pacific region

A dissertation submitted in partial satisfaction of the
requirements for the degree Doctor of Philosophy
in
Oceanography

by

Kyla Drushka

Committee in charge:

Sarah Gille, Chair
Keiko Nomura
Robert Pinkel
Dean Roemmich
Janet Sprintall

2011

The dissertation of Kyla Drushka is approved, and it is acceptable in quality and form for publication on microfilm:

_____

_____

_____

_____

_____

Chair

University of California, San Diego

2011

DEDICATION

Dedicated to my grandpa, Norman J. Wilimovsky.

TABLE OF CONTENTS

LIST OF FIGURES

LIST OF TABLES

ACKNOWLEDGMENTS

Sarah Gille and Janet Sprintall have been incredible advisors and mentors, and I have been continually blown away by their dedication, their energy, and their support. Their guidance, encouragement, and constructive criticism have been crucial and inspiring. Thank you.

I am grateful also for the support of the other members of my committee, Dean Roemmich, Rob Pinkel, and Keiko Nomura, as well as former member Paul Linden, who have been generous with their time and ideas. I appreciate that the committee allowed me to leave Scripps for nearly a year in order to work with Susan Wijffels at CSIRO in Tasmania. Susan made Chapter IV of this thesis possible, and I feel so fortunate that I had the opportunity to work with her.

Jim Means, Gordy Stephenson, and Dian Putrasahan were the best office- and hall-mates possible, providing friendship and snacks and regularly coaxing me away from Matlab. I am endlessly grateful to Phil Moses for keeping my computer running, and to Tomomi Ushii for all the logistical help. Thank you also to Becky Burrola and Josh Reeves in the graduate department for helping me to navigate the confusing bureaucracy of UCSD.

Above all, thank you to my crazy and awesome family, and to Caleb, for their nonstop love and support. I adore you!

The text of Chapter II, in its entirety, is a reprint with no modifications to content of the article as it appears in Journal of Geophysical Research - Oceans, 2008, K. Drushka, J. Sprintall, S.T. Gille, and W.S. Pranowo, reproduced by permission of American Geophysical Union. I was the primary researcher and author of this manuscript. Janet Sprintall provided data and directed and supervised the research along with Sarah Gille, and Widodo Pranowo contributed to the field work.

Chapter III, in full, is a reprint with no modifications to content of the article as it appears in Journal of Physical Oceanography, 2010, K. Drushka, J. Sprintall, S.T. Gille, and I. Brodjonegoro, copyright 2010 American Meteorological Society. I was the primary researcher and author of this manuscript, and the co-authors directed and supervised or provided the data for the research which forms the basis for this chapter.

Chapter IV, in full, is a manuscript in preparation for publication in the Journal of Climate. I was the primary researcher and author of this material, with contributions from co-authors Susan Wijffels, Sarah Gille, and Janet Sprintall.

VITA

2004	B.Sc., Physics, McGill University
2011	Ph.D., Physical Oceanography Scripps Institution of Oceanography, University of California, San Diego.

PUBLICATIONS

Drushka, K., S. Wijffels, J. Sprintall, and S. T. Gille, 2011: In situ observations of Madden-Julian Oscillation mixed layer dynamics in the Indian and western Pacific Oceans, in preparation.

Drushka, K., J. Sprintall, S. T. Gille, and I. Brodjonegoro, 2010: Vertical structure of Kelvin waves in the Indonesian Throughflow exit passages. *J. Phys. Oceanogr.*, **40**(9), 1965–1987.

Drushka, K., J. Sprintall, S. T. Gille, and W. S. Pranowo, 2008: Observations of the 2004 and 2006 Indian Ocean tsunamis from a pressure gauge array in Indonesia. *J. Geophys. Res.*, **113**, C07038.

ABSTRACT OF THE DISSERTATION

Ocean dynamics and thermodynamics
in the tropical Indo-Pacific region

by

Kyla Drushka
Doctor of Philosophy in Oceanography
University of California, San Diego, 2011
Professor Sarah T. Gille, Chair

The Indonesian archipelago links the tropical Indian and western Pacific Oceans, so transmission of oceanic and atmospheric energy across the archipelago has the potential to impact both basins. The network of straits and passages within the archipelago provides a conduit for the transmission of ocean signals. To first order, relatively warm, fresh water flows from the Pacific into the Indian Ocean; this is known as the Indonesian Throughflow. Wave energy at a variety of timescales can impact the Indonesian Throughflow, with potential consequences for the entire Indo-Pacific region. Atmospheric signals can also be transmitted across the Indonesian archipelago. For example, the Madden-Julian Oscillation (MJO), a coupled system of strong convective and wind anomalies, propagates eastward from the western Indian Ocean through to the central Pacific Ocean at intraseasonal (30- to 90-day) timescales.

The goal of this research is to characterize some of the ways in which oceanic and atmospheric energy is transmitted through the Indo-Pacific region. This thesis presents results from three studies that use in situ and satellite observations as well as simple models to examine these links. The effect of sub-surface topography is assessed through two studies that examine the properties of wave energy propagating into the Indonesian Throughflow region from the Indian Ocean. Pressure gauge measurements of two tsunamis demonstrate that the complex topography of the archipelago controls the propagation of high-frequency energy through dissipation, reflection, refraction, and resonant amplification. A study of Kelvin waves generated by wind anomalies over the equatorial Indian Ocean uses velocity and temperature measurements within the Indonesian archipelago to show that intraseasonal wave energy is also effectively controlled by bathymetry.

Atmospheric links across the Indonesian archipelago are evaluated through an observational study of MJO dynamics. In situ observations from Argo profiling floats reveal the signature of the MJO on upper ocean temperature and salinity in both the Indian and western Pacific Oceans,

illustrating that the atmosphere is an effective corridor for energy moving eastward over the Indo-Pacific region.

I

Introduction

The western Pacific and Indian Ocean warm pools and how they interact are key to understanding several important modes of climate variability: El Niño-Southern Oscillation, Indian Ocean Dipole, and Madden-Julian Oscillation. These large-scale climate modes are related to variations in temperature and rainfall around the Indian and Pacific Oceans and globally. The unique oceanic connection between the tropical Indian and Pacific Oceans through the Indonesian archipelago has profound consequences for the climate in both basins and within the archipelago itself. There is a mean flow through the archipelago from the western Pacific into the Indian Ocean known as the Indonesian Throughflow (Figure I.1). It is well known that conditions in the western Pacific will affect the tropical Indian Ocean by way of the Indonesian Throughlow (e.g. Gordon and Fine, 1996); however, it is not clear whether the reverse is true. Historically, while the Pacific Ocean has been studied extensively, there have been relatively few measurements in the Indian Ocean and even fewer within the Indonesian archipelago. As a consequence, there are many open questions about how energy – both atmospheric and oceanic – may be transmitted between the tropical Indian and Pacific Oceans across Indonesia. Do variations in the Indian Ocean impact the Pacific Ocean? What are the potential mechanisms for this, and what are the implications for weather and climate? Are there both oceanic and atmospheric links between the two basins, and if so what is the role of air-sea interaction? How do background conditions in both basins impact ocean dynamics? How does the highly complex topography of the Indonesian archipelago influence the energy that passes between the Indian and western Pacific Oceans? In this thesis, I address some of these questions using observations of the ocean and atmosphere as well as simple models. The emphasis is on understanding the roles of air-sea interaction and topography in controlling energy that moves eastward from the Indian Ocean to impact the Indonesian Throughflow region and potentially the western Pacific Ocean.

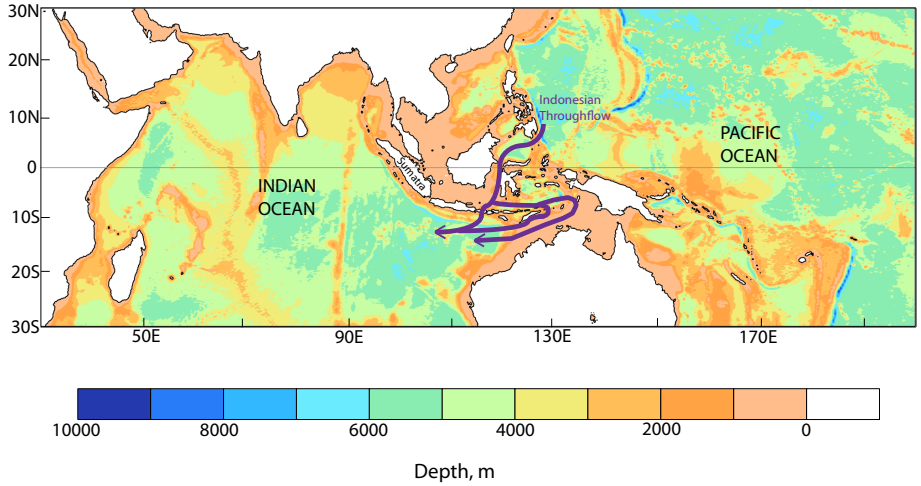

Figure I.1: Tropical Indo-Pacific region. The idealized pathway of the Indonesian Throughflow, which provides the primary oceanic link between the Indian and western Pacific Oceans, is illustrated in purple.

In Chapter II, I examine how high-frequency wave energy propagates through the Indonesian archipelago. This is achieved through a study of two Indian Ocean tsunamis that were recorded by pressure sensors located in three Indonesian Throughflow passages. The observations and results from a linear ray-tracing model demonstrate that the complex topographical features that comprise the Indonesian archipelago exert strong controls on how tsunami energy propagates through the region. This study draws attention to the need for higher-resolution bathymetry data within the archipelago in order to accurately predict local tsunami inundation.

The remainder of the thesis deals with energy on intraseasonal (30- to 90-day) timescales, which is particularly strong in the equatorial band as a result of the Madden-Julian Oscillation (MJO), a coupled pattern of anomalous deep convection and winds that propagates eastward through the Indian and Pacific Ocean basins. Many processes associated with the MJO can affect the dynamics and thermodynamics of the upper ocean. To first order, MJO convective and wind anomalies cool the sea surface and deepen the mixed layer. Anomalous winds can also induce horizontal currents and Ekman pumping, producing anomalous horizontal and vertical advection. Along the equator, zonal wind anomalies associated with intraseasonal variability (including, but not limited to, the MJO) can force Kelvin waves, which produce anomalies in thermocline depth, temperature, and velocity. There is thus a complex set of processes that can act on the upper ocean at MJO time scales, with potentially important implications for air-sea interaction in the tropical Indo-Pacific region.

In Chapter III, I present results from a study of intraseasonal Kelvin waves, which are forced by winds over the central Indian Ocean and propagate eastward along the equator, then poleward along the coast of Indonesia and into the archipelago, where they are steered by sills and other topographical features and can potentially modulate the Indonesian Throughflow. This study uses satellite observations of winds and anomalous sea level in the Indian Ocean to characterize the generation and propagation of numerous Kelvin waves. Temperature and velocity measurements from moorings in two Indonesian Throughflow passages reveal the subsurface signature of the waves. The observed variations at the air-sea interface in the Indian Ocean are linked to the vertical structure of the waves, and the impacts of topography on the horizontal and vertical propagation of Kelvin waves are evaluated. A linear wind-forced model reproduces the intraseasonal Kelvin wave signal well and demonstrates that Indian Ocean Kelvin waves are a superposition of the first two baroclinic modes. The model also reveals that winds off the coast of Sumatra, in addition to winds in the central Indian Ocean, contribute significantly to the observed Kelvin wave signal within the Indonesian archipelago.

Chapter IV addresses the thermodynamical impacts of the MJO in the Indian and western Pacific Oceans. Although the MJO represents an atmospheric rather than an oceanic connection between the two basins, its impacts on the upper ocean are significant. This study is the first use in situ observations to quantify the MJO mixed-layer signal throughout the Indo-Pacific domain. Measurements from Argo profiling floats, as well as a suite of satellite data, are used to construct heat budgets of the ocean mixed layer. The impacts of air-sea processes associated with the MJO – anomalous heat flux, advection, and entrainment – on the heat content of the mixed layer are assessed. The heat budget reveals that anomalous heat flux, which is dominated by variations in solar radiation, is largely responsible for the variations in mixed-layer temperature at MJO timescales. Changes in mixed-layer depth due to the MJO can modulate heat flux forcing, and thus the temperature tendency of the mixed layer. This finding underscores the importance of correctly representing intraseasonal mixed-layer depth variations in model simulations. A comparison of several heat flux products reveals that uncertainties of ocean heat flux estimates at MJO timescales are large, which limits our ability to accurately measure or predict the impacts of MJO forcing on the ocean.

In Chapter V, the thesis is briefly summarized and future directions suggested by this research are discussed.

II

Observations of the 2004 and 2006 Indian Ocean tsunamis from a pressure gauge array in Indonesia

II.1 Abstract

Five shallow pressure gauges located in straits in the southern Indonesian islands were used to evaluate tsunami signals triggered by the earthquakes off the northwest coast of Sumatra in December 2004 and the south coast of Java in July 2006. Tsunami waves reached the pressure gauges around five to six hours after the 2004 earthquake; the largest waves arrived 10 to 23 hours later, with amplitudes ranging from 9 to 25 cm. After the 2006 earthquake, tsunami arrivals were only evident at the Ashmore and Roti pressure gauges in Timor Passage. At these two gauges, the first waves arrived around 2.25 hours after the earthquake and the largest waves arrived two to three hours later, with amplitudes of 6 and 18 cm. Spectral analysis shows an increase of energy in the 40- to 80- min period band during the 2004 tsunami, and at periods of 10 to 20 min in 2006. A simple ray tracing model of both the 2004 and 2006 events, which approximates the tsunami as a shallow water wave, was used to evaluate the effect of topography on tsunami propagation in order to provide a physical explanation for the features observed in the pressure gauge data.

II.2 Introduction

On 26 December 2004 at 00:59 UTC, a magnitude M_W 9.3 earthquake off the west coast of Sumatra (Fig. II.2) generated a tsunami that devastated coastal communities around the Indian Ocean (Stein and Okal, 2005). On 17 July 2006 at 08:19 UTC another, less destructive (M_W 7.7), earthquake occurred about 200 km off the south coast of the Indonesian island of Java (Fujii and Satake, 2006; Lavigne et al., 2007). The 2004 and 2006 earthquakes differed in magnitude, location and source orientation, as well as in the destruction they caused. Here, data from a shallow pressure gauge array in the Indonesian islands are used to compare the tsunami properties during the two events. We evaluate the effect that the complicated bathymetry of the Indonesian archipelago had on the tsunami propagation and the associated wave height, which may help in building an effective tsunami warning system for this region.

Observational and modeling studies have shown that most of the 2004 Sumatra tsunami energy traveled to the west from the earthquake source region (e.g. Kowalik et al., 2005; Merrifield et al., 2005; Nagarajan et al., 2006; Rabinovich and Thomson, 2007). Rabinovich and Thomson (2007) presented records from 45 tide gauges in the Indian Ocean and showed that tsunami amplitudes at stations west of the earthquake epicenter were generally larger than at stations to the east. To the east of the tsunami source region, where our pressure gauge array was located, there were few tide gauges in place and the signal there has not been well documented. Furthermore, many of the tide gauges that recorded the tsunami were located on isolated islands or at other open ocean sites, and thus the signals that they recorded are not necessarily representative of the tsunami magnitude and arrival times within the highly populated Indonesian islands.

The 2004 Sumatra tsunami was modeled by the West Coast/Alaska Tsunami Warning Center (WC/ATWC) (Kowalik et al., 2005). Results from this model are in agreement with the observations of Rabinovich and Thomson (2007), showing primarily westward energy propagation and a relatively weak signal propagating eastward along the south coast of Sumatra and Java (see Fig. II.2). In the Java Sea region, where the average depth is less than 100 m and numerous islands and passages complicate the bathymetry, the tsunami arrival patterns of the WC/ATWC model are extremely convoluted (see Fig. 5 of Merrifield et al., 2005). Because tsunami propagation models rely heavily on accurate bathymetry, they are not guaranteed to perform well where bathymetry is complicated.

Following the 2006 earthquake, Lavigne et al. (2007) measured tsunami runup heights along the south coast of Java. Their results suggest that the tsunami waves propagated eastward from the source region, and that local topography played a large role in determining the local magnitude of the waves. A World Health Organization report tells the same story: most of the damage was confined to central Java, with no casualties west of the earthquake epicenter

(http://www.searo.who.int/LinkFiles/Indonesia_-_Emergency_Situation_Report_ESR_11_3_Aug-06.pdf).

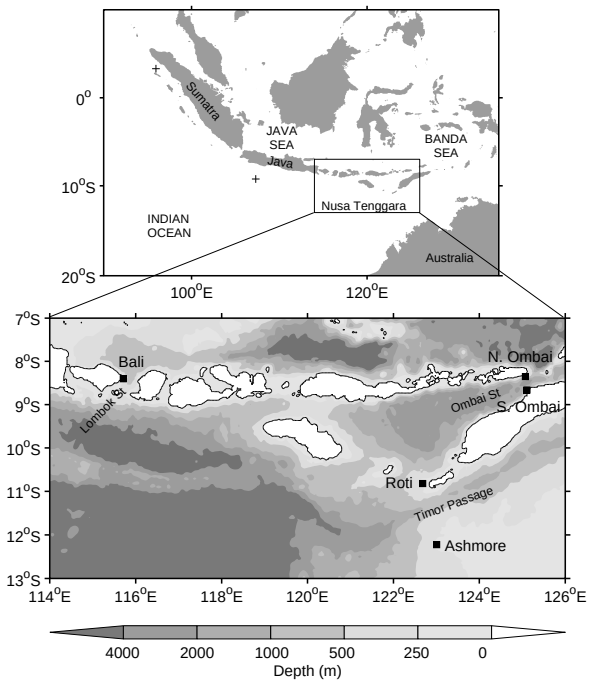

Figure II.1: Study region. Locations of earthquake epicenters are indicated by plus signs west of North Sumatra (December, 2004 earthquake) and south of Java (July, 2006 earthquake) on the top plot. The pressure gauge locations are indicated by squares in the bottom plot. Bathymetric contours are in meters.

In this paper we present data from five shallow pressure gauges that were located in the southern Indonesian island chain of Nusa Tenggara (Java east to Timor) during both the 2004 and 2006 tsunamis. The instruments were situated in narrow straits of varying sill depths, so the tsunami arrivals to the gauges were complicated by effects of bathymetry. The Indonesian archipelago has an enormous population density, mostly in coastal communities vulnerable to the effects of a large tsunami. Although tsunamis are relatively common in the region, their propagation through the thousands of islands and bathymetric features is too complex to model well, and it is therefore difficult to put an effective tsunami warning system in place. The objective of this study is to use the data from pressure gauges located within the Indonesian islands during two distinct tsunami events in order to observe the propagation of high-frequency wave energy through the Indonesian archipelago. The paper is organized as follows: the pressure gauge data set is described in Section 2 and the time series during the tsunamis presented in Section 3; spectral analyses of the pressure

data are given in Section 4; Section 5 contains results from a ray tracing model of the two events; finally, the results are discussed in Section 6.

II.3 Data

The tsunami signals were measured by shallow pressure gauges deployed as part of the International Nusantara STratification ANd Transport (INSTANT) program. INSTANT was a 3-year field program primarily designed to measure the long-term heat and freshwater flux in the Indonesian Throughflow (ITF). The INSTANT array consisted of eleven deep moorings in the major inflow and outflow passages of the ITF, as well as shallow coastal pressure gauges deployed on either side of Timor, Ombai and Lombok outflow passages (Sprintall et al., 2004). The pressure gauges were positioned on either side of these straits to best capture pressure differences across the straits in order to make proxy measurements of geostrophic flow, so it was fortuitous timing that the instruments were deployed during the two tsunami events.

Five pressure gauges were in operation during the tsunamis: these were located off of Bali (Lombok Strait), North Ombai and South Ombai (Ombai Strait), Ashmore Reef and Roti (Timor Passage), as shown in Fig. II.2. The Bali, North Ombai and Roti gauges were deployed in January 2004, and the South Ombai and Ashmore gauges were deployed in August 2003. The Bali, Roti, and North and South Ombai gauges collected data until June 2005, and the Ashmore gauge was retrieved in March 2007. A sixth gauge, on Lombok Island on the eastern side of Lombok Strait, was in place from January 2004 but failed in October 2004 and hence did not capture the tsunami events. The gauges were deployed $\sim$20 to 40 m off the coast of each island in 5 to 10 m water depth. Pressure was recorded every 10 s with 0.3 cm (0.3 mbar) accuracy using Paroscientific pressure sensors. In contrast, tide gauges used in earlier tsunami studies generally had temporal sampling of several minutes to an hour and were an order of magnitude less accurate (Rabinovich and Thomson, 2007). Pressure gauges are able to measure tsunami waves of much smaller magnitudes than those that can be detected with tide gauges (Baba et al., 2004).

Tides are the largest sea level signal in the pressure gauge records from these narrow passages: on average, the tidal component of the pressure gauge signal was order 1 m and the tsunami signal was order 10 cm. Removing the tidal signal from the data was an important and non-trivial step required to isolate the smaller tsunami signal from the data. We compared two methods of detiding the data: the T_Tide program of Pawlowicz et al. (2002) fits sinusoids of the dominant tidal frequencies in a least squares sense to construct a tidal signal that can then be subtracted from the data; the method of Thompson (1983) uses low-pass filters to suppress inertial and tidal frequencies. Using these methods to detide six-month or greater segments of the 10 s pressure data yielded

almost identical results. The Pawlowicz et al. (2002) program was less computationally expensive when processing long time series, and was thus used for the analysis presented here. A Hamming filter was used to compute a 60-minute running mean, which was subtracted from the detided data to remove a periodic signal that the detiding schemes could not capture. We explored running mean window sizes ranging from 30 to 120 minutes and found that the choice did not significantly affect the results.

II.4 Time Series Data

Fig. II.4 shows the pressure anomaly observed at each of the five gauges one day before and two days following the 2004 and 2006 earthquakes. Although the data have been detided, background fluctuations in pressure are large at some stations, and signal-to-noise ratios can be low. This is especially the case at Bali and North Ombai during both tsunami events (Fig. II.4), as well as at South Ombai for the 2006 event (Fig. II.4b): compared to the relatively exposed Roti and Ashmore stations, these gauges were sheltered from the incoming waves generated by the earthquakes, and the tsunami signals are buried in the background noise. To determine the tsunami travel times (Table II.1), a background level of variance at each station was computed from the 24 hours of data before the earthquake. Then, a 25-minute running variance of each detided and low-pass-filtered time series was computed. The travel time was calculated as the difference between the time of the earthquake and the first time that the standard deviation of the time series exceeded 1.5 standard deviations of the background signal.

During the 2004 event, the tsunami waves arrived at the Nusa Tenggara stations during the ebb tide, around four to five hours after the earthquake (Table II.1). Rabinovich and Thomson (2007) note that at tide gauges near the tsunami source region, the largest wave was generally the first to arrive, and farther afield the largest wave arrived later. At the Nusa Tenggara stations, however, the largest waves arrived 10 to 23 hours after the first waves (Table II.1), in spite of the pressure gauges' near proximity to the earthquake epicenter. The more sheltered gauges at Bali and North and South Ombai registered maximum trough-to-crest amplitudes of 9 to 12 cm, compared to 19.5 cm at Ashmore and 24.6 cm at Roti (Table II.1). This is consistent with Indonesian tide gauge data shown by Rabinovich and Thomson (2007), as well as with the peak at Nusa Tenggara seen in the WC/ATWC model results (Kowalik et al., 2005) that arrives around 12 hours following the earthquake after appearing to reflect off of Sri Lanka. The tsunami signals east of the source region were sufficiently small that they could not be distinguished from noise in satellite altimeter data (not shown), in contrast to signals near the source that were clearly visible in altimeter measurements (Gower, 2005; Smith et al., 2005; Hayashi, 2008). Thus using the altimeter measurements we were

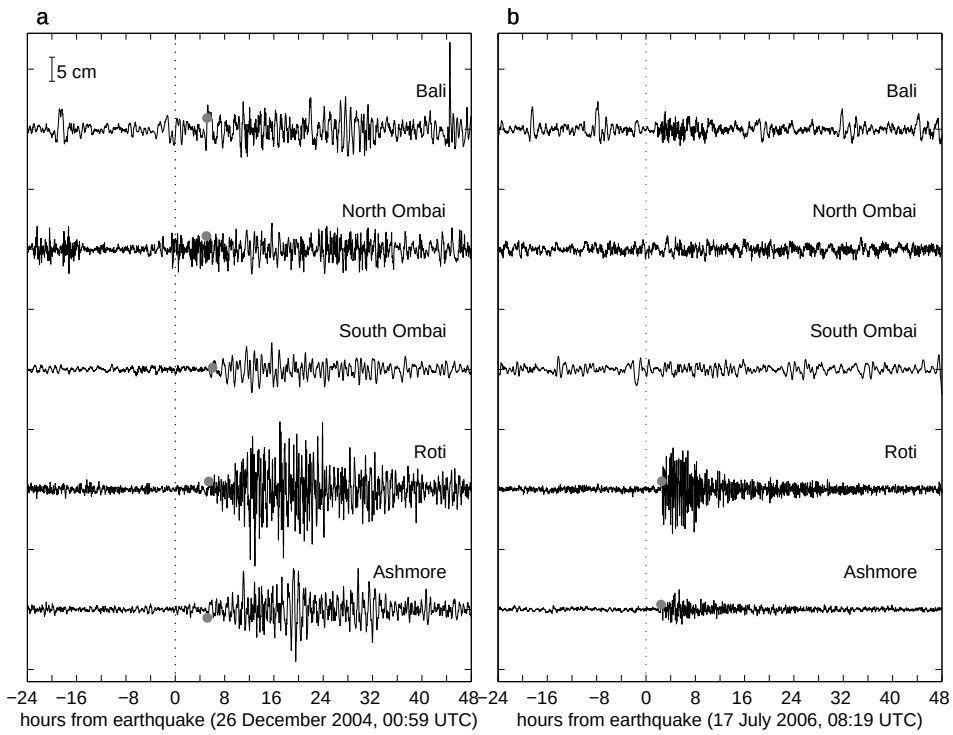

Figure II.2: Detided pressure data, from one day prior and two days following the earthquake (indicated by the dotted line), for the (a) 2004 Sumatra, and (b) 2006 Java earthquakes. Tsunami arrival times, where they could be calculated, are plotted as grey dots. For clarity, the data has been low-pass filtered with a cutoff frequency of 10 cph.

Table II.1: Tsunami observations and model results at pressure gauge sites[a]

Station	Travel Time	Peak Time	Peak Ampl (cm)	Max Energy Period (min)	Ray trace Travel Time
2004 Sumatra tsunami					
Bali	4:58	28:03	12.3	51	–
N. Ombai	4:51	24:35	9.8	80	–
S. Ombai	5:51	15:56	9.3	80	–
Roti	5:13	16:59	24.6	40	–
Ashmore	5:00	19:33	19.3	51	–
2006 Java tsunami					
Bali	–	32:09	6.3	12	1:13 ± :03
N. Ombai	–	9:56	4.7	6	3:13 ± :04
S. Ombai	–	25:54	4.2	15	3:13 ± :04
Roti	2:22	4:24	17.7	18	2:10 ± :06
Ashmore	2:14	5:35	5.9	15	2:14 ± :06

[a] Travel times are in hours:minutes since the earthquake, with blank values indicating that the data was too noisy to determine an accurate travel time. Peak time is the travel time for the largest wave observed; peak amplitude is the trough-to-crest amplitude of this wave (Fig. II.4). Max energy period is the period corresponding to the maximum tsunami energy greater than the background level (Fig. II.5). Ray trace travel time was calculated using the ray tracing model ± the standard deviation computed using 25 point sources for the rays; this column is omitted for the Sumatra event because no rays could be traced to within one degree of any pressure gauge site (Fig. II.6).

unable to identify open ocean propagation of the tsunami towards the Indonesian archipelago.

After the 2006 earthquake, only the Roti and Ashmore pressure gauges measured a significant tsunami signal (Fig. II.4b). The largest wave at Roti arrived two hours after the first wave; the much smaller peak wave seen at Ashmore arrived over three hours after the first (Table II.1). The signal-to-noise ratios are too low to clearly distinguish the tsunami signal at the other stations. At Bali, the closest site to the epicenter of the 2006 earthquake, the tsunami signal appears visible by eye in the time series but the arrival is not distinguishable according to the statistical criteria described above. As during the 2004 tsunami event, no trace of the 2006 tsunami could be detected in satellite altimetry measurements near Nusa Tenggara.

There are differences in the signals at North and South Ombai during both the 2004 and the

2006 events, noteworthy because the stations are close together. In the 2004 event, the background is noisier at North Ombai and the tsunami signal is ambiguous in comparison to that at South Ombai (Fig. II.4a). In 2006, tsunami signals are not readily apparent at either gauge, but there are generally more high-frequency fluctuations at North Ombai (Fig. II.4b). Ombai Strait, 35 km wide and 2700 m deep between the gauges, is a major outflow passage for the ITF (Chong et al., 2000; Potemra et al., 2003). The south side of the strait is steeply sloped in comparison to the north side, which has a shallow shelf running several kilometers offshore (see Fig. II.5 of Molcard et al., 2001). Moorings deployed on either side of Ombai Strait as part of INSTANT show that the main ITF is strongly trapped to the southern side of the strait (not shown). The discrepancy between the two pressure gauges during the tsunamis is likely due in part to a combination of ITF dynamics and topographic effects.

II.5 Spectral Energy

Fig. II.5 shows comparisons of spectral energy at each station before and during the 2004 and 2006 tsunamis. The background spectra were formed from the seven days of data before the tsunami (60480 data points) and the tsunami spectra were computed from the two days following the first wave arrival (17280 data points). A 12-hour Kaiser-Bessel window with 50% overlap was used, giving 54 and 14 degree-of-freedom spectral estimates for the background and tsunami data, respectively. For the 2004 event (Fig. II.5a), the tsunami energy at every location is significantly higher at low frequencies than the pre-tsunami energy. At high frequencies (not shown) the tsunami energy is similar to, although slightly lower than, the background. The tsunami energy peaks have periods of 40 to 80 min (Table II.1). For the 2006 Java event (Fig. II.5b), the background and tsunami energy are statistically indistinguishable at all stations except Roti, which has several large tsunami peaks at frequencies higher than 2 cph, and Ashmore, which shows consistently high tsunami energy at frequencies higher than 2 cph. A comparison of the 2004 and 2006 Roti spectra shows peaks of the same frequencies (e.g. periods of 23 and 40 min) with different relative magnitudes for the two events. For both events, the background and tsunami spectra have similar shapes at most stations, suggesting that the tsunami signal is a resonant amplification of the normal background response to the local topography (cf. Van Dorn, 1984). Because the INSTANT pressure gauges were in open, exposed locations rather than in harbors or semi-closed basins, the spectral peaks in the pressure time series are not a result of basin resonant effects such as what might be seen in the case of tide gauges located in harbors. In this sense, the energy peaks of the pressure data are akin to what could be expected from open ocean tide gauges.

To better understand the shift in energy suggested by the comparisons of spectra, wavelet

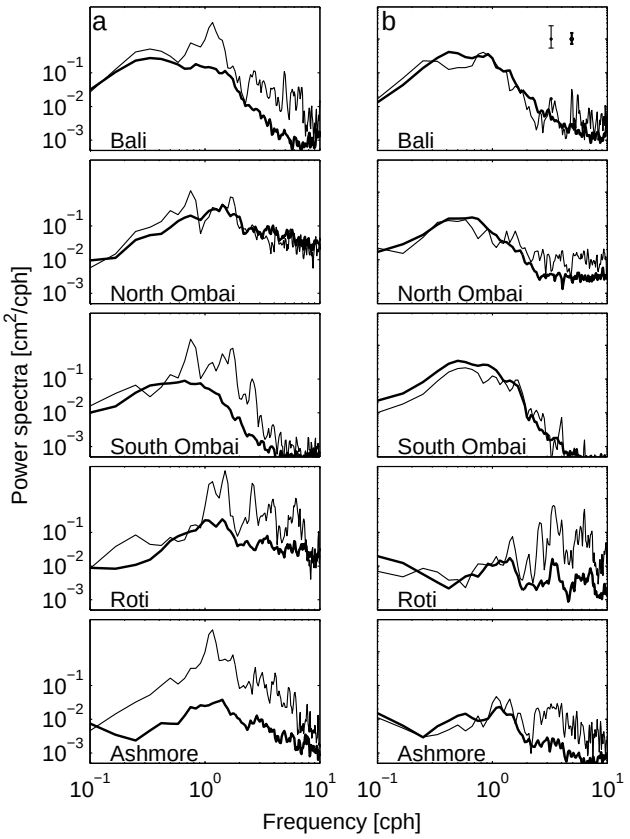

Figure II.3: Power spectra of pressure data comparing spectral energy for the seven days before (thick line) and two days following (thin line) the (a) 2004 Sumatra, and (b) 2006 Java earthquakes. The magnitudes of the uncertainties are indicated in the upper right.

analysis was applied to the data following Torrence and Compo (1998). Fig. II.5 shows the spectrograms (f-t plots) for one day preceding and two days following the 2004 and 2006 earthquakes. Station by station, the spectrogram structures are similar in 2004 and 2006, generally showing the same dominant bands of energy. The f-t plots from the 2004 event (Fig. II.5a) show significant post-earthquake energy in the 15- to 120-minute period band, in agreement with the findings of Rabinovich and Thomson (2007). In their spectrograms of the 2004 tide gauge data, Rabinovich and Thomson (2007) observed distinctive pulses of energy. They suggest that this "wave train" structure results when energy is pumped into local oscillations by topographic refraction and reflection. This structure can be seen at all sites shown in the f-t plots from the 2004 event (Fig. II.5a). For example, the wave train pattern at Bali is similar to that of the nearby Lembar station spectra given by Rabinovich and Thomson (2007, their Fig. 10), showing several distinct trains with the largest waves arriving 28 hours after the earthquake. In contrast, in 2006 the tsunami is not visible in the Bali spectrogram (Fig. II.5b) and the background energy is on the same order as the tsunami across all frequencies.

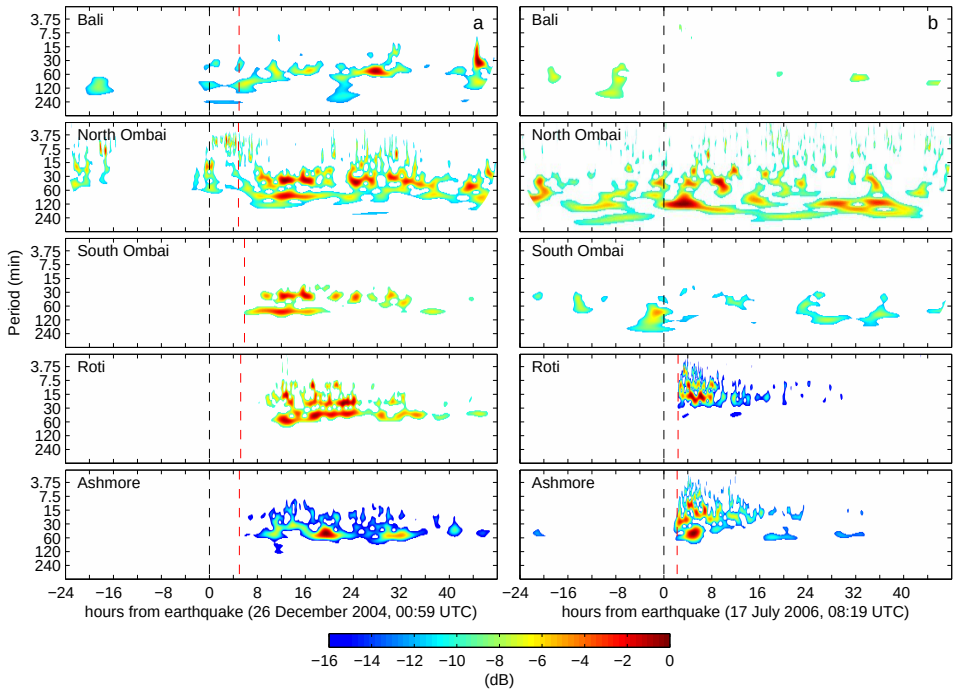

Figure II.4: Spectrograms of detided pressure anomaly data for the (a) 2004 Sumatra, and (b) 2006 Java earthquakes. The power has been normalized to the maximum power for each plot; areas with less than 95% significance have been masked out. The earthquake time is indicated with a black dashed line and the observed arrival time, where available (Table II.1), with a red dashed line.

After both the 2004 and 2006 earthquakes, Roti and Ashmore stations received the largest tsunami waves. This is evident from the time series data (Fig. II.4), but can also be seen in the f-t plots (Fig. II.5). For both events, the Roti spectrogram shows no energy at periods longer than around 60 min, and a strong wave train structure is evident; for the 2006 event, the wave trains are narrower in time and the energy falls off more sharply. The energy at Ashmore is strong in the 30- to 60-min period band during both events. The 2006 Ashmore spectrogram shows a surge of high-frequency energy induced by the tsunami around 4 to 6 hours after the earthquake.

In both events, the spectral energy at North Ombai is smeared out widely in frequency and in time, including a significant amount of high-frequency energy. In 2006, the background noise at North and South Ombai is considerable (Fig. II.5b): the energy peak seen at North Ombai just after the earthquake may be a tsunami signal or may be coincidental noise; at South Ombai no trace of the tsunami can be distinguished from the background signal. In 2004, the North Ombai spectrogram (Fig. II.5a) provides information about the tsunami arrival that the time series (Fig. II.4a) alone is unable to provide: the spectral energy is smeared out, but the tsunami can be seen as two significant spikes in energy at periods of 35 min and 70 to 80 min. Although the North and South Ombai time series have substantially different characters, their spectrograms share many features, particularly at the dominant frequencies (periods of 35 min and 70 to 80 min). This suggests that although local topography (e.g. the north versus the south side of Ombai Strait) plays an important role in wave behavior, the properties of the source also have a strong influence on the energy characteristics of the wave (Rabinovich and Thomson, 2007).

II.6 Ray Tracing

To evaluate the effects of topography on tsunami propagation to the pressure gauge sites, we implemented a simple model using the ray tracing equations for seismic surface waves over a sphere (Satake, 1988). The model used a short wavelength approximation and only included the refractive effects of bathymetry, relying on the 30-arcsecond Smith and Sandwell bathymetric grid (http://topex.ucsd.edu). The resolution of the bathymetry was considered too coarse to incorporate reflection into the model with any confidence. Thus, our model will not identify tsunami signals that arrive at the pressure gauges after one or more reflections off of topography, for example after reflection off of Sri Lanka as suggested by the WC/ATWC model of the 2004 tsunami (Kowalik et al., 2005).

More detailed models, such as that of the WC/ATWC, are exceptionally useful for a comprehensive look at wave propagation throughout the oceans as well as for predicting the magnitude of tsunami inundation on land. However, complex models can be computationally expensive to run.

For example, 40 parallel supercomputer processors required 9 hours to run the WC/ATWC model of the 2004 event. In contrast, the ray tracing model provides a simple, fast, computationally cheap and easy-to-implement tool for making estimates of tsunami travel time to a specific location. The integration of the ray tracing equations was done easily on a workstation in just a few hours. In the ray tracing model, individual rays were sent outward from a point source in a limited range of directions towards the gauge locations, allowing travel time estimates to be computed. By sending out rays from numerous point sources located within the tsunami source region, error bars for the travel time estimates could be determined from the ensembles. We evaluated the accuracy of the ray tracing model by comparing its output to observations (Rabinovich and Thomson, 2007) and WC/ATWC model results from the 2004 Sumatra tsunami at several Indian Ocean tide gauge stations (Kowalik et al., 2005). The results from comparing the observed and modeled travel times show that the ray trace model has the same order of accuracy as the WC/ATWC model.

Several studies have shown that the source region for the 2004 tsunami stretched over 1000 km north-northwest of the earthquake epicenter (e.g. Lay et al., 2005; Neetu et al., 2005). Fine et al. (2005) pinpointed two sources for the tsunami waves: the southern source, around 350 km north-northwest of the epicenter, which was responsible for the largest waves; and the northern source, immediately south of the Andaman islands, which was responsible for the smaller waves that hit the northern part of the Bay of Bengal. Fig. II.6a shows the result of tracing out a fan of rays spaced 0.2° apart, from 25 point origins located within the southern source region of the 2004 tsunami defined by Fine et al. (2005). Because of the topography of the Indonesian islands, a direct path could not be traced from the source region to any of the pressure gauges. This is consistent with the pressure signals observed at the gauges: the weak signals at Bali and North Ombai (Fig. II.4a), and the wave trains observed at all stations (Fig. II.5a) suggest that the waves reached the gauges after one or more reflections. The lack of direct paths between the source region and the exact gauge locations made it impossible to predict travel times with any precision using the ray tracing model. We tested the possibility of the peak waves arriving at the Indonesian gauges via reflection off of Sri Lanka by tracing rays westward to the Sri Lankan coast and then southeastward to Indonesia. In this way, the total travel time obtained by the ray trace model was around 12 to 14 hours, consistent with the times at which the first high-energy signal can be seen on the f-t plots (Fig. II.5a).

Using the ray tracing technique was more successful for the 2006 Java event, and lent some insight into the differences in signal that were observed between Roti and Ashmore and the other gauges. Fig. II.6b shows the results of tracing rays outward from 25 points within the source region of the 2006 tsunami as defined by Fujii and Satake (2006), again with 0.2° angular spacing. Numerous rays could be traced directly from the source to the Roti and Ashmore gauge locations: the modeled travel time to Ashmore is the same as the observed travel time, and to Roti the modeled travel time

is within two standard deviations of the observed time (Table II.1). Due to topographical refraction, few rays were able to enter Ombai Strait. The bathymetry did not permit any rays to reach the Bali gauge; the predicted travel time shown for Bali in Table II.1 is for the ray that made it the closest to that gauge (Fig. II.6b).

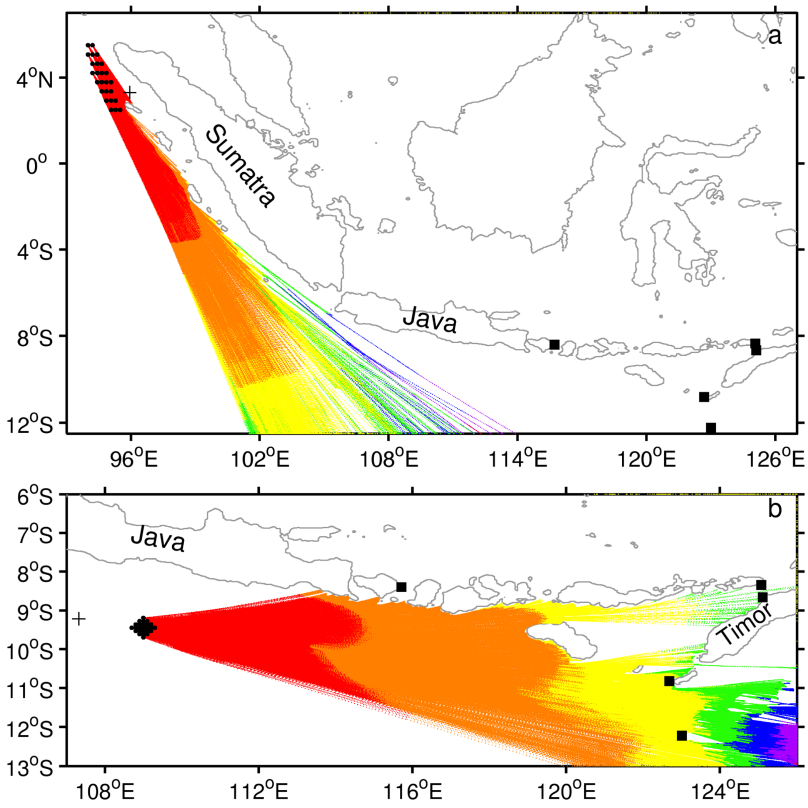

Figure II.5: Results of ray trace model for the (a) 2004 Sumatra, and (b) 2006 Java earthquakes. Rays were sent out with 0.2° angular spacing from 25 point sources (indicated by black dots) within the tsunami source region. Each color transition indicates one hour of ray travel time. The earthquake epicenters are shown as plus signs and the pressure gauge locations as squares. Rays that were sent out in other directions and did not come near to any of the pressure gauge locations have been omitted for clarity.

To evaluate the sensitivity of the ray tracing algorithm to the choice of bathymetry product, we repeated the simulations using the 1-minute gridded General Bathymetric Chart of the Oceans (GEBCO) Digital Atlas published by the British Oceanographic Data Centre. Marks and Smith (2006) compared the GEBCO grid to an older version of the Smith and Sandwell sea floor topography with 2-minute grid spacing (Smith and Sandwell, 1997), and concluded that the Smith and Sandwell product generally resolves details better at the small spatial scales that are relevant for the ray tracing

application. The 30-arcsecond Smith and Sandwell grid used in this study is an improvement over the 2-minute Smith and Sandwell grid discussed by Marks and Smith (2006) and can thus be presumed to perform even better than the 1-minute GEBCO map (Becker, 2008, personal communication). The ray tracing model obtained qualitatively similar results with both bathymetry fields: in neither case did any rays reach the INSTANT gauge locations from the 2004 Sumatra tsunami source region, and the patterns of rays from the simulation of the 2006 Java event were similar. This confirms that even 30-arcsecond bathymetry is too coarse to accurately model the tsunami propagation through a region with such shallow and varied sea floor topography. The travel times estimated using the Smith and Sandwell grid had consistently smaller standard deviations compared to those estimated using the GEBCO bathymetry, suggesting that the Smith and Sandwell 30-arcsecond bathymetry product is superior for this application.

II.7 Conclusions

The pressure gauge measurements show that the 2004 and 2006 tsunamis reached the narrow, shallow passages within the eastern Indonesian archipelago. Despite the relatively close proximity of the gauges to the earthquake epicenters and to one another, the tsunami signals seen in the pressure data (Fig. II.4) have widely varying features, suggesting the importance of local topography in directing the waves. Results from the wavelet analysis also indicate that topography as well as the characteristics of the tsunami source influence how wave energy travels through the passages. High temporal sampling (sampling interval < 1 min) of tide gauges and other instruments designed to measure tsunami signals is vital for capturing high frequency energy. Observations from this study allowed us to gain insight into the travel time and wave height characteristics of tsunamis in a region where models do not resolve the energy pathways well and few tide gauge measurements were available to verify their results.

The ray tracing model confirmed that details of the bathymetry are important for tsunami propagation through the archipelago. However, because the model neglected reflection, diffraction, and nonlinear interactions, it only accurately predicted travel times to stations that were more exposed to the tsunami source region. This simple, fast ray tracing model was shown to produce similar travel time estimates to the more complete WC/ATWC tsunami model, and thus is useful as a “first guess" if computational power and time is limited and if topographical reflection is not thought to be an important factor.

The thousands of islands, passages, and topographical features that make up Indonesia attenuate tsunami signals through reflection and refraction. To improve modeling and prediction efforts, a higher-resolution knowledge of regional bathymetry is necessary.

II.8 Acknowledgments

Funding for this work was provided by NASA-JPL contract 1224031 and NSF grant OCE-0220382.

The text of Chapter II, in its entirety, is a reprint with no modifications to content of the article as it appears in Journal of Geophysical Research - Oceans, 2008, K. Drushka, J. Sprintall, S.T. Gille, and W.S. Pranowo, reproduced by permission of American Geophysical Union. I was the primary researcher and author of this manuscript. Janet Sprintall provided data and directed and supervised the research along with Sarah Gille, and Widodo Pranowo contributed to the field work.

III

Vertical structure of Kelvin waves in the Indonesian Throughflow exit passages

III.1 Abstract

The subsurface structure of intraseasonal Kelvin waves in two Indonesian Throughflow (ITF) exit passages is observed and characterized using velocity and temperature data from the 2004 – 2006 International Nusantara STratification ANd Transport (INSTANT) project. Scatterometer winds are used to characterize forcing, and altimetric sea level anomaly (SLA) data are used to trace the pathways of Kelvin waves east from their generation region in the equatorial Indian Ocean to Sumatra, south along the Indonesian coast, and into the ITF region.

During the three-year INSTANT period, 40 intraseasonal Kelvin waves forced by winds over the central equatorial Indian Ocean caused strong transport anomalies in the ITF outflow passages. Twenty-one of these events are classed as "downwelling" Kelvin waves, forced by westerly winds and linked to depressions in the thermocline and warm temperature anomalies in the ITF outflow passages. Nineteen were "upwelling" Kelvin waves, generated by easterly wind events and linked to shoaling of the thermocline and cool temperature anomalies in the ITF. Both downwelling and upwelling Kelvin waves have similar vertical structures in the ITF outflow passages, with strong transport anomalies over all depths and a distinctive upward tilt to the phase that indicates downward energy propagation. A linear wind-forced model shows that the first two baroclinic modes account for most of the intraseasonal variance in the ITF outflow passages associated with Kelvin

waves, and highlights the importance of winds both in the eastern equatorial Indian Ocean and along the coast of Sumatra and Java for exciting Kelvin waves.

Using SLA as a proxy for Kelvin wave energy shows that 37% ± 9% of the incoming Kelvin wave energy from the Indian Ocean bypasses the gap in the coastal waveguide at Lombok Strait and continues eastward. Of the energy that continues eastward downstream of Lombok Strait, the Kelvin waves are split by Sumba Island, with roughly equal energy going north and south to enter the Savu Sea.

III.2 Introduction

The Indonesian Throughflow (ITF), the flow of water from the Pacific into the Indian Ocean through the narrow passages of the Indonesian archipelago, is an important conduit for mass, heat and freshwater between the two ocean basins. The ITF is thought to impact global circulation of both the ocean (Song et al., 2004) and atmosphere (Schneider, 1998). The ITF is highly variable across a broad range of frequencies, and there is a complicated interplay between locally and remotely forced energy (Wijffels and Meyers, 2004). The variability in the intraseasonal band (30 – 90 days) is particularly striking. Although some intraseasonal energy in the ITF exit passages originates from local and remote Pacific Ocean winds (Qiu et al., 1999; Schiller et al., 2010), the majority of the energy is forced remotely by wind anomalies over the Indian Ocean, which excite Kelvin waves that propagate eastward along the equator to the Indonesian coast and then on into the ITF region as coastally trapped Kelvin waves (Potemra et al., 2002; Wijffels and Meyers, 2004).

Kelvin waves transmit energy downward from the sea surface, so quantifying their subsurface structure (e.g. baroclinic mode number, vertical energy propagation) is critical to understanding how remote Indian Ocean winds affect the ITF interior. The impact that Kelvin waves have on the ITF is largely unknown: the waves travel southeastward along Sumatra and Java, then reach the first significant gap in the coastal waveguide at Lombok Strait (Figure III.1). Theoretical (Durland and Qiu, 2003; Johnson and Garrett, 2006) and modeling (Qiu et al., 1999) studies have demonstrated that nearly all of the incoming intraseasonal Kelvin wave energy should enter Lombok Strait, but *in situ* observations have shown Kelvin wave energy in Ombai Strait (Molcard et al., 2001; Potemra et al., 2002, S09) and a recent modeling effort by Qu et al. (2008) demonstrated the same. Syamsudin et al. (2004) used altimetric data to estimate that 56% of incoming Kelvin wave energy enters Lombok Strait, but the amount of intraseasonal Kelvin wave energy entering Lombok Strait has not been well-quantified with observations. Few *in situ* measurements have captured Kelvin waves in the Indonesian archipelago, and most of these have focused on the semiannual Kelvin waves forced during the monsoon transition seasons in May and November (Arief and Murray, 1996;

Sprintall et al., 1999, 2000; Hautala et al., 2001; Potemra et al., 2002). Little is known about the vertical profile of velocity associated with Kelvin waves (Wijffels and Meyers, 2004), particularly in the Indonesian archipelago, which has many sills, islands, and other topographic features that likely affect local Kelvin wave dynamics (Sprintall et al., 2009, hereafter S09). Sprintall et al. (2000) used data from a pressure gauge array within the ITF outflow straits to observe the passage of a semiannual Kelvin wave; however, this data set provided no information on the vertical structure of the Kelvin waves. Horii et al. (2008) observed the vertical velocity and temperature structures of Kelvin waves in the open ocean at a mooring in the eastern equatorial Indian Ocean, and found a clear pattern of positive and negative velocity and temperature anomalies associated with Kelvin waves forced by periodic Indian Ocean winds.

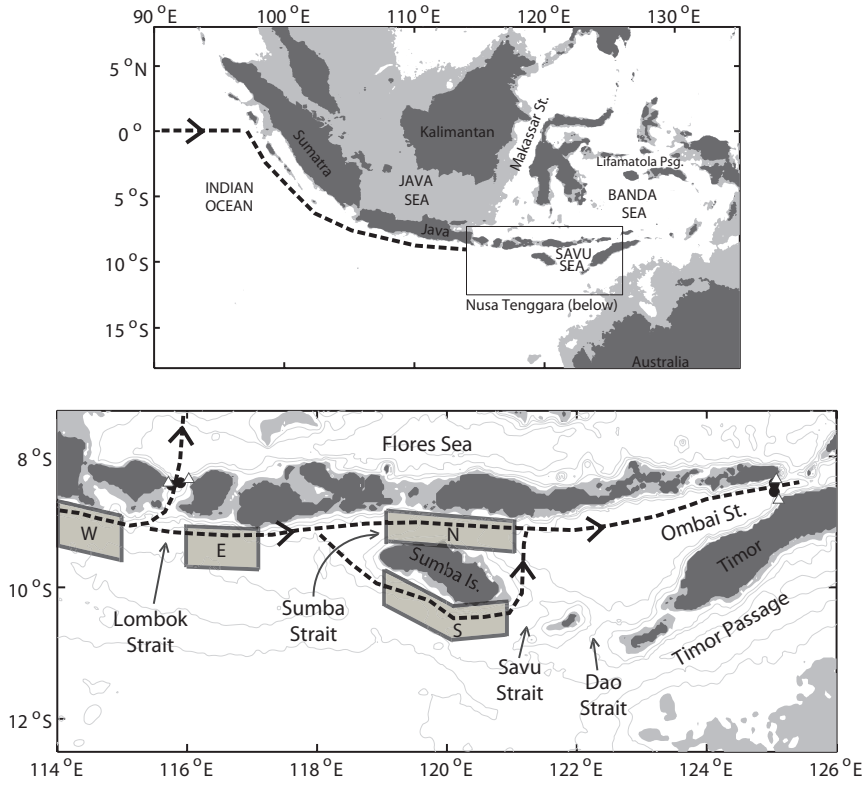

Figure III.1: (Upper panel) Indonesian archipelago. The 0 – 100 m depth is shaded in gray. (Lower panel) Nusa Tenggara region. Lombok and Ombai Strait moorings and pressure gauges with temperature sensors are indicated with circles and triangles, respectively. The 0 – 100 m depth is shaded in gray and the 500-m, 1000-m, 2000-m, and 4000-m contours are drawn in pale gray. The Kelvin wave path is shown as a dashed line. The E and W labels and shading refer to the regions east and west of Lombok Strait; N and S labels refer to the regions north and south of Sumba Island.

In this paper we examine how Kelvin waves propagate through the Indonesian archipelago

by using observations from the International Nusantara STratification ANd Transport (INSTANT) project, a 3-year deployment of moorings and pressure gauges in the straits of Indonesia designed to measure the ITF (Sprintall et al., 2004). This is a unique data set for observing Kelvin waves in this region: INSTANT provides a long time series of full-depth direct current measurements in the ITF outflow passages, for the first time allowing the subsurface structure of Kelvin waves to be observed and characterized in terms of their vertical energy propagation, baroclinic modes, and interaction with topography. Here, we use the INSTANT velocity and temperature measurements made during 2004 – 2006 in two ITF outflow passages – Lombok and Ombai Straits – to characterize the vertical structure of ITF Kelvin waves, their interaction with the regional topography, and their links to Indian Ocean wind forcing. A linear wind-forced model is used to evaluate the hypotheses motivated by the observations.

III.3 Data Sets

III.3.A INSTANT

The aim of the INSTANT project was to make direct full-depth measurements of the velocity and temperature structure of the ITF in order to quantify its mass and heat transports and to understand its variability on intraseasonal, seasonal, and annual time scales (Sprintall et al., 2004). The INSTANT array consisted of eleven deep moorings in the major inflow (Makassar and Lifamatola; see Figure III.1, Gordon et al. (2008), and van Aken et al. (2009)) and outflow (Lombok, Ombai, and Timor) passages of the ITF (S09), plus shallow coastal pressure gauges deployed on either side of each of the outflow passages (Drushka et al., 2008). In this study we use mooring data from Lombok and Ombai Straits. The moorings were deployed in December 2003 – January 2004, recovered and redeployed in June – July 2005, and recovered in November – December 2006. Detailed descriptions of the mooring configuration, deployment, and data processing are given by S09.

The two Lombok Strait moorings were located on each side of the 35 km wide, roughly north-south-oriented passage, in deeper water just north of the 300 m sill (Figure III.1). The two Ombai Strait moorings were located on either side of the 37 km wide, east-west-oriented passage. In both passages the subsurface mooring configurations were similar, with an upward-looking ADCP positioned to capture the surface flow above $\sim$300 m and current meters positioned at discrete depths below. All measurements were objectively mapped onto hourly grids with 10-m depth spacing.

The Lombok West mooring was not recovered in December 2006, and data at this location are only available for the first 18 months of the INSTANT deployment period. However, the complete 3-year time series at Lombok East is available. The first 18 months of data at Lombok East are well

correlated with the measurements from the Lombok West mooring, allowing the second 18 months of data at Lombok West to be predicted from the Lombok East data (see S09 for details).

Transports (Q) were computed by interpolating the along-strait velocities at each time and depth to a cross-strait grid, assuming no-slip conditions at the bottom and side walls, and then summing over the width of the strait to obtain a value of along-strait transport at each time and depth. At each depth, the transport anomaly (Q') was computed with respect to the mean at that depth over the entire time series. S09 used the range of values determined from several different interpolation schemes to provide uncertainties for the transport measurements. They estimated 25 – 30% uncertainty on the total Lombok Strait transports and up to 45% on the Ombai Strait total transport. Here, we use the same interpolation schemes as S09 and calculate the variance of the intraseasonally-bandpassed data for each scheme. Based on this range, we estimate similar uncertainties on the intraseasonal transports: around 25% on the Lombok Strait transports and 45% on the Ombai Strait transports.

It is difficult to maintain surface moorings in the Indonesian straits due to pressures from fishing and other maritime activities, so no temperature or salinity sensors were deployed above 100-200 m. None of the salinity sensors returned viable data so this analysis is restricted to velocity and temperature observations. The width of the straits is much smaller than the Rossby deformation radius in this region (∼100 km), so Kelvin waves are expected to have a similar effect on both sides of the straits and it is reasonable to use a single instrument to quantify the Kelvin wave signal within the strait. This was confirmed: the temperature trends associated with Kelvin waves were the same at both moorings in each strait, and our findings were not sensitive to the choice of mooring that was used to represent the temperature of each strait. We thus used temperatures from the mooring in each strait with the most complete record: 100 m and deeper at Lombok East, and 200 – 1050 m at Ombai North. Coastal temperature sensors deployed in each strait at around 10 m water depth as part of a shallow pressure gauge array (Drushka et al., 2008) were also examined. However, the signals in these data associated with the Kelvin waves were less clear, likely because the measurements were influenced by coastal and tidal processes, and they are not used in this analysis.

III.3.B Other data

Kelvin waves have a sea level anomaly (SLA) signature in the equatorial Indian Ocean on the order of 20 cm (Syamsudin et al., 2004). With phase speeds of 1 – 3 m s^{-1}, they take around 20 days to propagate across the Indian Ocean and around 10 days to travel along the Indonesian coast. Tracking the Kelvin waves eastward along the equator from their generation region and then along coastal Sumatra and Java (Figure III.1) can be accomplished effectively using satellite altimetry.

However, using altimetry to track Kelvin waves east of Lombok Strait, either into the internal Indonesian seas or along Nusa Tenggara, is complicated. The altimetric data are contaminated by land, so it is difficult to observe the Kelvin waves once they reach the many islands and narrow straits that make up the archipelago. There is also significant tidal aliasing of altimeter data at time periods of ∼60 days (Stammer and Wunsch, 1999), which further complicates quantifying intraseasonal signals in regions where the tide models may be imperfect. We explored the possibility that the raw, along-track altimetric sea surface height anomaly data (reference SLA, available from Aviso; Ducet et al., 2000) could offer additional insights compared to the gridded data (Aviso merged, updated SLA). In all of the analyses, there were no significant differences between the two altimetric products. The smoother gridded data are easier to visualize and so those results are presented here. These data are weekly, 0.25° × 0.25° gridded SLA, available for the period from October 1992 to present.

Scatterometer winds were used to observe the forcing of Kelvin waves over the Indian Ocean. We used the Level 3.0 6-hourly gridded data set produced by the Global Modeling and Assimilation Office at the NASA Goddard Space Flight Center. The product uses a variational analysis method to combine data from several satellite missions, and is available globally on a 25 × 25 km grid (Ardizzone et al., 2009).

Indian Ocean temperature and salinity measurements from Argo, available as a gridded product with 30 day × 1° horizontal resolution × 10-100 m vertical resolution, were also used (Roemmich and Gilson, 2009a). These data are too coarse to resolve the propagation of Kelvin waves along their path, but provide a measure of both the background stratification as well as its seasonal and spatial variations.

III.4 Background

III.4.A Wind forcing

Kelvin waves are forced by wind anomalies over the ocean. Westerly wind anomalies produce disturbances that depress the thermocline and thus are commonly referred to as downwelling Kelvin waves. These increase the upper ocean temperature in the eastern part of the basin both by advecting warm water east and by reducing the upwelling of colder water (Giese and Harrison, 1990). In the Indian Ocean, anomalous westerly winds occur at both semiannual and intraseasonal frequencies (Potemra et al., 2002). The mechanisms underlying the forcing at these frequencies are fundamentally different: during the monsoon transition seasons, roughly in May and November, westerly wind anomalies over the central part of the Indian Ocean force a semiannual Kelvin wave, commonly referred to as the Wyrtki jet (Wyrtki, 1973). Independently, intraseasonal westerly

wind anomalies arise from the Madden-Julian Oscillation (MJO), a coupled ocean-atmosphere phenomenon consisting of large-scale patterns of convection that propagate eastward across the Indian and Pacific Oceans (Madden and Julian, 1971; Zhang, 2005). In this study, the semiannual harmonics have been removed from all data in order to restrict the analysis to the intraseasonal Kelvin waves.

Intraseasonal easterly wind anomalies force upwelling Kelvin waves that are manifested as eastward-propagating anomalies that shoal the thermocline depth. The result is a shallow thermocline off the coast of Sumatra, which enhances the upwelling of cool deep water and directly lowers the temperature in the upper layer (Yu and Rienecker, 1999). Thus, oscillating intraseasonal winds over the Indian Ocean are expected to produce alternating warm, downwelling and cold, upwelling Kelvin waves (Masumoto et al., 2005). Cool sea surface temperature (SST) anomalies in the eastern Indian Ocean have been linked to the development of Indian Ocean Dipole (IOD) events (e.g. Yu and Rienecker, 2000; Han et al., 2006; Vinayachandran et al., 2007; Horii et al., 2008). The IOD is characterized by a strong SST gradient across the Indian Ocean, with anomalously cool SSTs seen in the eastern Indian Ocean off Sumatra during its positive phase (Saji et al., 1999). Interannual variations such as the IOD may also affect intraseasonal dynamics of the Indian Ocean (Rao et al., 2007). Although a strong IOD occurred in 2006 during the INSTANT period, the present study is restricted to intraseasonal variability in the ITF; interannual variations and their relationship to intraseasonal Kelvin waves will be the subject of a future study.

III.4.B Kelvin wave vertical structures

Both downwelling and upwelling wind-forced Kelvin waves can be thought of as a superposition of vertical modes that combine in such a way that energy and phase propagate both horizontally and vertically, carrying energy into the ocean interior with a slope that can be predicted by linear inviscid ray theory (McCreary, 1984). We consider our observations in this context in order to (1) assess how well they are described by linear theory; (2) estimate the dominant modal structures of the Kelvin waves; and (3) evaluate the interaction between vertical energy propagation and the topography of the Indonesian archipelago.

From the linearized shallow water equations, each baroclinic mode-n Kelvin wave can be described by

$$\frac{\partial}{\partial z}\left(\frac{1}{N(z)^2}\frac{\partial \psi_n(z)}{\partial z}\right) = -\frac{1}{c_n^2}\,\psi_n(z) \tag{III.1}$$

subject to the boundary conditions

$$\frac{\partial \psi_n(0)}{\partial z} = \frac{\partial \psi_n(H)}{\partial z} = 0 \tag{III.2}$$

and normalized such that

$$\int_{-H}^{0} \psi_n^2(z)\, dz = H, \tag{III.3}$$

where ψ_n is the mode-n vertical structure function; c_n is the phase speed of that mode; *N(z)* is the Brunt-Väisälä frequency, assumed to vary only with depth; and H is the bottom depth (McCreary, 1984; Cane, 1984). Note that ψ represents the horizontal velocity. By solving Eq. (III.1) as an eigenvalue problem for a given stratification *N(z)*, the expected vertical structure and phase speed for each mode can be computed. Here we use the stratification from the gridded Argo temperature and salinity fields: the expected phase speeds for the first three modes are presented in Table III.1, with the mean and standard deviation values based on the range of stratifications observed across the equatorial Indian Ocean (45°E – 99°E, 2°S – 2°N) during the 2004 – 2006 INSTANT deployment period. Table 1 also contains the approximate travel time for each mode to propagate along the coastal waveguide from Lombok to Ombai Strait, based on the phase speed calculated from the stratification in the Nusa Tenggara region (115°E – 125°E, 9°S) and assuming a distance of ∼1050 km between Lombok and Ombai Straits (Figure III.1). The first three vertical structure functions, based on average Indian Ocean stratification, are plotted in Figure III.2: the first baroclinic mode is positive down to 1500 m depth, whereas the second baroclinic mode has a zero crossing at around 200 m. The third mode has zero crossings at around 100 m and 900 m. Although McCreary (1984) suggests that the superposition of many higher-order modes is required for Kelvin wave energy to propagate as a beam of energy into the ocean interior, observations of Pacific and Indian Ocean Kelvin waves have shown that, in practice, only the lowest two or three modes are distinguishable and significant in large-scale Kelvin wave dynamics (e.g., Eriksen et al., 1983; Giese and Harrison, 1990; Cravatte et al., 2003).

Linear ray theory, which arises from the WKB approximation that stratification *N(z)* varies slowly with respect to the vertical wavelength of the wave, states that Kelvin wave energy propagates in the vertical at an angle θ:

$$\theta(z) = \frac{dz}{dx} = \frac{-\omega}{N(z)}, \tag{III.4}$$

where ω is the frequency of the wind forcing. This was first applied to the case of Indian Ocean Kelvin waves by Luyten and Roemmich (1982), who showed that semiannual Kelvin waves forced by winds anywhere in the equatorial Indian Ocean will reach Sumatra in the top 200 m of the water column. Generally, Eq. (III.4) suggests that higher-frequency energy can "dive" deeper than lower frequency energy, and that the further west a Kelvin wave is generated in the equatorial Indian Ocean, the deeper it will have penetrated before reaching a given longitude to the east. This becomes particularly important when considering Kelvin wave propagation through the ITF region, where there are many shallow sills, islands, and bathymetric features that could affect wave dynamics at depth. On the basis of the Argo stratification, Eq. (III.4) predicts that a Kelvin wave at a 45-day

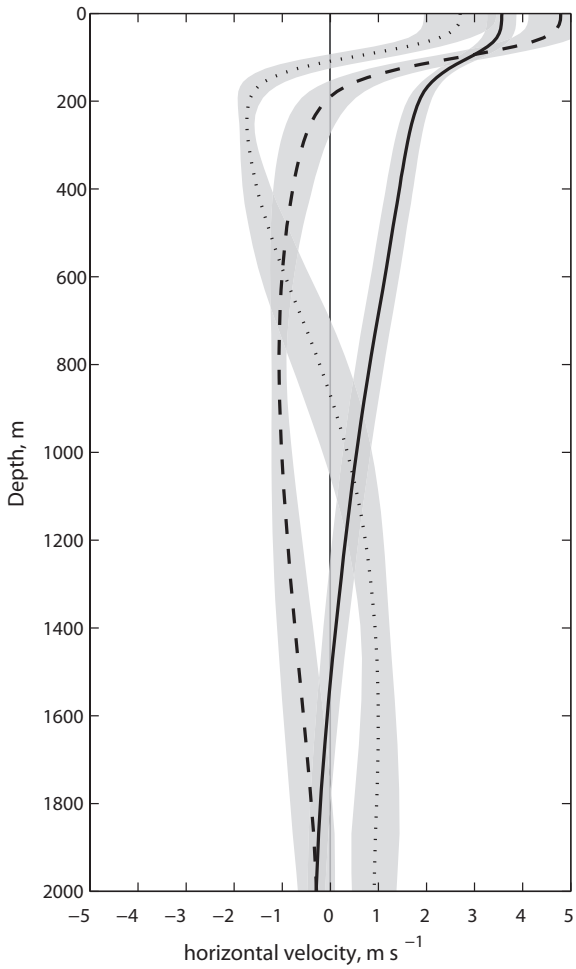

Figure III.2: Theoretical vertical structure functions $\psi(z)$ of Indian Ocean Kelvin waves. The first, second, and third modes are plotted as solid, dashed, and dotted lines, respectively, and 1-σ error bars are shaded. The functions represent horizontal velocity and are normalized according to Eq. (III.1).

period generated at 60°E on the equator in the Indian Ocean will have dived to around 2500 m by the time it reaches Lombok Strait, whereas a wave originating at 85°E will only have reached 1000 m. Kelvin waves generated at 80°E must be forced at periods longer than around 90 days to penetrate no deeper than the 300 m sill depth at Lombok Strait, and at periods longer than around 65 days to penetrate shallower than the ∼900 m sill north of Sumba Island to reach Ombai Strait (Figure III.1).

III.5 Observations of Kelvin Waves

III.5.A Sea level anomalies

Figure III.3a shows a Hövmöller diagram of altimetric SLA over the Indian Ocean and following the Kelvin wave path along the Sumatra and Java coasts (Figure III.1). The annual and semiannual harmonics were removed and the data were bandpassed with a 30- to 90-day filter, revealing a series of coherent eastward-propagating positive and negative SLA signals corresponding, respectively, to downwelling and upwelling Kelvin waves. Generally positive and negative SLA events alternate, consistent with them being forced by periodic winds. Except for their sign, downwelling and upwelling Kelvin waves share similar characteristics in their SLA signals: the magnitude of the SLA signals increases toward the east, consistent with them being forced by a patch of wind with a large fetch, and the largest SLA values are seen along the coast of Sumatra. Further east along the Kelvin wave path in the Nusa Tenggara region (Figure III.1), the SLA signal appears to decrease. This may partly be an artifact of the sparser altimeter data within the Indonesian islands. It may also indicate that the Kelvin wave energy is being dissipated on the topography, reflected, or routed along a different pathway (e.g. northward along the west coast of Sumatra). There are a number of instances of westward-propagating SLA signals east of ∼105°E, for example around February 2006 (Figure III.3a), which are likely Rossby waves that originate as reflected Kelvin waves. These signals propagate at around 0.3 m s^{-1}, consistent with previous observations of Rossby waves in this region (Peter and Mizuno, 2000). The trace of the signals is not seen west of the longitude at which Sumatra and Java meet and there is a bend in the coastal waveguide. This suggests that the reflected Rossby waves travel along the coast of Java and then continue propagating westward into the Indian Ocean at this latitude.

In order to quantify the properties of the individual Kelvin waves, we used an objective procedure to pick each event out of the SLA data based on Figure III.3a. Note that for all of the steps in the extraction of the Kelvin wave signals, the same procedure was used to isolate the downwelling (positive SLA) and upwelling (negative SLA) Kelvin waves. First, the positive and negative SLA peaks at longitude 95°E having an amplitude of at least 1 cm were identified as

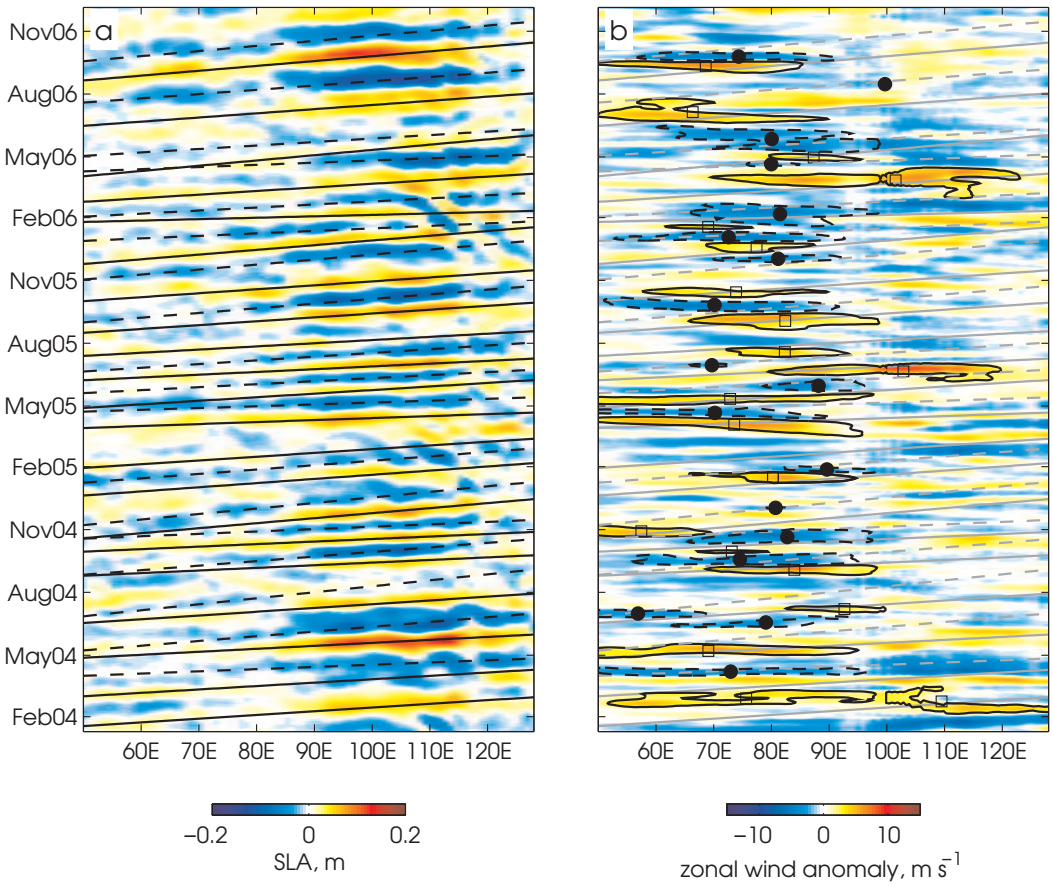

Figure III.3: Time-longitude plots of (a) SLA and (b) anomalous along-shore winds. The x-axis corresponds to longitudes along the path assumed to have been taken by the Kelvin waves (dashed line in Figure III.1). The straight lines show the fits to the Kelvin wave SLA signals, with solid lines indicating downwelling events and dashed lines indicating upwelling events. The contours in (b) indicate the wind signals associated with the Kelvin waves, with westerly wind anomalies (>2 m s^{-1}) contoured with solid lines and easterly wind anomalies (<–2 m s^{-1}) contoured in dashed lines. The center of the westerly and easterly wind bursts are plotted as squares and circles, respectively.

"events". This longitude was used to define the Kelvin wave events because the intraseasonal SLA variability there is high and is well-correlated with signals to the east and west of it, suggesting that SLA at this longitude captures the intraseasonal Kelvin wave effectively. From the SLA peaks at 95°E we identified 22 downwelling and 21 upwelling Kelvin waves during the 2004 – 2006 INSTANT time period. For each of these events, a series of coherent, eastward-propagating SLA peaks with an amplitude of at least 1 cm were identified along the Kelvin wave path, and a line was fit to the SLA peaks in order to estimate the propagation speed and its uncertainty (lines in Figure III.3). The phase speeds estimated from the SLA range from 1.6 to 6.1 m s^{-1}, with an average value of 2.6 $\pm$ 1.0 m s^{-1} (Figure III.4). The phase speeds for downwelling and upwelling events are in agreement. The phase speeds for all events are in a range consistent with Kelvin waves of the first three modes (Table III.1). However, there is not a distinctive separation between the modes, likely because the observed waves are a superposition of two or more modes. In addition, there are limitations on the precision of estimating phase speed from SLA: bandpass-filtering the data, which is necessary to isolate coherent SLA events, erodes the precision of the phase speed estimate. However, the robustness of the phase speed estimates across the set of events, and their agreement with theory, indicates that the range of values is reasonable.

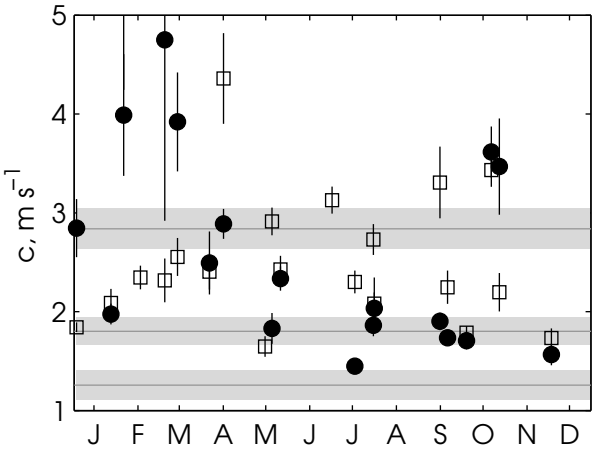

Figure III.4: Kelvin wave phase speeds and uncertainties estimated from SLA for downwelling (squares) and upwelling (circles) events, plotted against month. Error bars are from the linear fit to the SLA data. Horizontal gray areas indicate the theoretical phase speeds for the first three modes of Indian Ocean Kelvin waves, with uncertainties, during the INSTANT time period (Table III.1).

III.5.B Transport observations in the ITF outflow passages

Figure III.5 shows the mean and anomalous transports through Lombok and Ombai Straits. The mean flow through both straits was towards the Indian Ocean, roughly southward in Lombok Strait and westward in Ombai Strait (Figure III.5a,b). Averaged over the INSTANT deployment, the total transports were –2.3 Sv through Lombok Strait (0 – 300 m) and –4.6 Sv through Ombai Strait (0 – 1600 m). Timor Passage (Figure III.1) carried an additional –7.5 Sv (S09), for a total ITF transport of –14.4 Sv toward the Indian Ocean. The anomalous transports were bandpassed with a 20 – 365 day Butterworth filter to remove the high-frequency (primarily diurnal) and interannual signals, and the annual and semiannual harmonic at each depth was removed in order to concentrate on intraseasonal rather than semiannual Kelvin waves.

The transport anomalies (Figure III.5c,d) are highly energetic throughout the water column. In both passages there is strong variability in the mixed layer to ∼100 m depth, likely due to local fluctuations in wind (Schiller et al., 2010). Deeper, there are episodic positive and negative anomalies in the flow through both straits, distinctive events that persist for a few days or longer. Many of the reversals observed in Ombai Strait occur several days after a reversal is observed in Lombok Strait, suggesting features propagating eastward at phase speeds on the order of 1 – 4 m s^{-1}, consistent with low-mode baroclinic Kelvin waves (Table III.1).

Table III.1: The mean theoretical Kelvin wave phase speeds ($\bar{c}$) and standard deviation (σ_c), averaged across the equatorial Indian Ocean and the INSTANT deployment period, for the first three modes. Also given is the approximate time for each Kelvin wave mode to travel from Lombok to Ombai Strait.

n	$\bar{c}$ (m s^{-1})	σ_c (m s^{-1})	Lombok-Ombai time (days)
1	2.83	0.20	4.7
2	1.80	0.14	7.7
3	1.26	0.15	11.8

A lag-correlation analysis confirms that intraseasonal transport anomalies propagate eastward from Lombok to Ombai. Because energy is traveling in the vertical (Eq. III.4) as well as the horizontal, a Kelvin wave transport anomaly that is seen at a certain depth in Lombok Strait may be seen at a different depth in Ombai Strait. Thus although the signals are propagating eastward, a Kelvin wave can be observed earlier at depth in Ombai Strait than nearer the surface in Lombok Strait. The lag-correlation analysis shows that Lombok Strait transport anomalies at 200 m depth lead Ombai Strait transport anomalies at 200 m depth by 7 days, comparable to the travel times expected for low-mode Kelvin waves to travel from Lombok to Ombai Strait (Table III.1). However,

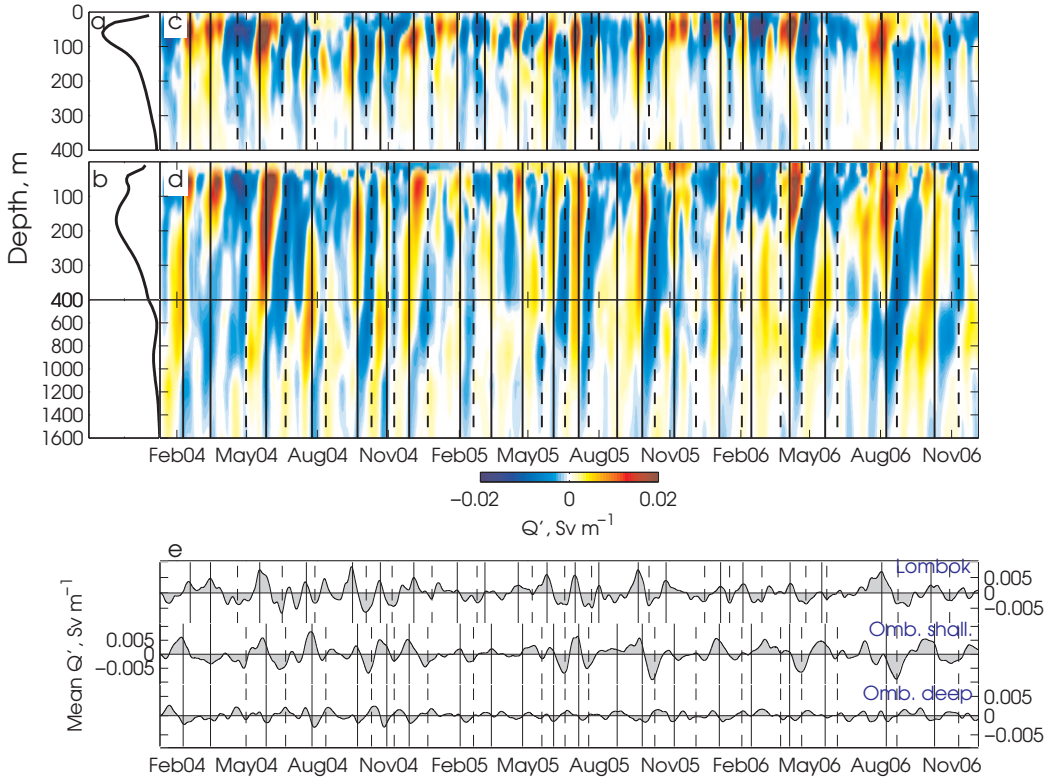

Figure III.5: Mean transports (Sv per unit depth) through (a) Lombok and (b) Ombai Straits; transport anomalies (Sv per unit depth) in (c) Lombok and (d) Ombai Straits; and (e) depth-averaged transports in Lombok (averaged over depths 120 – 250 m) and Ombai shallow (250 – 800 m) and deep (1200 – 1900 m). Negative values indicate ITF outflow. Vertical lines indicate the times the Kelvin waves observed in this study passed through each strait: solid lines denote downwelling waves and dotted lines denote upwelling waves. In Lombok Strait these lines correspond to the peak transport anomaly at 130 m, and at Ombai Strait the lines correspond to the peak at 230 m. Note the two depth scales in (b) and (d).

200-m depth Lombok Strait transport anomalies lead 500-m Ombai Strait transport anomalies by just 1 day; that is, as the Kelvin waves dive, the deep lag-correlated signal reaches Ombai earlier than the shallow signal. This confirms the expectation that energy is propagating vertically, but makes it complicated to use the lags to precisely estimate the phase speed of the Kelvin waves.

To observe subsurface Kelvin wave signatures in the ITF outflow passages, we linked each of the SLA events identified above to a signal in Lombok and Ombai Strait transport anomalies. For each SLA event, the associated transport anomaly peak in each strait was selected with an objective two-step procedure, with positive SLA peaks matched to positive transport anomalies (downwelling Kelvin waves) and negative SLA peaks to negative transport anomalies (upwelling Kelvin waves). First, the line fit to the SLA data was used to predict when each Kelvin wave was expected to arrive at each strait. As discussed above, the subsurface Kelvin wave structure is sloped so there is a time lag between the arrival of the surface and subsurface Kelvin wave signals: for first-mode and second-mode intraseasonal waves, the arrival at 200 – 1000 m depth in the outflow passages should lead the surface arrival by around 2 – 20 days (Eq. III.4). Thus, to match the signals in transport and SLA, we looked for subsurface transport anomaly signals arriving at Lombok and Ombai Straits within the 20-day period preceding the surface SLA signals.

In Lombok Strait, the timing of the events that were defined as Kelvin waves corresponds to the peaks in transport anomalies averaged over depths 120 – 250 m (Figure III.5e). In Ombai Strait, some events only appear in shallower water and some only at depth. Most events are seen throughout the water column, although there is often a discontinuity between the shallow and deep signals (Figure III.5d). As noted by S09, the distinction between the shallow (down to ∼900 m) and deeper (below ∼1200 m) transport anomaly signals in Ombai Strait may be due to the sills north (900 m) and south (1150 m) of Sumba Island, which control the deep flow between Lombok and Ombai Straits (Figure III.1). The deep Kelvin wave energy may be trapped below the 900 m Sumba sill and propagate south rather than north of Sumba Island before reaching Ombai Strait. For this reason, we used two separate depth ranges to identify Kelvin wave reversals in Ombai Strait: 250 – 800 m ("shallow") and 1200 – 1800 m ("deep"). The depth-averaged transport anomalies are shown in Figure III.5e. Of the 43 Kelvin wave events observed in SLA, there were 2 strictly deep events, 17 strictly shallow events, and 21 events with both shallow and deep signals (vertical lines in Figure III.5d,e). Three Indian Ocean SLA events (Figure III.3a) could not be definitively linked to transport events in Lombok and/or Ombai Straits, and have been excluded from the analysis. We considered a total of 40 events, 21 downwelling and 19 upwelling, for the remainder of the study. There are around five transport anomalies in Figure III.5b,d that appear Kelvin wave-like but have not been linked to Indian Ocean SLA events and are not included in this analysis (e.g. positive transport anomaly in August 2004). These signals may be due to energy from local winds

or remotely from Pacific Ocean winds, or they may be Kelvin waves with weak or convoluted SLA signals in the Indian Ocean that were not captured by the scheme we used to identify events.

For both downwelling (positive transport anomaly) and upwelling (negative transport anomaly) events, the upward phase propagation can be seen as a shoaling of the Kelvin wave signal with time in the anomalous transport time series (Figure III.5c,d), particularly at Ombai Strait. This is consistent with the expectation of Kelvin waves forced at the surface to have downward-propagating energy and upward-propagating phase. From Eq. (III.4), the forcing frequency ω can be estimated if the stratification *N(z)* and the angle of propagation θ are known, based on the relationship

$$\omega(z) = -N(z)\,\theta = -N(z)\,\frac{dz}{dx} = -N(z)\,\frac{\frac{dz}{dt}}{\frac{dx}{dt}} = -N(z)\,\frac{\frac{dz}{dt}}{c}. \tag{III.5}$$

The stratification *N(z)* obtained from the Argo data was used with Eq. (III.1) to estimate the phase speed c_n in the Nusa Tenggara region (Figure III.1), and the peak Q' from the transport anomalies for each event (Figure III.5c,d) were used to estimate *dz/dt* at each depth. From Eq. (III.5) we then estimated the average frequency of the wind forcing *ω(z)* for the Kelvin waves at each depth based on the local phase slope and the local stratification, and the mean ω was estimated by averaging over depths 100 – 300 m in Lombok Strait and 200 – 1200 m in Ombai Strait. From the 40 observed downwelling and upwelling events, we estimate from the Lombok Strait transports that the Kelvin waves are forced by winds with a period of 28 ± 15 days, with the uncertainty representing one standard deviation. The Ombai Strait transport anomalies give an estimate that the Kelvin waves are forced by winds with period 46 ± 18 days. These estimates are consistent with intraseasonal wind forcing, albeit with a large uncertainty, suggesting that it is reasonable to use linear theory to describe the upward phase propagation of Kelvin waves observed in the ITF. The discrepancy in the Lombok and Ombai estimates likely results from the difficulty in estimating *dz/dt* in the Lombok Strait signals, which have probably had their structures modified as a result of the topography of Lombok Strait. Note that the estimates are based on the mode-1 phase speed. From Eq. (III.5) it can be see that forcing frequency is inversely proportional to phase speed, so since $c_2/c_1 \sim 0.6$ (Table III.1), the wind forcing period could conceivably be around 60% of these values, which is in the lower range of the intraseasonal band. This method is based solely on the local observations in the ITF passages, and thus represents an independent estimate of the prevailing frequency of Indian Ocean winds that force Kelvin waves.

Composites of the Kelvin wave transport anomalies were constructed by isolating each Kelvin wave in the transport anomaly time series (Figure III.5c,d) and then averaging over the set of events. For each event, t=0 was defined as the time of the peak transport anomaly associated with that event, at 130 m in Lombok Strait and at 230 m in Ombai Strait. Then, the full depth anomaly for the t=±15 days was extracted to give a picture of the depth-time structure. Separate

composites were formed for the set of downwelling events and the set of upwelling events, for both the Lombok and Ombai Strait data (Figure III.6). To evaluate whether the transport anomaly composites for the downwelling and upwelling events were statistically distinct from each other, a Monte-Carlo simulation was performed. Drawing from the 40 available Kelvin wave events, two transport composites were formed for both Lombok and Ombai Strait data, one from a random selection of 21 events and the other from the remaining 19 events. Then the root-mean-squared difference (RMSD) between the pair of composites was used as a metric for "distinctiveness". The test was performed for 1000 random composite pairs and the RMSD values compared to the RMSD of the actual composites for both locations. The RMSD of the downwelling and upwelling transport anomaly composites was found to be greater than the RMSD of the random pair more than 95% of the time, indicating that the differences observed between the downwelling and upwelling waves are significant.

Apart from their signs, the structures of the transport composites of the downwelling and the upwelling events are similar (Figure III.6). The transport anomalies are strongest at depths above the controlling sills in each strait, 300 m in Lombok and 900 – 1150 m in Ombai, as expected for signals arriving from the Indian Ocean (Figure III.1). For both the downwelling and upwelling events, the strongest transport anomalies are seen at around 70 m in Lombok Strait; at this depth, the Kelvin wave transport reversals persist for around 14 days in Lombok Strait and around 20 days in Ombai Strait. The positive transport anomaly of the downwelling events is preceded and followed by negative transport anomalies; similarly, the negative transport signal of the upwelling events is flanked by positive transport anomalies. This is a result of the periodic nature of intraseasonal Kelvin waves; based on each composite representing half a cycle, this points to a forcing period of 28 – 40 days, consistent with the values estimated completely independently from the vertical phase slopes. At Ombai Strait, the distinctive upward Kelvin wave phase propagation seen in the time series is captured in the composites. However, using the phase slope of the composite transport anomalies to estimate the forcing frequency ω yielded values of 15 days (Lombok) – 28 days (Ombai), around half of what was computed from the individual events above. This suggests that the averaging procedure used to form the composites smooths over some of the detail in the vertical structures and that the Kelvin waves vary substantially from one event to the next. Thus, while composites are useful for observing the general subsurface properties of Kelvin waves, the events must be considered individually to understand their dynamics.

The composites presented in Figure III.6 provide a crude estimate of the magnitude of the Kelvin wave transports. We considered each event to be defined by the significant (with respect to the standard error), positive or negative (for downwelling or upwelling events, respectively) portion of its transport anomaly. We then summed over all depths and averaged over the duration of the

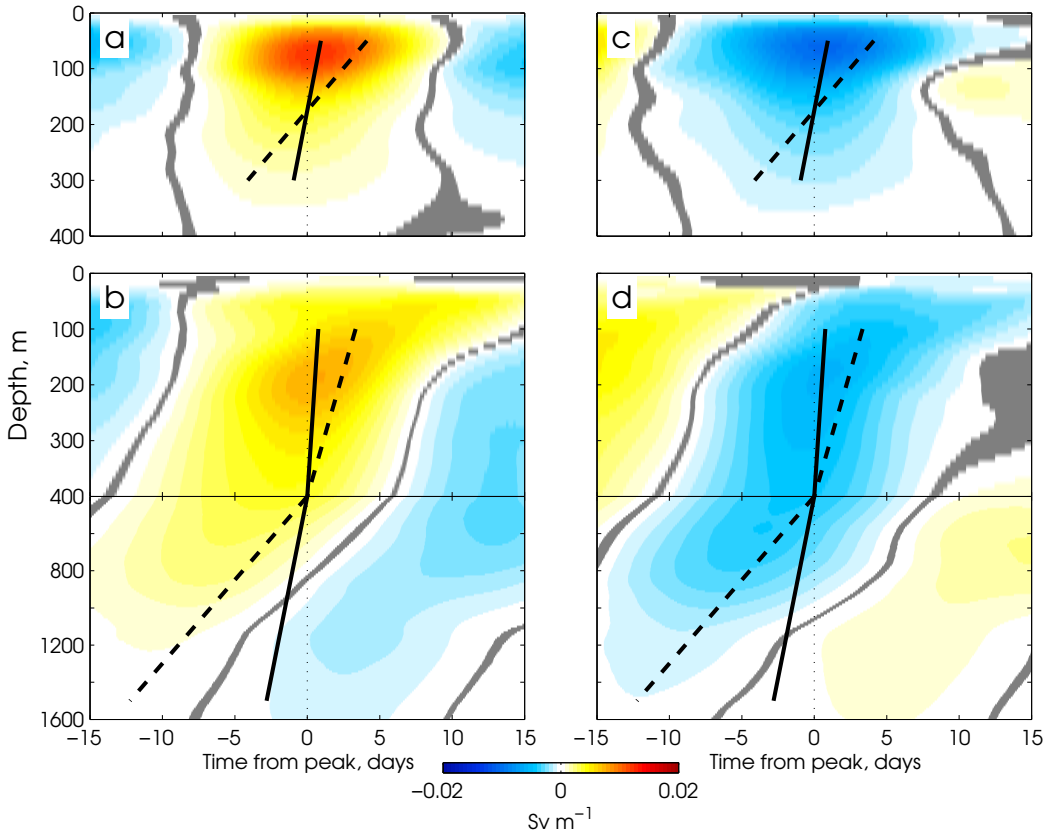

Figure III.6: Composites of transport anomalies (Sv m^{-1}) for downwelling (left; (a) and (b)) and upwelling (right; (c) and (d)) Kelvin waves in Lombok (top; (a) and (c)) and Ombai (bottom; (b) and (d)) Straits. Areas where the mean is less than the standard error have been masked out. The solid and dashed lines represent the approximate phase slope for Kelvin waves forced by winds with periods of 12 days and 54 days, respectively. These value are the minimum and maximum values of the forcing period (mean ± standard deviation) estimated from the transports. Note the two vertical scales in (b) and (d).

event to get an estimate of the transport anomaly associated with each Kelvin wave. The mean and standard deviation of the total Kelvin wave transport anomaly was then computed by averaging over all events. The downwelling events have a transport anomaly of 0.8 ± 0.2 Sv in the top 300 m of Lombok Strait and 2.2 ± 0.2 Sv in the top 1600 m of Ombai Strait. For the upwelling events, the magnitudes of the significant Kelvin wave transports are in agreement, with –0.8 ± 0.2 Sv through Lombok Strait and –2.1 ± 0.2 Sv through Ombai Strait. The errors reported for these estimates only reflect variability over the set of events and not the uncertainty inherent in the method used to compute the transport anomalies.

To diagnose the relative contributions of the baroclinic modes to each wave, we compared the observed Lombok Strait profile of each Kelvin wave transport anomaly to the vertical structure functions (Figure III.2, Eq. III.1). We used two methods to do this: first, fitting the observed transport profiles to the theoretical profiles using a least-squares fit; and second, computing which of the theoretical vertical structure functions accounted for more of the variance of the observations based on their correlation coefficients. These two methods gave consistent results. Of the 21 downwelling and 19 upwelling Kelvin waves, seven of each type of event were dominated by the second baroclinic mode and the rest were dominated by the first baroclinic mode. As expected, the phase speeds of the mode-2 dominated events, as derived from fits to the SLA, are generally lower than those associated with the mode-1 dominated events. Interestingly, all of the mode-2 dominated events occurred during boreal summer (May – October). The reasons for this are unclear, although many studies of equatorial Indian Ocean Kelvin wave dynamics have noted seasonal asymmetries (e.g., Waliser et al., 2003; Iskandar et al., 2005, 2009). Iskandar et al. (2005) suggested that mode-1 Kelvin waves are more efficiently excited in regions where the thermocline is thick, whereas mode-2 waves are more efficiently excited when the thermocline is thin and sharp. However, we see the opposite pattern, with the mode-2 events preferentially forced when the thermocline is deep. Mode-2 is a resonant mode in the Indian Ocean due to the basin geometry (Han, 2005; Fu, 2007); however, the resonance seems to dominate at the 90-day period, substantially longer than we have observed here, so we cannot explain our observations using resonance.

III.5.C Temperature observations in the ITF outflow passages

Figure III.7 shows the anomalous temperature time series at the Lombok East and Ombai North moorings, with the missing surface and deep levels masked out. The data were bandpassed to 20 – 365 days and the annual and semiannual harmonics removed, as for the transport data. Interestingly, the annual temperature signal was about twice as large as the semiannual signal in Lombok Strait, whereas in Ombai Strait the semiannual signal was larger. Intraseasonal temperature variability is strong, with peaks ranging from –2 to +2°C in Lombok Strait (Figure III.7a)

and –1 to +2°C in Ombai Strait (Figure III.7b). From Figure III.7 it can be seen that patterns in the temperature time series are similar to the patterns in the transport time series, with alternating warm and cold events. Thermocline deepening resulting from downwelling Kelvin waves is expected to cause warm temperature anomalies; similarly, upwelling Kelvin waves are expected to be linked to cool temperature anomalies (McCreary, 1983; Yu and Rienecker, 1999; Masumoto et al., 2005). Observational studies have shown that Kelvin wave temperature anomalies generally lag the transport anomalies (e.g. Romea and Allen, 1983; Johnson and McPhaden, 1993).

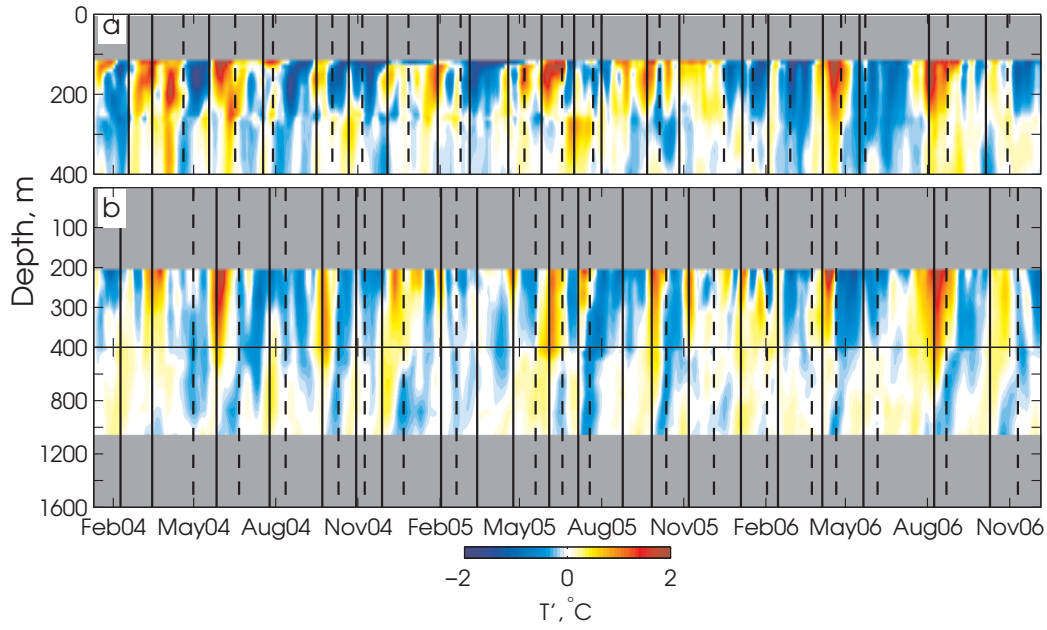

Figure III.7: Anomalous intraseasonal temperatures (°C) in (a) Lombok and (b) Ombai Straits. Depths above the shallowest instrument and below the deepest instrument have been masked out. Vertical lines indicate the Kelvin wave arrivals inferred from the transport observations (Figure III.5): solid (dashed) lines denote downwelling (upwelling) waves. Note the two depth scales in (b).

To explore the relationship between Kelvin wave transport and temperature anomalies, we formed composites of the temperature anomalies associated with the downwelling and upwelling Kelvin waves. For each event, we used the same t=0 that was used for the transport composites, that is, the time of the peak transport anomaly at 130 m in Lombok Strait and at 230 m in Ombai Strait. The composited temperatures at Lombok and Ombai Straits are shown in Figure III.8. If the assumption that Kelvin wave temperature anomalies lag the transport signals holds true, the downwelling and upwelling events are clearly linked to warm and cold temperature anomalies, respectively, consistent with expectations. The downwelling events have an average peak temperature anomaly of +0.3°C at around 150 m depth in Lombok Strait, and the upwelling events have an

average temperature anomaly of –0.5°C at the same depth. The peak temperature anomalies probably lie above the shallowest level at which there are Ombai Strait data (Figure III.7b,d); however, in spite of the missing surface data, the Kelvin wave temperature structures are clear. As seen in the transport anomaly composites, the Lombok Strait Kelvin wave temperature anomalies are preceded and followed by anomalies of the opposite sign. The upward phase propagation apparent in the transport data (Figure III.6) is also seen in the temperature composites, although the slope is somewhat ambiguous. The timing of the peak temperature signal in relation to the peak transport signal (t=0) is also ambiguous, with strong composite temperature anomalies in both straits seen from around t=2–15 days. This suggests that the Kelvin wave temperature signals vary from event to event and that the averaging used to form the composite smears out the details of each temperature event. Indeed, a close comparison between the temperature anomalies and the timing of the transport anomalies (colors and vertical lines in Figure III.7) indicates that the relationship between Kelvin wave transport and temperature anomalies is not always straightforward. In some cases (e.g. February 2006), a warm event follows a downwelling event after a few days, and in other cases (e.g. February 2004) the time lag is two weeks. For some events (e.g. June 2006), the temperature anomalies are extremely weak. In some cases, the patterns seen at Lombok and Ombai Strait are also different: for example, in the March 2004 downwelling event, the lag between the transport and the temperature signal is close to two weeks in Lombok Strait but near zero in Ombai Strait (Figure III.7).

McPhaden (2002) used a mixed-layer heat budget analysis to diagnose the phase relationship between Kelvin wave transport and temperature anomalies, and noted that the exact phasing depends on the relative importance of the terms in the heat budget. For example, if horizontal advection dominates the Kelvin wave mixed-layer temperature signal, the transport anomaly should lead the temperature anomaly by around one quarter of a cycle; if Kelvin wave-induced vertical velocity variations control the mixed-layer temperature, Kelvin wave transport and temperature anomalies should be in phase (McPhaden, 2002). Unraveling the transport-temperature phase relationship in these observations is beyond the scope of this paper; however, we show that intraseasonal transport and temperature anomalies are linked using a lagged correlation analysis between transport and temperature anomalies at 130 m in Lombok Strait and at 230 m in Ombai Strait. At zero lag, the correlations between transport and temperature are low, with R^2 values of less than 0.05 in both straits. In Lombok Strait, temperature and transport anomalies have a maximum correlation (R^2=0.19, significant at the 95% level) for transport at 130 m leading temperature at 130 m by around 15 days. In Ombai Strait, the maximum correlation (R^2=0.29) is seen for transport at 230 m leading temperature at 230 m by around 6 days. For Kelvin waves with periods of around 30 days, these time lags are equivalent to phase lags of around ∼180° at Lombok Strait and ∼70°

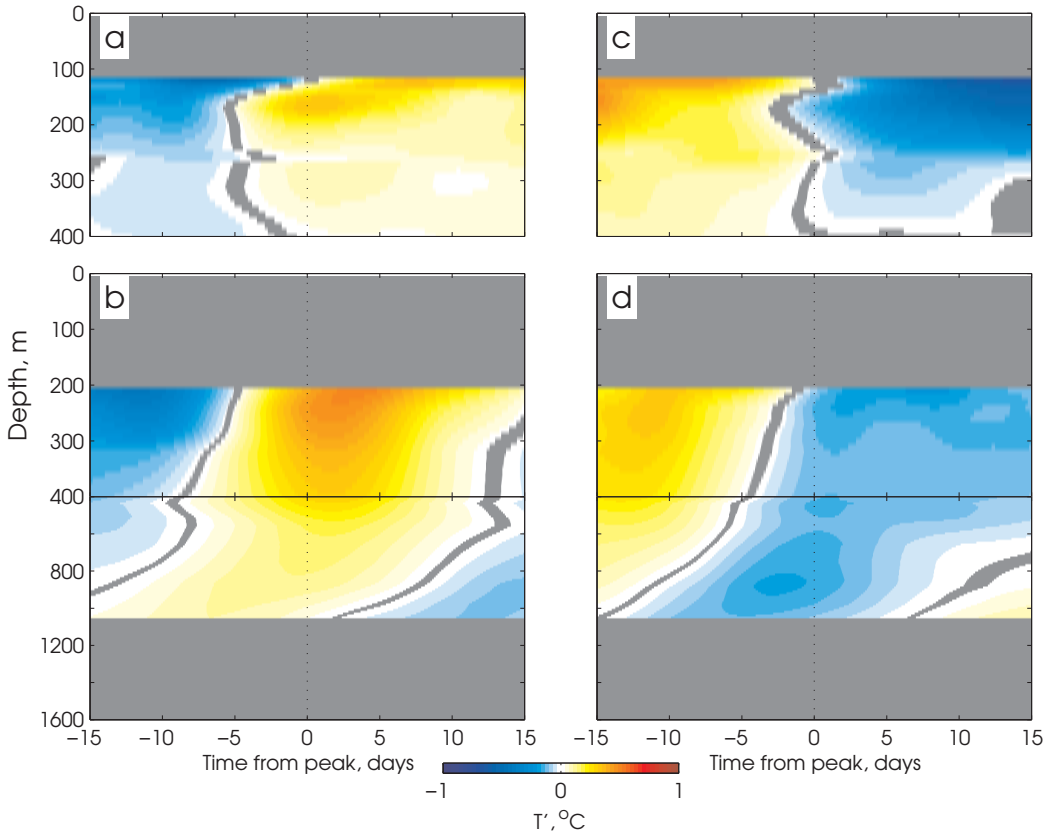

Figure III.8: As for Figure III.6, but for anomalous temperatures (°C). Depths above the shallowest instrument and below the deepest instrument have been masked out.

at Ombai Strait, suggesting the importance of horizontal advection in controlling the Kelvin wave temperature signal (McPhaden, 2002). The significant lagged correlation between the time series of temperature and transport anomalies motivates us to look for relationships between the anomalies for the individual Kelvin wave events. For each Kelvin wave event, we found the first temperature peak following the transport peak at 130 m depth in Lombok Strait and at 230 m depth in Ombai Strait, linking positive transport anomalies to positive temperatures and negative transport anomalies to negative temperatures. Averaged over all 40 events, the lag between the transport and temperature peaks is 11±9 days in Lombok Strait and 12±12 days in Ombai Strait, consistent with the observation that the relative timing of the transport and temperature signals is highly variable. The value of these lags is the same for both downwelling and upwelling events. In both straits, the peak (absolute) temperature and transport anomalies associated with each Kelvin wave event are significantly correlated, with R^2=0.21 in Lombok Strait and 0.28 in Ombai Strait (Figure III.9). These results indicate that the strength of Kelvin wave transport anomalies is positively correlated with the strength of Kelvin wave temperature anomalies, but that the relative phasing between the transport and temperature is highly variable.

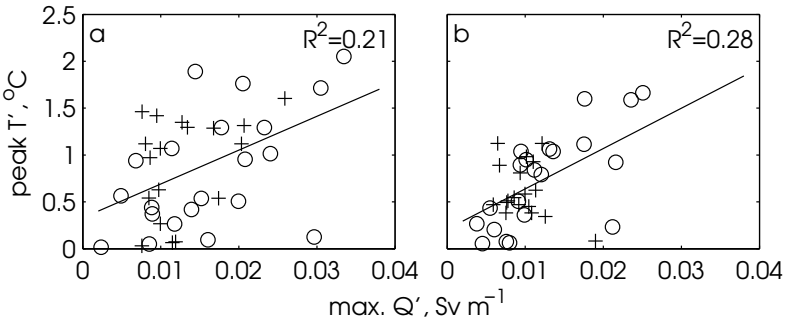

Figure III.9: Scatterplots comparing absolute value of peak transport and temperature anomalies associated with downwelling (circles) and upwelling (pluses) Kelvin wave events at (a) Lombok Strait, and (b) Ombai Strait. Note that the peak can refer to positive or negative values. Temperature data are from the instrument closest to the surface in each strait: ∼130 m at Lombok Strait and ∼230 m at Ombai Strait. Lines and R^2 values are result of linear least-squared regressions. Both are statistically significant (95% significance cutoff is 0.10).

III.5.D Wind forcing

Previous observational and modeling studies (e.g. Qiu et al., 1999) have demonstrated that Indian Ocean winds are the dominant source of intraseasonal energy in Lombok and Ombai Straits. We thus only consider the Indian Ocean as the primary source of the intraseasonal transport signal

in Lombok and Ombai Straits, although there are doubtless small intraseasonal signals originating locally or in the Pacific Ocean (Schiller et al., 2010).

To place the ITF observations into the larger context of Indian Ocean dynamics, each of the Kelvin wave events was linked to a signal in wind. We used zonal winds averaged over 2°S – 2°N in the equatorial Indian Ocean and alongshore winds averaged over a 2°-wide strip along the Sumatra and Java coasts (Figure III.1). The mean and the annual and semiannual harmonics were removed from the winds at each longitude, and the winds were bandpassed with a 20 – 365 day window. To associate Kelvin waves with wind anomalies, we used the line that was fit to the SLA (Figure III.3a) to extract the wind signal for a 10-day wide strip preceding each Kelvin wave. We then picked out the peak wind along this strip, assuming that westerly (positive) winds force downwelling Kelvin waves and easterly (negative) winds force upwelling waves, and the nearest ± 2 m s^{-1} contour associated with the peak wind was identified as the event that forced the Kelvin wave. Figure III.3b shows the wind field and the contour associated with each Kelvin wave. Having an estimate of the location and magnitude of each wind peak allowed us to quantify the characteristics of the wind forcing in terms of its longitude and strength, and associating each event with a wind contour allowed us to quantify the duration and longitudinal span of the wind bursts. These are somewhat arbitrary metrics for characterizing the wind events, but they allow a comparison of the different events. Typically, wind events are seen to the west of SLA events, as would be expected for winds forcing an eastward-propagating SLA signal. In general, westerly and easterly wind bursts share fairly similar characteristics: westerly events are centered around 80 ± 13°E, and easterlies around 78 ± 9°E. Westerlies tend to have a slightly greater fetch, with an average longitudinal span of around 32° and a duration of 20 days, compared with around 27° and 15 days for easterlies. Contrary to previous observations (Waliser et al., 2003; Iskandar et al., 2005), we did not notice strong seasonal asymmetries in the properties of the wind events, and we were thus unable to find a clear connection between the prevalence of mode-2 events in boreal summer and the wind forcing.

The exercise of associating each Kelvin wave with an Indian Ocean SLA and wind anomaly and an ITF transport and temperature anomaly allowed us to evaluate how the wind forcing affects the characteristics of the Kelvin waves. This was done using a series of scatterplots comparing the properties of each of the events, including wind strength, location, and duration; peak transport anomaly and depth; total transport anomaly; and peak temperature anomaly (Figure III.10). Generally, Kelvin wave transport anomalies have similar amplitudes in Lombok and Ombai Straits (Figure III.10f), and Kelvin waves with large transport anomalies also have large temperature anomalies (not shown). The strength of the Kelvin wave transport and temperature anomalies is well correlated with wind fetch: for both downwelling and upwelling Kelvin waves, the amplitude of the transport anomalies had positive correlations with wind duration, and longitudinal extent

(Figure III.10a,b). These wind properties are also well correlated with Kelvin wave temperature anomalies (Figure III.10c,d). In agreement with linear ray theory (Eq. III.4), Kelvin waves forced farther west in the basin tend to penetrate deeper in the water column (Figure III.10e).

III.6 Energy Pathways

III.6.A Partitioning of energy at Lombok Strait

Tracking the Kelvin wave signal in SLA is an effective way to evaluate the pathways the waves take as they propagate. Lombok Strait is 35 km wide and the Rossby radius of deformation here is around 100 km, so an oft-asked question is whether Kelvin wave energy enters Lombok Strait, and if so how much. Syamsudin et al. (2004) associated annual maxima in altimetric SLA measurements with the single largest Kelvin wave observed each year from 1993 – 2001, and then compared the spectral energy east and west of Lombok Strait. From this technique, they estimated that 56% of incoming Kelvin wave energy enters Lombok Strait, with a standard deviation of 14% over the 9-year time period. Note, however, that this estimate was based on the semiannual Kelvin wave and therefore is not necessarily directly comparable to the intraseasonal Kelvin waves considered in the present study. Here, we examine the SLA signals of the individual Kelvin waves to identify the pathway of intraseasonal Kelvin waves. For each individual event, we extracted the SLA signal over areas 2° to the west and to the east of Lombok Strait (regions W and E in Figure III.1). The root mean squared SLA (rms_{SLA}) in these regions over the course of each event was used as a proxy for Kelvin wave energy, and comparing the rms_{SLA} values at W and E gave an estimate of how much of the incoming energy was siphoned north into Lombok Strait. Averaged over the 40 Kelvin waves observed during the INSTANT period, 37% ± 9% of the incoming Kelvin wave energy bypassed Lombok Strait and continued east along the coastal waveguide. This implies that approximately 63% of the incoming energy entered Lombok Strait, or was dissipated or reflected off the topography in that region. This ratio is the same within statistical error bars for downwelling and upwelling Kelvin waves, although generally a greater percentage of the incoming energy of downwelling waves enters Lombok Strait compared with upwelling waves. We found no clear relationship between wind strength or fetch and the ratio of rms_{SLA} east and west of Lombok Strait, indicating that the winds are not the primary determining factor for how much Kelvin wave energy enters Lombok Strait.

III.6.B Kelvin waves north and south of Sumba Island

S09 suggested that as the Kelvin waves propagate eastward along the Nusa Tenggara waveguide from Lombok to Ombai, there are two pathways that the waves could take (Figure III.1).

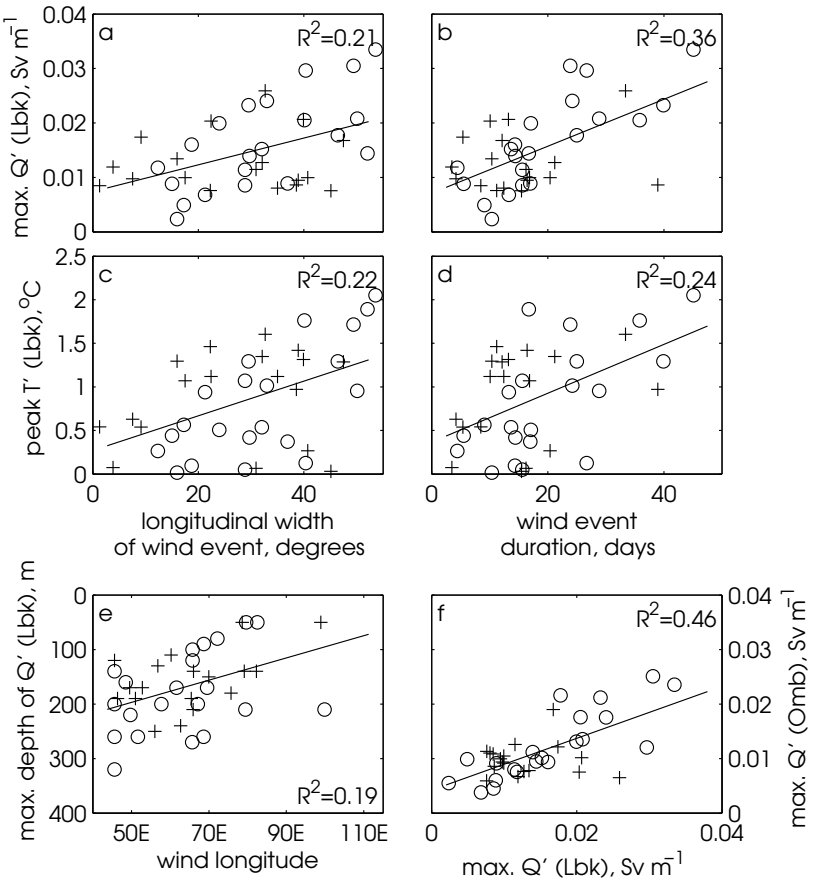

Figure III.10: Scatterplots comparing transport, temperature, and wind properties of downwelling (circles) and upwelling (pluses) Kelvin wave events. Lines and R^2 values are result of linear least-squared regressions. All are statistically significant (90% significance cutoff is 0.07, 95% significance cutoff is 0.10). (a) Magnitude of peak Lombok Strait transport anomaly due to the Kelvin wave versus longitudinal extent of the wind event; (b) Magnitude of peak Lombok Strait transport anomaly versus duration of the wind event; (c) Magnitude of peak Kelvin wave temperature anomaly observed in Lombok Strait versus longitudinal extent of the wind event; (d) Magnitude of peak Lombok Strait temperature anomaly versus duration of the wind event; (e) Depth penetration of transport anomaly in Lombok Strait versus westernmost longitude of wind patch; (f) Magnitude of peak transport anomaly seen in Ombai versus in Lombok Strait.

North of Sumba Island the sill depth is around 900 m, and Kelvin wave energy shallower than this depth likely propagates directly to Ombai Strait, whereas deeper Kelvin wave energy may be blocked by the sill. The deeper waves could conceivably either pass through Savu/Dao Strait (sill depth 1150 m) into the Savu Sea to Ombai Strait, or, if deeper than this sill, proceed southward into Timor Passage (S09). For now we only consider whether the waves propagate north versus south of Sumba Island. For each of the 40 events, we extracted the Kelvin wave SLA along the path north and south of Sumba Island and computed the rms_{SLA} of the signal over the duration of the event and longitude range of Sumba Island (117°E – 122°E; shaded regions labeled N and S in Figure III.1). The ratio of the rms_{SLA} along the two paths, N:S was then used as an estimate of how much of the incoming energy went north or south of the island. Averaged over all 40 events, N:S was equal to around 1.0 ± 0.1, meaning that half of the incoming Kelvin wave energy goes north of Sumba Island. Separating the two types of events shows that more of the incoming energy for downwelling Kelvin waves goes south of Sumba Island, and more of the upwelling Kelvin wave energy travels north of Sumba Island: for the downwelling events, N:S was equal to around 0.6 ± 0.2, whereas for the upwelling events the ratio was 1.3 ± 0.2. There is little correlation between the amount of Kelvin wave energy going north versus south of Sumba Island and the depth of the maximum transport anomalies seen in either Lombok or Ombai Straits. This suggests that the routing of the Kelvin waves north or south of Sumba Island does not necessarily arise from differences in the depth penetration or structure of the Kelvin waves as hypothesized by S09. The N:S ratio is also not well-correlated with wind strength, location, or fetch, nor does the ratio have an obvious seasonal cycle.

III.7 Wind-forced model

Kelvin wave dynamics in the ITF region can also be explored using a simple wind-forced model in which the ocean is considered to be a linear, continuously stratified fluid, and wind stress is applied as a body force over a shallow mixed layer (c.f. Cane, 1984; Kessler and McPhaden, 1995). The Kelvin wave response is determined by integrating along the characteristic $x - ct =$ constant, from the western edge of the Indian Ocean basin (50°E) to a point x_o along the Kelvin wave path. Each mode of some modeled quantity, A_n (for example, sea level, velocity, pressure, etc.), is computed individually, then the modes are summed to give the total response. The generalized formulation for this is given by

$$A(x_o, z, t) = \sum_{n=1}^{\infty} \alpha_n(z) \int_{50°\text{E}}^{x_o} \tau^x \left(x, t + \frac{x - x_o}{c_n} \right) dx, \tag{III.6}$$

where α_n is the coefficient for the mode-n part of the modeled signal, c_n is the baroclinic phase speed, and τ^x is the zonal wind stress. To model A_n as sea level, $\alpha_n = \psi_n(0)^2/\rho g D$, where $\psi_n(0)$ is the vertical structure function $\psi_n(z)$ (Eq. III.1) at the surface (z=0), ρ is seawater density, g is the gravitational constant, and D is the bottom depth. To model A_n as zonal current as a function of depth, we set $\alpha_n = \psi_n(0)\psi_n(z)/\rho c_n D$ (Kessler and McPhaden, 1995).

We used this model to examine some of the noteworthy features of the observations: the role of wind forcing over different parts of the basin, the relative strength of the different baroclinic modes, and the importance of stratification variability. As the baseline case, we forced the model with 6-hourly wind stress along the Kelvin wave path (Figure III.1): zonal winds along the equator over the longitude range 50°E – 100°E, averaged over 2°S – 2°N, and alongshore winds along the Sumatra and Java coasts from 100°E – 115°E. We ran the model for the 2004 – 2006 INSTANT deployment period in order to compare the modeled output with our observations. All model quantities have been filtered in the same manner as the corresponding observations in order to facilitate the comparisons. The stratification *N(z)* was obtained from the Argo gridded temperature and salinity fields (Roemmich and Gilson, 2009a) averaged over the same area as the wind patch during the same time period, and the phase speeds c_n were computed from Eq. (III.1) using Argo data (Table III.1), again for the same space and time period as the wind patch.

To evaluate the success of the model, we used a linear least-squares method to fit the observed Lombok Strait velocity at each time to the first four modes of modeled velocity over depths 100 – 300 m. Averaged over all times, the first two modes accounted for 48% and 38% of the variance of the time series, respectively, with modes 3 and 4 accounting for less than 13%. Modes higher than n=2 can thus reasonably be neglected for comparisons between model results and observations. Even with only the first two modes included, the model effectively reproduces the propagation of the observed Kelvin waves (Figure III.11). The lines fit to the Kelvin wave signals observed in SLA (Figure III.3a) have been superimposed on the modeled SLA (Figure III.11), showing that all of the Kelvin waves seen in the observed SLA were reproduced by the model. This confirms that our observations are entirely consistent with wind-forced Kelvin waves and also validates the effectiveness of the Kelvin wave selection method used to identify the events in the observations. Comparing the timing of the modeled and observed signals shows that in some cases the modeled events are slower than the observed events. This difference may be a result of the model's sensitivity to bottom depth and stratification, which are based on the gridded Argo fields and thus are rather coarse. Alternatively, nonlinear effects, for example due to wave-mean flow interaction, may cause the Kelvin waves to propagate faster than predicted by the model (McPhaden et al., 1986).

Figure III.12a and b show the observed Lombok Strait transport anomaly and the sum of the first two modes of the modeled transport anomaly, with the times corresponding to the observed

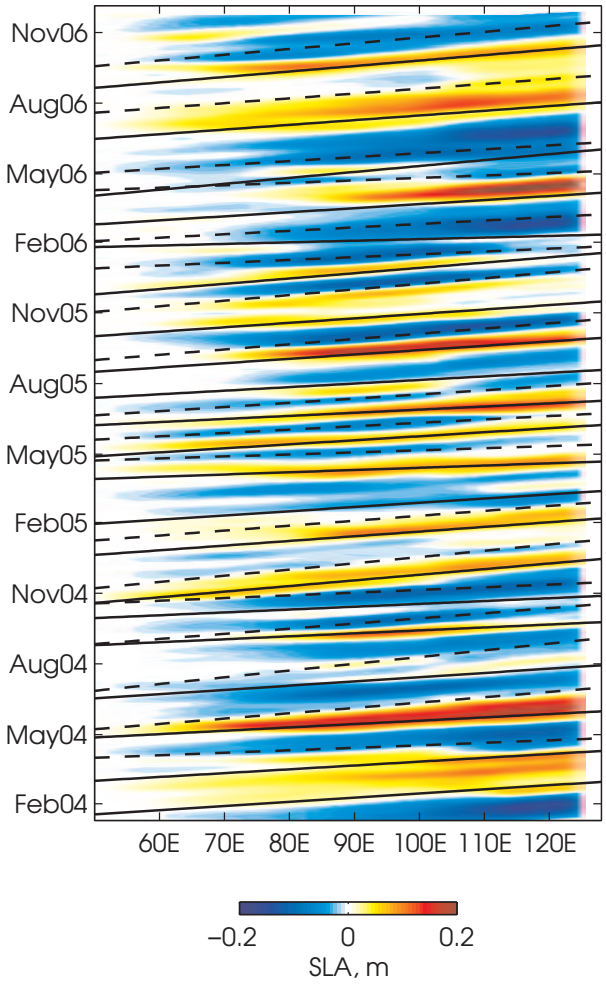

Figure III.11: Model results (sum over first two modes): SLA over the Kelvin wave path. Lines corresponding to paths of the observed downwelling (solid lines) and upwelling (dashed lines) Kelvin waves are shown, as in Figure III.3a.

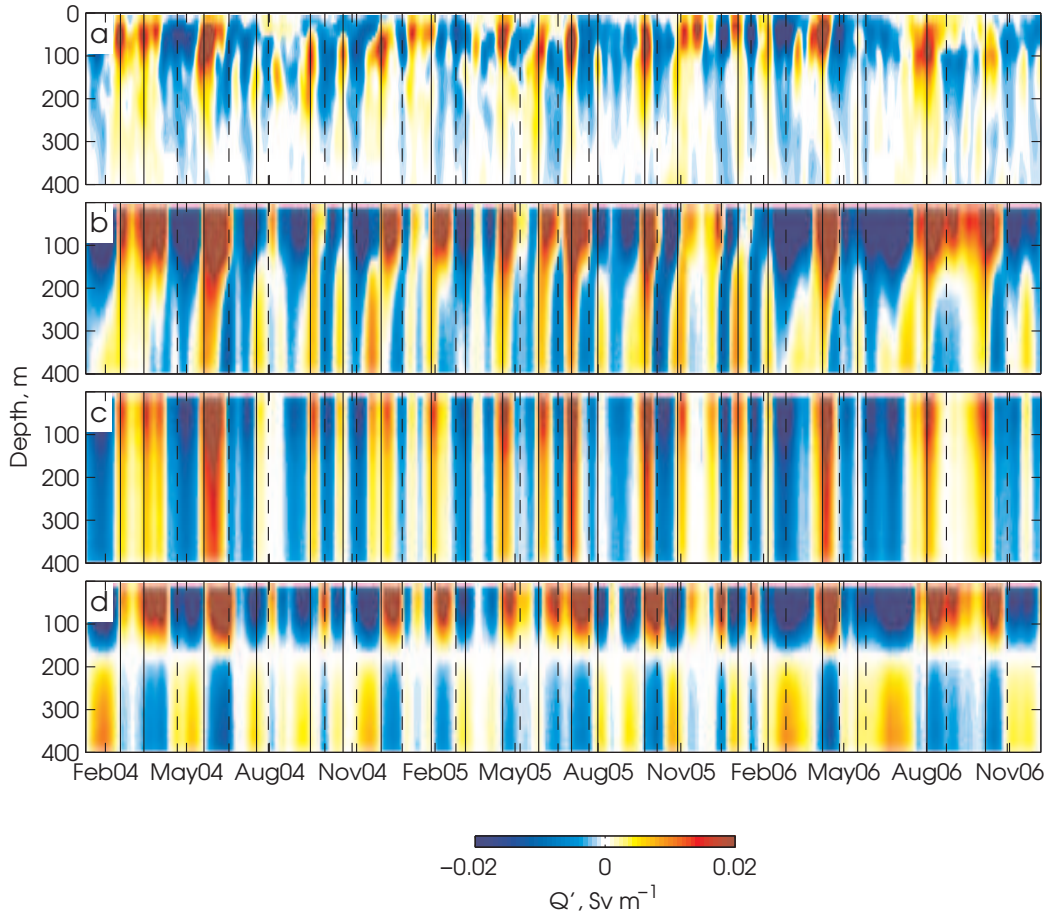

Figure III.12: Intraseasonal transport anomaly in Lombok Strait: (a) observations (same as Figure III.5c); (b) sum over first two modes of the model; (c) modeled mode-1; (d) modeled mode-2. Vertical lines indicate arrival of observed Kelvin waves, with solid lines denoting downwelling events and dashed lines denoting upwelling events. The thick lines indicate the events with structures that were shown to be dominantly mode-2 in Section III.5III.5.B The model was forced with winds over 50°E – 115°E.

events indicated with vertical lines. The model generally does an excellent job of reproducing the Kelvin wave transports. As is seen in the modeled SLA (Figure III.11), some of the modeled events are slower than the observations by a few days. The mean time difference (Kelvin wave arrival time from model minus observations) is around 4 days $\pm$ 5 days, where the uncertainty represents the standard deviation over all of the events. Since this time difference is reasonably small and varies over the set of modeled events, it is likely due to small nonlinear effects in the ocean that are not accounted for by the model, for example wave-mean flow interaction. Linear theory requires the superposition of two or more modes in order for energy to propagate in the vertical. The success of the model in correctly reproducing the observed vertical structure, for example the slope of the vertical phase propagation, is dependent on the precise timing of the arrival of the two modes. This is illustrated strikingly when the first- and second-mode responses of the modeled transport anomaly are plotted separately: the first mode is responsible for the dominant signal of the Kelvin wave throughout the water column (Figure III.12c), and the second mode (Figure III.12d) is slower and has a zero-crossing at around 180 m depth. Thus, when the modes are added, their relative phasing produces the upward phase propagation characteristic of Kelvin waves. The amplitude of the mode-2 signal is surprisingly large, and contributes substantially to the surface signal in Lombok Strait. This has important consequences for understanding and modeling the ITF on intraseasonal timescales: to characterize the surface layer of Lombok Strait, Ekman dynamics alone are not sufficient and remotely forced equatorial waves must be taken into account.

The modeled transport anomaly at Ombai Strait further highlights the importance of the second mode (Figure III.13). As for the modeled Lombok Strait transports, the timing and vertical phase propagation of the Kelvin waves observed in Ombai Strait are well-represented by the model. In Lombok Strait, mode-1 more closely resembles the observed transports (Figure III.12a,c), whereas in Ombai Strait the observations throughout the water column look much more like the mode-2 signal (Figure III.13a,d).

The winds used to force the model extend as far east as 115°E. The model does not incorporate any of the effects of energy dissipation or reflection, nor does it allow any energy to split and go north through Lombok Strait. Stratification does not vary with longitude or time, so the only parameters that change as the waves propagate east of Lombok Strait are the vertical structure functions ψ(z), which vary with bottom depth (Eq. III.1). It is therefore possible to make a crude estimate of the energy lost to dissipation and reflection, and north through Lombok Strait, by comparing the model output to the observations. In the simplest scenario, a certain percentage (α_L) of the incoming Kelvin wave energy is siphoned north through Lombok Strait above the 300 m sill. The remaining energy (1–α_L above the 300-m sill and 100% below it) continues eastward along the waveguide. Downstream of Lombok, the sill will block all of the deep energy below 900

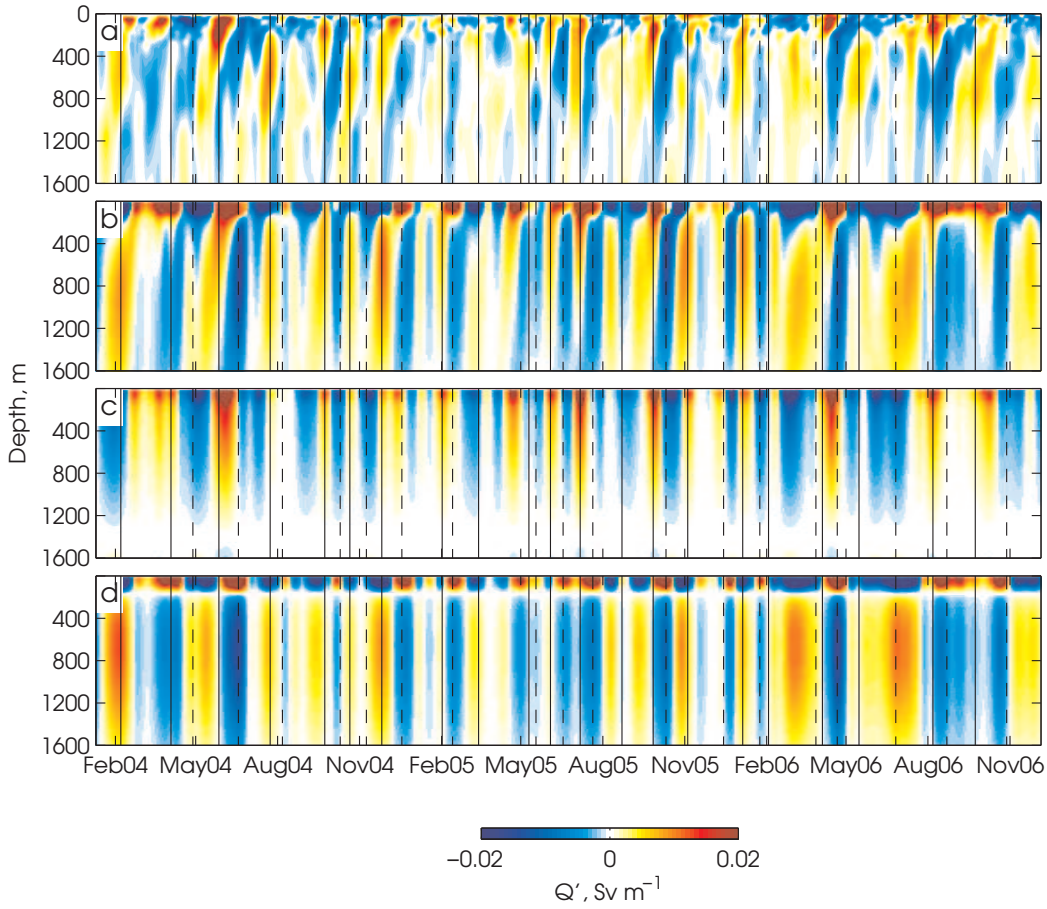

Figure III.13: As for Figure III.12 but for Ombai Strait. Note the different depth scale than in Figure III.12.

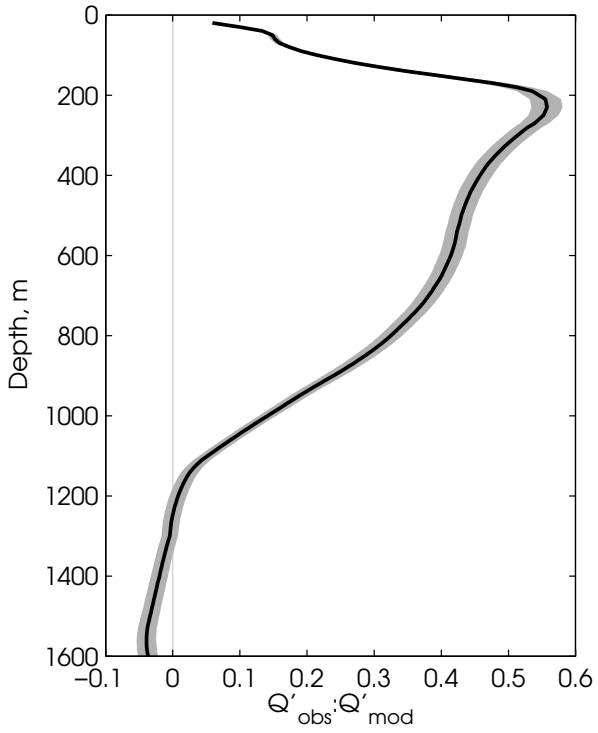

Figure III.14: Ratio of observed to modeled Ombai Strait transport anomaly at each depth. The model was forced with winds over 50°E – 115°E, and the modeled transport used is the sum over the first two modes.

m or 1150 m depth, depending on whether the wave travels north or south of Sumba Island. Thus, in this simplistic picture of the dynamics, the Kelvin waves that reach Ombai Strait will be missing α_L of the surface signal and should have zero energy at depth, and the energy at mid-depth should be a maximum. The ratio of observed to modeled Kelvin wave transports, calculated at each depth level, should allow us to estimate α_L and assess whether the Kelvin waves go north or south of Sumba Island, i.e. over the 900-m sill or the 1150-m sill. This ratio is shown in Figure III.14: it was computed by performing a linear regression of the observed versus the modeled transport anomalies at each depth. The error shown in Figure III.14 represents the uncertainty from the regression. As expected, the ratio in the surface layer is low due to the energy that is lost through Lombok Strait. However, instead of being constant above the 300-m Lombok Strait sill depth, the ratio has a minimum (0.06) at the surface and increases to a peak of 0.55 at a depth of around 230 m. This is explained by recalling that the Kelvin waves are diving, so the energy $1–\alpha_L$ that does not go through Lombok Strait is redistributed vertically as the waves travel eastward. The ratio is fairly constant (0.4 – 0.5) between around 400 m and 800 m; below this depth the ratio drops off rapidly and falls to zero by 1200 m. Again, the vertical energy propagation can be used to explain why the energy is not zero below the 900-1150 m sill at Sumba Island: some of the Kelvin wave signal at mid-depths will have been redistributed deeper as the waves dive. There is too much conjecture in this picture of the dynamics to allow us to estimate the energy partitioning at Lombok Strait, or to assess whether the deep part of the signal is blocked by the 900-m deep sill at Sumba Strait or the 1150-m deep sill at Savu/Dao Strait. However, the ratio of observed to modeled Kelvin wave transport shown in Figure III.14 is consistent with the expected Kelvin wave dynamics in this region, and thus further validates the application of linear ideas to understanding Kelvin wave dynamics in the ITF region.

Figure III.15 shows the composited transport anomalies in Lombok and Ombai Straits using the model output. To form the composites, each of the 21 downwelling and 19 upwelling events observed in the INSTANT data was matched to the corresponding event in the modeled time series by matching peaks in the depth-averaged observed and modeled (mode-1 plus mode-2) Lombok Strait transport data. This gives a t=0 for each event based on the signature of that event in the model. The composites highlight the successes and failures of the model in reproducing the Kelvin waves (Figure III.15). The model correctly shows the strongest transport anomalies at around 100 m depth in Lombok Strait, but fails to reproduce the local transport minimum at the surface. At Ombai, the model predicts a strong surface transport anomaly that is not seen in the observations; as discussed above, this is because the model is not able to lose energy into Lombok Strait, so the surface transports are overestimated. The modeled transports penetrate much deeper into the water column than the observed signals, again due to the model's inability to capture the loss of energy resulting from Kelvin waves being blocked by the sills. The modeled Kelvin wave transports persist

for roughly 10 – 14 days, consistent with the observed events: this suggests that the duration and size of the wind events that force the Kelvin waves are linearly related to the duration of the Kelvin waves. Although the model correctly reproduces the upward trend in vertical phase propagation, the slope of this upward phase is not well modeled, as discussed above. In Lombok Strait the vertical propagation of the modeled signal is much more pronounced than in the observations, whereas in Ombai Strait the modeled transport anomalies show virtually no phase propagation between 200 m and 1200 m depth. This is not surprising, since neither the mode-1 nor the mode-2 signals vary much over this depth range (Figure III.2,Figure III.13).

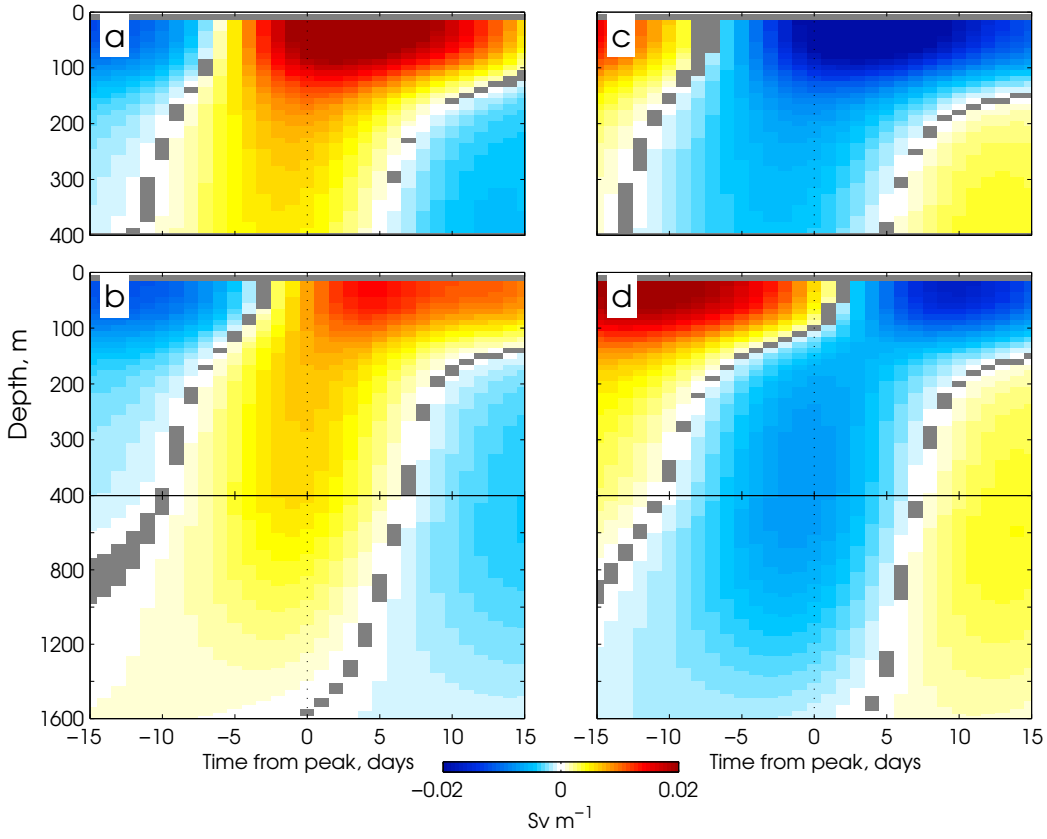

Figure III.15: Composited transport anomalies for downwelling and upwelling Kelvin waves: as for Figure III.6 using the modeled transport anomalies. The model was forced with winds over 50°E – 115°E, and the output shown is the sum over the first two modes.

To test the impact that wind anomalies in different regions have on Kelvin wave generation, we forced the model with winds over a number of different longitude ranges: (a) western equatorial Indian Ocean (50°E – 75°E); (b) eastern equatorial Indian Ocean (75°E – 100°E); Sumatra and Java coast (100°E – 115°E); and (d) [control case] along the entire Kelvin wave path (50°E – 115°E). The results are shown as depth-averaged transports in Figure III.16a. Correlations between the modeled

and observed Lombok Strait transports are highest (R^2=0.36) when winds over the entire Kelvin wave path (control) are used, followed closely by the case of eastern Indian Ocean winds (R^2=0.32). The amplitude of the signal forced in the control case, winds over the entire Kelvin wave path, is large (standard deviation of 6 x 10^{-3} Sv m^{-1} compared to the data, which have a standard deviation of 2.6 x 10^{-3} Sv m^{-1}), whereas the amplitude of the modeled signal forced by only the winds over the eastern Indian Ocean (standard deviation of 3.4 x 10^{-3} Sv m^{-1}) more closely resembles the data. Interestingly, using just the winds along the Sumatra and Java coasts reproduces the observed Kelvin wave events quite well (R^2=0.17). The modeled transports forced by winds in the western part of the basin have R^2=0.06, barely above the 95% significance level of 0.05. These results confirm that the winds in the eastern equatorial Indian Ocean (east of 75°E) dominate the forcing of intraseasonal Kelvin waves, but also highlight the important contribution of the alongshore winds off of Sumatra and Java to the Kelvin wave signal. In a study using ECMWF reanalysis winds, Iskandar et al. (2005) showed that during boreal summer, intraseasonal variations seen in the ITF region are primarily forced by winds over the eastern Indian Ocean, whereas in boreal winter the contribution of winds along the Sumatra and Java coasts also contribute significantly. Our results suggest that winds off of Sumatra and Java contribute significantly to the intraseasonal energy in the ITF during all seasons.

Although the linearity assumption implicit in the model requires that *N(z)* be constant in longitude and time, we explored allowing *N(z)* to vary on the monthly time and 1° longitude grid of the Argo data set. The depth-averaged transports that result from using a fixed and a variable Brunt-Väisälä frequency are shown in Figure III.16b. The amplitude of the events is stronger when *N(z)* is allowed to vary in longitude or time, but the timing of the events is not changed, nor are their vertical structures (not shown), suggesting that seasonal and spatial differences in stratification are not large enough to significantly modify the propagation speeds of either mode-1 or mode-2 Kelvin waves. Since the relative phasing of the two modes determines the vertical structures of the Kelvin waves, seasonal and spatial changes do not appear able to account for changes in the vertical structures.

III.8 Summary

A 3-year, high-resolution time series of velocities and temperatures was used to observe the vertical structure of Kelvin waves in the ITF outflow passages for the first time. We have identified 40 Kelvin wave events in Lombok and Ombai Straits associated with transport and temperature anomalies during 2004 – 2006. Each wave was in response to an anomalous Indian Ocean zonal wind event and was associated with an eastward-propagating SLA signal. Consistent with previous

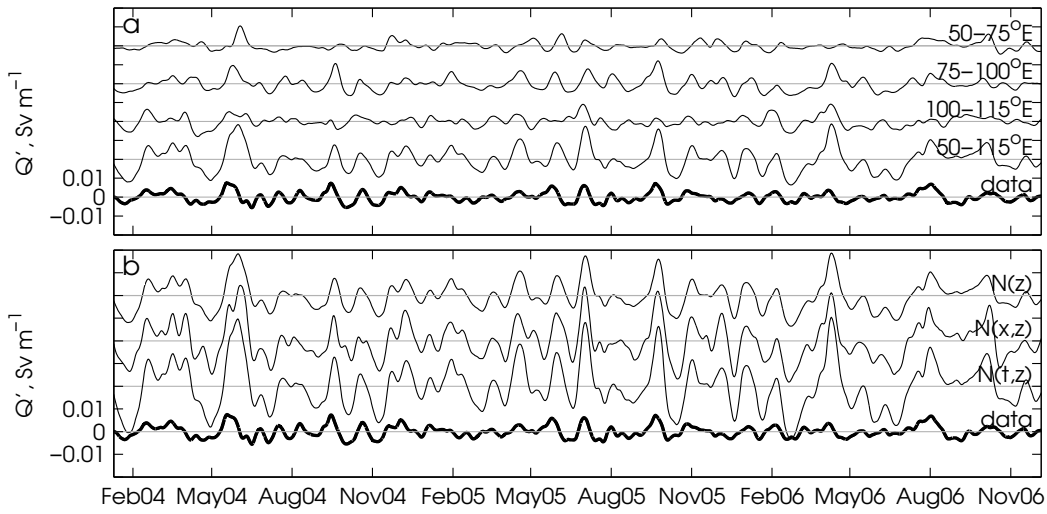

Figure III.16: Sum of first two modes of modeled transport anomalies in Lombok Strait, vertically averaged over depths 100 – 300 m. (a) Using a fixed stratification profile and forced with winds over different longitude ranges along the Kelvin wave path to force the model; (b) forced with winds over the entire Kelvin wave path (50°E – 115°E) and using a stratification profile that is fixed (*N(z)*), varies with longitude (*N(x,z)*), and varies with time (*N(t,z)*). In both (a) and (b), the thick line shows the observed vertically-averaged Lombok Strait transport anomaly and plots are offset by 0.02 Sv m^{-1}.

observations of equatorial Indian Ocean Kelvin waves, our observations show that westerly wind events produce downwelling Kelvin waves with positive transport anomalies and warm temperature anomalies, and easterly wind events produce upwelling Kelvin waves associated with negative transports and cool temperature anomalies. The transport signals observed in the ITF outflow passages are consistent with linear theory and suggest that both upwelling and downwelling Kelvin waves are forced with periodic winds with periods of 28 – 46 days.

We found correlations between the duration and longitudinal extent of the wind patch that forced each event and the strength of the transport and temperature anomalies in Lombok Strait, consistent with linear model of wind acting as a body force on the surface layer of the ocean and exciting Kelvin waves. Linear ray theory, which is based on the idea that Kelvin waves are a superposition of many baroclinic modes that propagate into the ocean interior as a beam of energy, can also explain the depth of the Kelvin waves observed at Lombok Strait: the further west a Kelvin wave is generated, the deeper it can penetrate into the water column once it has reached the ITF region. These results suggest that Kelvin waves generally behave in a linear fashion as they propagate through this region.

Altimetric SLA measurements show that 37% ± 9% of the Kelvin wave energy seen just west of Lombok Strait (Figure III.1) bypasses Lombok and continues moving east along the coastal wave guide. The remainder can be assumed to enter the internal seas via Lombok Strait, or to be topographically reflected or dissipated. Kelvin wave signals in SLA north and south of Sumba Island indicate that downstream of Lombok, Sumba Island splits the incoming Kelvin wave energy roughly equally to the north and south.

A linear wind-forced model was used to examine how the behavior and structure of the first two baroclinic modes impacts Kelvin waves observed in the ITF. The model did a good job of reproducing the observations. Comparing the observed and predicted transports at Ombai Strait suggested that a significant portion of the Kelvin wave energy is lost through dissipation and/or reflection off of topography. This comparison also confirmed the basic theory that some of the incoming Kelvin wave signal above 300 m is siphoned north through Lombok Strait, and the deep Kelvin wave signals are blocked by a sill downstream of Lombok Strait. The model showed that the dominant forcing region of intraseasonal Kelvin waves is the equatorial Indian Ocean between 75°E and 100°E, the along-shore winds off of Sumatra and Java between 100°E and 115°E also contribute significantly to the Kelvin waves observed in the ITF. Wind forcing in the western equatorial Indian Ocean (west of 75°E) contributes little intraseasonal Kelvin wave energy. Finally, we used the model to consider the cases of stratification varying slowly in time or in space: in both cases, the amplitudes of the modeled Kelvin waves are much larger than in the constant stratification case or the data.

III.9 Acknowledgments

We thank Sophie Cravatte, whose comments greatly improved this manuscript. The first author gratefully acknowledges assistance from the NASA Earth and Space Science Fellowship. This work was also supported by NSF Grant 0725476. We are grateful to our colleagues Drs. Indroyono Soesilo and Sugiarta Wirasantosa at the Agency for Marine and Fisheries Research (BRKP), Indonesia, as well as the captains and crews of the Baruna Jaya I and VIII and the *R/V* Southern Surveyor. The wind data were obtained from Global Modeling and Assimilation Office at the NASA Goddard Space Flight Center, Greenbelt, MD, USA. The altimetric SLA products were produced by Ssalto/Duacs and distributed by Aviso with support from Cnes.

Chapter III, in full, is a reprint with no modifications to content of the article as it appears in Journal of Physical Oceanography, 2010, K. Drushka, J. Sprintall, S.T. Gille, and I. Brodjonegoro, copyright 2010 American Meteorological Society. I was the primary researcher and author of this manuscript, and the co-authors directed and supervised or provided the data for the research which forms the basis for this chapter.

IV

In situ observations of Madden-Julian Oscillation mixed layer dynamics in the Indian and western Pacific Oceans

IV.1 Abstract

The response of the ocean mixed layer to the Madden-Julian Oscillation (MJO) in the Indo-Pacific region is determined using in situ observations from the Argo profiling float dataset. Composites reveal that the MJO forces systematic variations in mixed-layer depth and temperature throughout the domain. The largest MJO mixed-layer depth anomalies (>10 m peak-to-peak) are observed in the Indian Ocean west of Sumatra and in the Seychelles-Chagos thermocline ridge region, as well as in the western Pacific Ocean. Strong mixed-layer temperature variations (>0.5°C peak-to-peak) are found in the Indian Ocean along the equator, in the region between northwest Australia and Java, and in the far western Pacific Ocean. A heat budget analysis shows that the mixed-layer temperature variations associated with the canonical MJO are driven almost entirely by anomalous net surface heat flux, which is dominated by variations in solar shortwave radiation (71%) that result from anomalous MJO convection. An exception is in the central Indian Ocean and in the region between Australia and Java, when rapid deepening of the mixed layer during the onset of the active MJO induces significant basin-wide entrainment cooling. In the central equatorial Indian Ocean and in the far western Pacific warm pool region, variations in mixed-layer depth associated with the

MJO can modulate MJO variations in heat flux into the mixed layer, and therefore mixed-layer heat storage, by up to 25–50%. This suggests that accurately resolving mixed-layer depth variations in models at MJO timescales may be important for capturing temperature variations, and thus air-sea interaction, associated with the MJO.

IV.2 Introduction

The Madden-Julian Oscillation (MJO) is a system of large-scale coupled patterns of atmospheric convection and winds that originate in the western tropical Indian Ocean, propagate eastward along the equator, and eventually die out in the eastern Pacific Ocean (Madden and Julian, 1972; Zhang, 2005). Atmospheric MJO forcing exerts a profound influence on the mixed layer of the tropical Indian and Pacific Oceans through anomalous fluxes of heat, precipitation, and momentum (e.g. Hendon and Glick, 1997; Lau and Waliser, 2005). In turn, these processes affect the distribution of heat and salt in the ocean mixed layer. The impacts of the MJO on weather and climate are manifold (for examples, see Zhang, 2005), most notably in the tropical Indian and Pacific Oceans where the forcing is strongest, but also throughout the world. Despite extensive study, model simulations consistently fail to reproduce the MJO correctly, and MJO forecasts are not accurate beyond around two weeks (Seo et al., 2009). As a result, the impacts of the MJO on both present-day and future weather and climate are still largely unresolved.

Results from model sensitivity tests have suggested that air-sea coupling is an integral part of MJO dynamics (e.g., Flatau et al., 1997; Waliser et al., 1999; Inness and Slingo, 2003; Maloney and Sobel, 2004; Woolnough et al., 2007). Developing a better picture for how MJO forcing impacts the ocean, and how this may feed back onto the MJO, is necessary for improving MJO prediction and modeling. This requires quantifying not only the variations associated with the MJO at the air-sea interface, but also the variations within the upper ocean.

The MJO can force significant fluctuations in the mixed-layer depth (MLD; e.g. Lukas and Lindstrom, 1991; Shinoda and Hendon, 1998; Waliser et al., 2003; Duvel et al., 2004). Since heat, freshwater and momentum inputs are integrated over the mixed layer, variations in MLD could modulate the impacts of surface forcing. There have been relatively few water-column observations available at timescales sufficient for capturing MJO variability. Consequently, previous studies estimating MJO heat budgets have generally used model output (e.g. Schiller and Godfrey, 2003; Waliser et al., 2003; Duvel et al., 2004; Lucas et al., 2010) or relied only on satellite observations (e.g. Duvel and Vialard, 2007); or, those studies that did include in situ subsurface observations have been limited to mooring sites (e.g. Anderson et al., 1996; Zhang and McPhaden, 2000; Vialard et al., 2008) or small regional studies (e.g. Sato et al., 2010; Jayakumar et al., 2010). Collectively,

these studies produce a fairly coherent description of MJO signals in the upper ocean; however, to our knowledge there has been no study using in situ observations to characterize the mixed-layer dynamics of the MJO throughout its entire Indo-Pacific domain.

In the present study, we use data from Argo floats to assess the response of the mixed layer of the tropical Indian and western Pacific Oceans to MJO forcing. Argo offers an advantage over satellite data sets by providing direct subsurface measurements of temperature and salinity. From these observations we estimate MLD and vertical temperature gradients, and construct composite MJO mixed-layer heat budgets based on the index of Wheeler and Hendon (2004) ("Wheeler-Hendon index"). The Wheeler-Hendon index breaks the MJO cycle into eight phases that correspond to the shifting locations of maximum intraseasonal winds and convection, so composites formed using this index describe the strength and progression of the MJO as it moves over the Indian Ocean and east through the Pacific Ocean. Although our estimates are not sufficiently accurate to close the heat budget, we use the composites to qualitatively expand on the existing picture of how MJO forcing impacts the upper ocean, with a particular emphasis on the role of MLD variations.

The paper is organized as follows: in section IV.3 we describe the data sets used in the study and the method used to form the MJO composites. The MJO forcing and mixed-layer response throughout the entire spatial domain are presented in section IV.4, and the effect of MJO-related MLD variations is shown in section IV.5. In section IV.5.A we discuss sources of uncertainty in the methodology, and in section IV.6 we summarize our findings.

IV.3 Data and Methodology

IV.3.A Heat budgets

The "active" MJO is characterized by the presence of a deep convective anomaly with a zonal wavelength of ∼12,000–20,000 km that is coupled to zonal surface wind anomalies (Wheeler and Hendon, 2004). The whole system propagates eastward along the equator at around 5 $\mathrm{m\,s^{-1}}$ (Zhang, 2005). To the east and west of the active MJO, convection and winds are anomalously weak: this characterizes the inactive, or suppressed, MJO phase. Atmospheric forcing during MJO events affects the ocean mixed layer in various ways: convective cells block the incoming solar radiation from reaching the sea surface, producing anomalously cool sea surface temperatures (SSTs) (e.g. Hendon and Glick, 1997; Shinoda et al., 1998). Wind anomalies can modify SST via several mechanisms (Cronin and McPhaden, 1997, and references therein). Increased wind stress associated with the MJO cools the sea surface by enhancing latent heat loss (Zhang and McPhaden, 1995). Strong winds can also induce localized vertical entrainment, which has been shown to contribute significantly to (McPhaden, 2002; Schiller and Godfrey, 2003; Saji et al., 2006; Jayakumar et al., 2010), or even

dominate (Duncan and Han, 2009), changes in mixed-layer temperature. Vertical velocities, for example due to anomalies in Ekman pumping, can advect cool, deep water into the mixed layer (Sato et al., 2010). Finally, wind bursts can force both ocean currents that advect heat horizontally (e.g. Waliser et al., 2003; Lau and Waliser, 2005; Cronin and McPhaden, 1997), as well as equatorial waves that cause propagating anomalies in thermocline depth (Lucas et al., 2010). To diagnose the relative impacts of these processes on the mixed-layer temperature, we computed the mixed-layer heat budget, which can be expressed as (e.g. Schiller and Godfrey, 2003; Jayakumar et al., 2010):

$$\frac{\partial T}{\partial t} = \underbrace{\frac{(Q_{net} - Q_{pen})}{\rho c_p h}}_{a} - \underbrace{\left(u\frac{\partial T}{\partial x} + v\frac{\partial T}{\partial y}\right)}_{b} - \underbrace{w_{Ek}\frac{\partial T}{\partial z} - \frac{\partial h}{\partial t}\frac{\Delta T}{h}\mathcal{H}}_{c} - \epsilon. \tag{IV.1}$$

The right-hand side of Eq. (IV.1) describes the different contributions to variations in mixed-layer temperature (T). Term a represents the corrected net heat flux forcing over the mixed layer, where h is the MLD and ρc_p is the volumetric heat capacity of seawater. Q_{net} is the total surface heat flux, equal to the sum of the shortwave, longwave, sensible and thermal heat fluxes ($Q_{net} = Q_{sw} + Q_{lw} + Q_{sh} + Q_{lh}$), where we have followed the convention that heat flux terms are positive when they warm the mixed layer. The correction term Q_{pen} denotes the fraction of shortwave radiation that penetrates through the bottom of the mixed layer and thus does not contribute to the heating. Term b represents the horizontal advection of heat into the mixed layer: u and v are the zonal and meridional surface currents, and $\partial T/\partial x$ and $\partial T/\partial y$ are the zonal and meridional temperature gradients. Term c describes the vertical fluxes of heat: advection (assumed to result from Ekman pumping) and vertical entrainment of deeper water into the mixed layer. Here, w_{Ek} is vertical Ekman velocity and ΔT is the difference in temperature between water within and just below the mixed layer. The vertical entrainment term is multiplied by the Heaviside function $\mathcal{H}$, which is equal to zero for a shoaling mixed layer ($\partial h/\partial t \leq 0$) and equal to 1 for a deepening mixed layer ($\partial h/\partial t > 0$). The residual, ϵ, includes turbulent entrainment and mixing at the base of the mixed layer, diffusion, advection from vertical velocities other then Ekman pumping, and errors.

On MJO timescales, the heat budget is somewhat more complicated because MJO anomalies act on the background state. For example, horizontal advection involves anomalous MJO current acting on both mean and MJO temperature gradients, as well as the mean current acting on anomalous temperature gradients that arise due to the MJO. It is thus necessary to consider all interactions between MJO anomalies and the background state. For each term ("X") in Eq. IV.1, the time-mean ($\bar{X}$) and the MJO ($\hat{X}$) components can be separated out. Then, the MJO heat budget can be ex-

pressed as

$$\begin{aligned}\frac{\partial \hat{T}}{\partial t} = & \left(\hat{Q}_{net} - \hat{Q}_{pen}\right) \frac{1}{\rho c_p (\overline{h} + \hat{h})} - \left(\overline{Q}_{net} - \overline{Q}_{pen}\right) \frac{\hat{h}}{\rho c_p \overline{h}^2} \\ & - \left(\overline{\mathbf{u}}.\nabla \hat{T} + \hat{\mathbf{u}}.\nabla \overline{T} + \hat{\mathbf{u}}.\nabla \hat{T}\right) \\ & - \left(\overline{w}_{Ek} \widehat{\frac{\partial T}{\partial z}} + \hat{w}_{Ek} \overline{\frac{\partial T}{\partial z}} + \hat{w}_{Ek} \widehat{\frac{\partial T}{\partial z}}\right) \\ & - \left(\frac{\frac{\partial \hat{h}}{\partial t} \Delta T}{\overline{h} + \hat{h}} - \overline{\left(\frac{\frac{\partial \hat{h}}{\partial t} \Delta T}{\overline{h} + \hat{h}}\right)}\right) \hat{\mathcal{H}} \\ & - \epsilon. \end{aligned} \tag{IV.2}$$

Eq. IV.2 includes MJO-MJO interactions as well as MJO-mean-state interactions. The last term on the first line is an approximation of the interaction of MJO variations in MLD and the mean net corrected heat flux. We are only interested in entrainment that results from MLD deepening on MJO timescales, so the entrainment term includes only the interaction between MJO variations in MLD and total ΔT, with the mean (rectified) component removed. The rectified component was also estimated for the vertical and horizontal advection terms and found to be negligible, and so is excluded from Eq. IV.2. For each variable X we computed the seasonal and interannual signals (X_{seas} and $X_{interann}$), then estimated the MJO signal as $\hat{X} = X - \bar{X} - X_{seas} - X_{interann}$.

IV.3.B Data sets

The terms in Eq. IV.2 involving mixed-layer temperature (T) and depth (h) were derived from Argo profile data, and the remaining terms came from gridded products, which are described in Table IV.1. The period of the MJO is approximately 50 days, so the eight phases of the Wheeler-Hendon MJO index are thus spaced, on average, about 6 days apart. (Note that the MJO does not oscillate regularly, so these are rough temporal approximations.) Argo floats make temperature and salinity measurements of the top 1000–2000 m of the water column, with ∼5 m vertical resolution, approximately every 10 days, so numerous Argo profiles are needed in order to observe the temporal evolution of an MJO event. Although gridded Argo products have been developed (e.g. Roemmich and Gilson, 2009b), these generally have monthly temporal resolution, which is too coarse to capture the evolution of the MJO and would also smooth out some of the intraseasonal signal. We thus used the raw data from around 54,000 Argo profiles made within the domain of the tropical Indian and western Pacific Oceans (50°E–180°E, 25°S–10°N). Most of these profiles were made between 2004 and 2010, but around 5% were made during 1999–2003, while the Argo program was being established.

The temperature measurement closest to the surface for each profile was used as a proxy for

mixed-layer temperature (T). To avoid erroneous mixed-layer depth estimates, profiles with fewer than five measurements within the top 100 m of the water column were discarded, as were profiles without measurements in the top 6 m. MLD for each profile was estimated following de Boyer Montégut et al. (2004) based on a density threshold criterion, where $\Delta\rho$=0.03 $\mathrm{kg\,m^{-3}}$ is the density difference from the measurement closest to a near-surface reference depth. Qualitatively, the results were not sensitive to the choice of reference depth, so 6 m was used in order to capture shallow mixed layers. The resulting MLDs were interpolated linearly to the nearest meter. We estimated $\partial T/\partial z$ from the local vertical temperature gradient observed at the depth of the mixed layer, and ΔT as the temperature at the MLD minus the temperature 10 m below the MLD. The dependence of the findings on $\Delta\rho$ is discussed in section IV.5.A.

The heat flux components making up Q_{net} came from the OAFlux and International Satellite Cloud Climatology Project (ISCCP) products (Table IV.1). The OAFlux surface latent and sensible heat fluxes are based on satellite measurements and several reanalysis products (Yu and Weller, 2007), and ISCCP surface shortwave and longwave radiation are derived using a radiative transfer model along with surface and atmospheric observations (Zhang and Dong, 2004). Kumar et al. (2010) compared several surface heat flux products with observations from Indian and Pacific Ocean moorings and found that the OAFlux and ISCCP products agree well with the observations of intraseasonal variability patterns. In section IV.6, we discuss the sensitivity of MJO heat budgets to the choice of flux product, and compare the OAFlux product with fluxes from the NCEP-2 reanalysis (Kanamitsu et al., 2002), European Centre for Medium-Range Weather Forecasts (ECMWF) ERA-interim reanalysis (ERA-I; Simmons et al., 2007), and Japanese Ocean Flux datasets with Use of Remote sensing Observations (J-OFURO; Kubota et al., 2002).

The shortwave radiation entering the ocean mixed layer was estimated using an albedo of 7% (Morel and Antoine, 1994). Q_{pen} was estimated following Morel and Antoine (1994) and Sweeney et al. (2005) as

$$Q_{pen}(h) = 0.57\,Q_{sw}(V_1 e^{-h/\zeta_1} + V_2 e^{-h/\zeta_2}), \tag{IV.3}$$

where V_1, V_2, ζ_1 and ζ_2 were estimated using chlorophyll-a observations from from the NASA Ocean Biogeochemical Model (NOBM), which is based on data assimilation of remotely-sensed chlorophyll-a (Gregg, 2008). Chlorophyll-a can vary at MJO timescales (Waliser et al., 2005; Vinayachandran and Saji, 2008), so the MJO can modulate Q_{pen} by variations both in MLD and in ocean chlorophyll. Unraveling these effects is beyond the scope of this study, particularly since Argo floats generally do not measure biological variables. Therefore, we evaluate Eq. IV.3 using seasonal-mean values of chlorophyll, so that Q_{pen} only varies spatially and with h.

The $\mathbf{u}$ terms in Eq. IV.2 were estimated from the Ocean Surface Current Analyses (OSCAR) surface current product, which is based on satellite winds and altimetric sea level anomaly data

Table IV.1: Gridded data sets and climatologies

Variable	Data source	Spatial resolution	Temporal resolution	Temporal range
SST	TMI	$0.25° \times 0.25°$	1 day	1998–present
Surface winds	CCMP	$0.25° \times 0.25°$	6 hour	1974–present
OLR	NOAA	$2.5° \times 2.5°$	1 day	1974–present
Turbulent heat fluxes	OAFlux	$1° \times 1°$	1 day	1985–present
Sensible heat fluxes	ISCCP	$1° \times 1°$	1 day	1983–2007
Surface currents	OSCAR	$1/3° \times 1/3°$	5 day	1992–present
Chlorophyll-a	NOBM	$5/4° \times 2/3°$	5 day	1998–2006
Surface and mixed-layer temperature	RG2009	$1° \times 1°$	1 month	2004–present
MLD, ILD	dBM2004	$2° \times 2°$	1 month	(climatology)

(Bonjean and Lagerloef, 2002). We compared the OSCAR data to in situ surface current observations from the TRITON/TAO and RAMA mooring arrays and found that generally the in situ zonal currents are significantly correlated with the OSCAR product on MJO timescales, but the meridional currents tend to be less well correlated, particularly along the equator (c.f. Johnson et al., 2007). Meridional surface currents at MJO timescales are generally weak ($<0.03\,\mathrm{m\,s^{-1}}$; Waliser et al., 2003), so this is not a large source of error in the overall analysis, although it may be locally important in some areas.

Ekman pumping, w_{Ek}, was estimated as $\nabla \times (\tau/f)\,\rho_s^{-1}$, where τ is wind stress, ρ_s is the density of seawater, and f is the Coriolis frequency. Winds were obtained from the level 3.0 gridded cross-calibrated multiple platform (CCMP) wind vectors, which are derived from numerous satellite products (Ardizzone et al., 2009). In addition, we used outgoing longwave radiation (OLR) data as a proxy for tropical convective activity, relying on the National Oceanic and Atmospheric Administration (NOAA) product (Liebmann and Smith, 1996). This is the same product that Wheeler and Hendon (2004) used to form the MJO index that the present study is based on. The gridded data sets have different spatial resolutions (Table IV.1), so each of the above fields was put on a common $2.5^\circ \times 2.5^\circ$ grid using a 2°-wide boxcar filter in each direction.

We estimated (T_{seas}+$T_{interann}$) from the gridded dataset produced by Roemmich and Gilson (2009b) (RG2009), which is based exclusively on Argo profiles and is available from 2004–present on a $1^\circ \times 1^\circ \times 1$-month grid. These data were low-pass filtered with a 120-day cutoff, then projected onto the exact time and position of each Argo profile using linear interpolation. This gave the expected background temperature component for each profile. For the profiles outside of the time-range of the RG2009 product (around 5% of the data used in the analysis), we projected the mean seasonal signal onto the float location and set $T_{interann}$ to zero. In the same manner, we projected the seasonal signals of MLD onto the time and location of each profile, using the gridded climatology from de Boyer Montégut et al. (2004) (dBM2004), which are based on objectively-mapped profile data from 1948–2008. To estimate the seasonal cycles of the variables derived from Argo ($\partial T/\partial z$, ΔT) as well as all of the gridded fields (Table IV.1), we fit annual and semiannual harmonics to the measurements in each grid box. For the gridded data we also used a 120-day lowpass filter to estimate the interannual signal. This filtering was not done for the derived Argo variables, as Argo profiles are irregularly distributed in time and space so filtering could have introduced biases. Generally, accurately estimating the seasonal signal, and to some extent the interannual signal, proved to be the greatest limitation to resolving the MJO signal: locations for which we could not successfully remove all of the background variability tended to yield poorer fits with large uncertainties.

IV.3.C MJO heat budget composites

To estimate the terms in the MJO heat budget (Eq. IV.2), we formed composites by averaging over numerous MJO events. The composites were defined using the Wheeler-Hendon MJO index (Wheeler and Hendon, 2004), which is based on the first two empirical orthogonal functions of the combined fields of OLR and 200-hPa and 850-hPa zonal winds averaged over 15°S–15°N. The index consists of a daily amplitude and phase, which is separated into eight discrete phases that represent the location of the active MJO. Although the MJO exhibits highly seasonal behavior due to the migration of the warmest SSTs, and thus convection, north and south of the equator (Zhang, 2005), the Wheeler-Hendon index is independent of season. Thermodynamic anomalies associated with the MJO are strongest in boreal winter (Wheeler and Hendon, 2004), so we restrict our analysis to November–April. The mean ocean conditions during this season are shown in Figure IV.1.

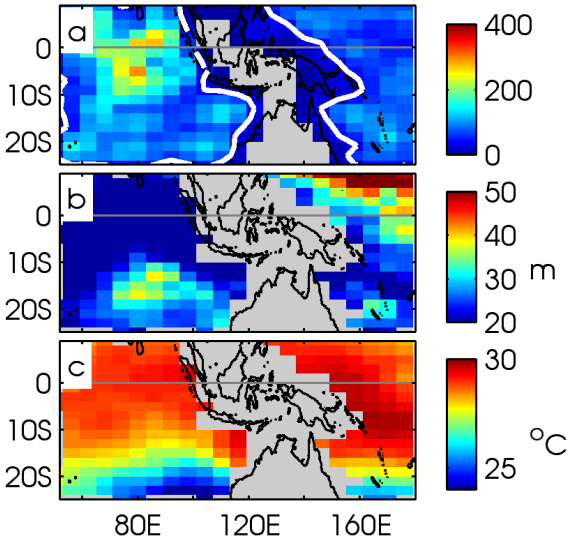

Figure IV.1: Boreal winter (November–April) mean fields estimated from Argo observations: (a) average number of Argo profiles used to form the MJO composites presented in this study, (b) MLD; (c) mixed-layer temperature. The grey shading in (a) indicates where zero Argo profiles were available, and the white contour indicates 40 profiles per grid box. In (b)–(c), grid boxes with fewer than 40 profiles are masked out in grey.

At each grid point (x_g,y_g), we formed composites of the individual variables in Eq. IV.2 by averaging over all measurements made during a given MJO phase. Only events for which the Wheeler-Hendon index had an amplitude greater than 1.5 were considered "significant" and used to form the composites; the results were largely insensitive to the choice of this threshold, although a value outside of the amplitude range 1–2 tended to degrade the composites. For the November–April

time period, there were generally 2–3 significant events per year.

Composites from the gridded data were formed by averaging all of the observations made within ±2 days of the significant MJO events. Compositing the Argo data was necessarily more involved because of the sparse and irregular temporal and spatial distribution of Argo profiles. To form statistically robust composites that captured the MJO spatial and temporal variability, it was necessary to include Argo profiles from a time-span and from grid boxes larger than those used for the gridded datasets. Instead of simply averaging the Argo data in each grid box, we fit a function to the observations and used it to extract information about the spatial and temporal patterns of MJO variability, including the MJO anomaly ($\hat{T}$, $\hat{h}$) and the gradient terms ($\partial T/\partial t$, $\partial T/\partial x$, $\partial T/\partial y$, $\partial h/\partial t$, etc.). Details about this procedure are given in the appendix. Using grid boxes defined by ±6° in longitude and ±2° in latitude, there were around 100–300 Argo profiles per grid box per phase that could used for the regressions (Figure IV.1a). No Argo floats have measured within the Indonesian archipelago, so the signal there could not be estimated in this study. The floats provide patchy spatial coverage of the floats in some regions, which can introduce artifacts in the composite maps. For example, if one region contains fewer profiles compared to the adjacent regions, fewer data points will be used in the regression and the fit there will be worse; this can result in misleading patchiness in the observed spatial patterns. We thus restrict our analysis to grid boxes where more than 40 Argo profiles were available for the regressions (white contour in Figure IV.1a).

For each variable, we used the standard error of the composite to represent the uncertainty. The uncertainties thus take into account the variation across different MJO events, which can be large, but not any systematic biases in the data. Errors in the satellite-derived quantities were generally small because the great availability of data allowed us to composite over many events. In contrast, Argo profiles are sparsely distributed in space and in time, so there are large uncertainties in the estimates derived from Argo data. This is particularly noticable in regions where there are few profiles (Figure IV.1a) or where the variance between MJO events is large.

IV.4 Spatial patterns of MJO variability

IV.4.A MJO surface forcing

Figure IV.2 shows the progression of the MJO in terms of anomalous heat fluxes and winds based on the Wheeler-Hendon MJO index (c.f. 8 of Wheeler and Hendon, 2004). To highlight the significant patterns of variability, regions for which the composite average is smaller than the standard error have been stippled. It is important to keep in mind that the compositing procedure smooths out the variability of the MJO signal considerably: not only is there great variation in the amplitude of individual MJO events, but the duration and structure of events are highly variable

as well. The eastward propagation of thick convective cells (negative OLR), flanked on both sides by clear skies, that characterizes the MJO is evident (Figure IV.2a). The active MJO signal is strongest over the central and eastern Indian Ocean in phases 3–4 (OLR anomalies $<$–30 $\mathrm{W\,m^{-2}}$). In phases 5–6 the convective anomalies move eastward over the Indo-Pacific warm pool, at which point they weaken and move southward. By phases 7–8, the convective anomalies have reached the eastern Pacific and weakened considerably (OLR$\sim$–18 $\mathrm{W\,m^{-2}}$); at the same time, the suppressed MJO conditions are strongest, with positive OLR anomalies (25 $\mathrm{W\,m^{-2}}$) extending from the central Indian to the western Pacific Ocean. The OLR $\pm$5 $\mathrm{W\,m^{-2}}$ contour is shown in order to highlight the regions where the MJO convective forcing is strongest and therefore the mixed-layer response is expected to be large. Correlations and regressions presented later in this study are restricted to grid boxes for which OLR exceeds this threshold. Rainfall was estimated using the Global Precipitation Climatology Project (GPCP) product, which are estimated from a combination of satellite and in situ measurements (Adler et al., 2003, ; not shown). Variations in precipitation associated with anomalous MJO convection is much larger than variations in evaporation, so the MJO patterns of freshwater flux (precipitation minus evaporation, or P–E) closely resemble those of convection (Figure IV.2a), with the strongest rainfall anomalies over the Indo-Pacific warm pool during phases 4–6.

Zonal wind anomalies also show a systematic MJO signal: strong westerly wind anomalies ($\sim$3.5 $\mathrm{m\,s^{-1}}$) are associated with the active MJO, and slightly weaker easterly wind anomalies ($\sim$–2.5 $\mathrm{m\,s^{-1}}$) with the suppressed MJO (Figure IV.2b). To first order, total MJO heat flux variations are controlled by perturbations in the shortwave and latent heat flux caused, respectively, by variations in convection and winds (Woolnough et al., 2000), so the phase relationship between convection and winds has important consequences for the patterns of net heat flux and thus the MJO mixed-layer temperature trend. Zhang and McPhaden (2000) describe two models for MJO forcing. In model 1, maximum westerly winds lag (i.e., are to the west of) the peak convection, so there are two active forcing regimes: one beneath the peak westerlies, where latent heat loss and wind stirring are strong, and one beneath the convective center, where incoming solar heat flux is anomalously low. In model 2, the peak MJO westerlies and convection are co-located and there is a single forcing regime. Model 2 tends to cool (and heat) the ocean more efficiently, since the convection and winds act in phase. Hendon and Salby (1994) and Shinoda et al. (1998) found that the wind-convection phasing resembles model 1 in the equatorial Indian Ocean and model 2 in the western Pacific Ocean. Indeed, comparing Figure IV.2a and Figure IV.2b reveals that in the Indian Ocean anomalous OLR tends to lead anomalous zonal wind, whereas in the Pacific Ocean they are more closely aligned. However, variations in latent heat flux are controlled by anomalies in the magnitude of the wind stress (rather than the zonal wind), which have a more complicated phasing relationship with convection

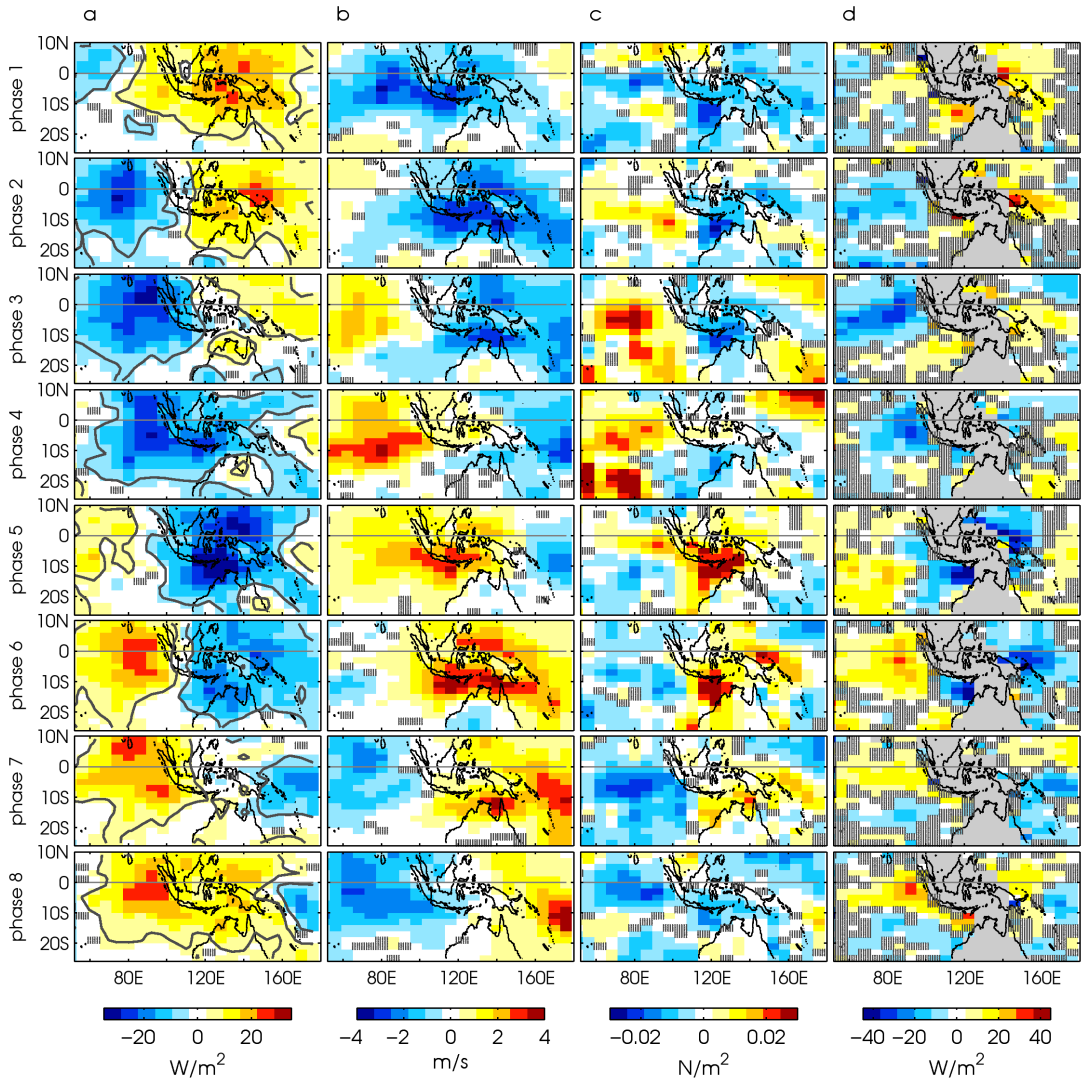

Figure IV.2: Composites of November–April MJO anomalies based on the index of Wheeler and Hendon (2004): (a) outgoing longwave radiation (OLR) from NOAA data; (b) zonal wind speed from CCMP winds; (c) wind stress magnitude from CCMP winds; (d) Q_{net} from the OAFlux product. Each column shows the progression of the MJO through each of the eight phases defined by the Wheeler-Hendon index. Regions where the composite value is less than the standard error are stippled. In (a) OLR = ± 5 W m^{-2} contours are shown: the regions where OLR anomalies exceed this threshold are considered to have significant MJO-related variability and are used in the subsequent analysis for estimating correlations between different fields.

(Figure IV.2c). The spatial patterns of anomalous wind stress magnitude (Figure IV.2c) have a coherent spatial signal at MJO timescales, but the propagation that characterizes the zonal wind and convective anomalies is less evident. While anomalous convection marches steadily eastward during the course of the MJO, the strongest anomalies in wind stress remain relatively stationary over the southwestern tropical Indian Ocean during phases 2–4, then over the region between northern Australia and Java ("northwestern Australian Basin") during phases 5–7. In this region, MJO convective and wind anomalies are consistently out of phase with the rest of the Indian Ocean basin, and much more closely resemble conditions in the far western Pacific Ocean, where forcing is also strong in phases 5–7. While zonal wind anomalies generally have a roughly coherent spatial structure throughout the western Pacific Ocean (Figure IV.2b), patterns of anomalous wind stress magnitude are more complicated (Figure IV.2c). There is a band of anomalous wind stress magnitude found to the northeast of Papua New Guinea and the Solomon Islands that has a distinctively different sign and magnitude from the surrounding regions in any given phase (Figure IV.2c). As a result, wind stress varies over relatively small spatial scales in the western Pacific Ocean, and the phasing with convection is complicated. Consequently, neither of the two models described by Zhang and McPhaden (2000) can easily explain the response of the upper ocean to MJO forcing.

The signature of the MJO is apparent in the net heat flux (Q_{net}; Figure IV.2d): large negative anomalies, indicating heat loss from the ocean surface, propagate eastward in concert with the active MJO, with maximum amplitudes (–25 $\mathrm{W\,m^{-2}}$) in phases 4–5 over the equatorial Indo-Pacific region. The patterns resemble those of OLR (Figure IV.2a), suggesting that they may be more strongly controlled by convective anomalies than by winds.

By the time the MJO reaches the central Pacific Ocean, anomalous convection and winds have weakened considerably (Wheeler and Hendon, 2004), and the processes governing mixed-layer dynamics at MJO timescales are different than those in the Indian and western Pacific Oceans (Maloney and Kiehl, 2002; McPhaden, 2002; Lucas et al., 2010). For example, oceanic Kelvin waves that are generated in the western Pacific Ocean by MJO wind bursts and then propagate eastward along the equator exert a strong influence on the eastern equatorial Pacific Ocean at MJO timescales (Kessler et al., 1995). Roughly around the dateline, there appears to be a shift in the relative importance of one-dimensional versus dynamical processes on the MJO mixed-layer signature (McPhaden, 2002; Lucas et al., 2010). Thus, in the present study we limit our analysis to the Indian and Pacific Ocean west of the dateline, where MJO surface forcing is large.

IV.4.B Mixed-layer response to MJO forcing

The anomalous response of the mixed layer to MJO forcing is shown in Figure IV.3. Composite MJO anomalies of MLD exhibit systematic variations, particularly in the Indian Ocean, with

amplitudes of up to around ±10 m (Figure IV.3a). The spatial structures of MLD generally resemble those of wind stress (Figure IV.2c) and net heat flux (Figure IV.2d), consistent with the model that diabatic cooling and wind stirring during the active MJO both contribute to mixed-layer deepening, and surface warming, and light winds during the suppressed MJO allow the mixed layer to shoal. The patterns of MLD variations are largely coherent over the Indian Ocean, but less so in the Pacific Ocean. This may be because the MJO forcing varies over fairly small spatial scales in this region. Alternatively, it may be that Argo data fail to accurately capture particularly shallow MLDs that can arise when there is a large diurnal signal, as is the case here (Bellenger and Duvel, 2009), so the signal gets smoothed out. It may also reflect the influence of other processes that are modulated by the MJO, such as precipitation, horizontal ocean dynamics, or Ekman pumping.

Composite mixed-layer temperature anomalies also display strong, systematic spatial and temporal patterns of MJO variability (Figure IV.3b). Throughout the Indian Ocean and in the equatorial Indo-Pacific region, the mixed-layer temperature patterns are similar to those of MLD (Figure IV.3a) but with the opposite sign: mixed layers are anomalously cool during the active MJO, and anomalously warm during the suppressed MJO. These patterns are consistent with the model that heat flux anomalies drive the mixed-layer temperature signal. Although the mixed-layer temperature signal is weaker in the Pacific Ocean than in the Indian Ocean, it varies systematically at MJO timescales, again consistent with being driven by net heat flux, which is largely coherent in the western Pacific Ocean (Figure IV.2d). The largest MJO temperature signal (peak-to-peak amplitude of around 0.7°C) is seen in the northwestern Australian basin region, as has been observed previously (Duvel and Vialard, 2007), where wind stress and heat flux anomalies are both strong (Figure IV.2c,d). The mixed-layer temperature here is warmest one phase later than the peak positive heat flux and at the same time as the weakest winds. Similarly, the coldest temperatures are seen to lag the anomalous negative heat flux.

IV.4.C MJO heat budgets

To assess which processes contribute to the observed trends in mixed-layer temperature, we formed composite maps of the individual heat budget terms (Eq. IV.2), with the exception of the vertical advection term, which is negligible (magnitude $<0.001°\mathrm{C\,day^{-1}}$) in all regions. The MJO mixed-layer temperature trend (Figure IV.4a) is clearly driven by anomalies in heat flux (Figure IV.4b): the large-scale patterns in the two fields match closely, although the magnitude of the temperature tendency is, on average, around 73% that of the net corrected heat flux term (Table IV.2). The correlation between the two fields, calculated using all statistically significant observations for which the magnitude of the OLR anomaly was greater than $5\ \mathrm{W\,m^{-2}}$ (Figure IV.2a), was R^2=0.38 (compared to a 95% significance level of R^2=0.05). This confirms that the corrected

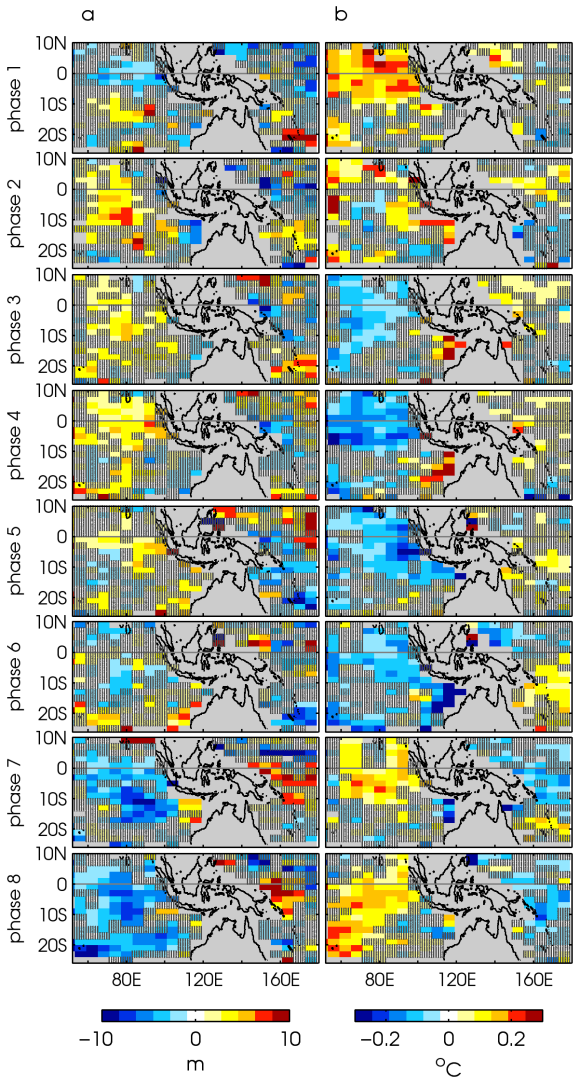

Figure IV.3: Composites of November–April MJO anomalies based on the index of Wheeler and Hendon (2004) and data from Argo profiles: (a) mixed-layer depth; (b) mixed-layer temperature. Grid boxes where fewer than 40 profiles were available to compute the regressions have been masked out in grey; regions where the composite value is less than the standard error are stippled.

heat flux forcing indeed represents a significant portion of the observed MJO variance in $\partial T/\partial t$, but suggests that other processes may also be important. One notable exception is seen during phase 1 throughout the Indian Ocean, when the heat flux forcing is positive ($\sim$0.01°C day^{-1}) but the mixed-layer temperature trend is negative ($\sim$–0.008°C day^{-1}).

Table IV.2: Regression coefficient (κ) and R^2 between mixed-layer temperature tendency ($\partial T/\partial t$) and individual heat budget terms. Regressions are based on MJO composite observations at all grid points where the magnitude of the OLR anomaly exceeds 5 W m^{-2} (Figure IV.2a). The first four rows in the table show the breakdown between each of the flux components; the remaining rows correspond to the individual terms in the heat budget (Eq. IV.2). The 95% significance level is R^2=0.05. The regression coefficient explains the fraction of the $\partial T/\partial t$ signal explained by each term.

.

term	κ	R^2
$(Q_{sw} - Q_{pen})(\rho c_p h)^{-1}$	0.71	0.38
$Q_{lh}(\rho c_p h)^{-1}$	0.17	0.13
$Q_{sh}(\rho c_p h)^{-1}$	-0.17	0.37
$Q_{lw}(\rho c_p h)^{-1}$	0.04	0.26
$(Q_{net} - Q_{pen})(\rho c_p h)^{-1}$	0.73	0.35
vert. entrainment	0.10	0.05
horiz. advection	0.02	0.03
vert. advection	0.005	0.01
residual	0.15	0.02

The net heat flux signal is dominated by anomalies in shortwave radiation, which result from anomalous MJO convection. Calculated over the whole domain, the regression coefficient between the shortwave heat flux retained by the mixed layer (i.e., corrected for Q_{pen}) and $\partial T/\partial t$ is 0.71, compared to latent and sensible heat fluxes, which effectively cancel each other out, and longwave heat flux, which accounts for less than 5% of the observed $\partial T/\partial t$ signal (Table IV.2). Uncertainties for the heat flux composites are negligible, but do not capture any errors that are inherent to the heat flux estimates themselves. This will be discussed in section IV.6.

Horizontal advection exhibits systematic variations on MJO timescales on the order of 0.005°C day^{-1}(Figure IV.4c). These are almost entirely due to anomalous currents excited by the MJO, which act on the mean temperature gradient (e.g., Figure IV.1c). MJO horizontal advection anomalies contribute, on average, less than 2% to the observed variability in $\partial T/\partial t$ (Table IV.2). In the central Pacific Ocean east of around 160°E, strong anomalous wind bursts associated with the MJO excite zonal surface jets along the equator (e.g. Kessler et al., 1995), advecting heat zonally at a rate of up to $\pm$0.01°C day^{-1}, which is comparable to the local temperature tendency (Figure IV.4a).

Overall, including horizontal advection in the domain-wide MJO heat budget (i.e. adding term b to term a in Eq. IV.1) does not improve the budget closure by a significant amount (not shown). In other words, though significant in the central Pacific Ocean, advection is generally at most a second-order correction to the heat budget at MJO timescales in the western Pacific and Indian Ocean basins.

Vertical entrainment also contributes little to the canonical MJO mixed-layer heat budget (Figure IV.4d, Table IV.2). Although both the temperature jump at the base of the mixed layer (ΔT) and the deepening of the mixed layer ($\partial h/\partial t$) can be considerable, the regions where these terms are largest are not co-located, so the composite entrainment term is small (order $0.005°\mathrm{C\,day^{-1}}$). Furthermore, the uncertainty in $\partial h/\partial t$ is the same order as the signal itself, so entrainment is generally not statistically significant (Figure IV.4d). The only widespread, significant entrainment cooling occurs in the central Indian Ocean during the onset of the active MJO in phase 1. Here, both wind stirring and diabatic cooling appear to contribute to the rapid deepening of the mixed layer (up to $1\ \mathrm{m\,day^{-1}}$), as can be inferred by comparing the phase 1 forcing patterns (Figure IV.2c,d) with the phase 1–2 shift in the mixed-layer response (Figure IV.3). This basin-scale entrainment cooling appears to account for the large discrepancy between the temperature tendency and the heat flux forcing in this phase (Figure IV.4a,b). Entrainment cooling is also large, though not statistically significant, in the northwestern Australian basin during the transition to the active MJO in phases 4–5. Thus, while entrainment cooling on average does not play a leading role in MJO variations in heat storage, it has a significant impact on the mixed-layer temperature of the Indian Ocean during the cooling phase of the MJO. Note that in individual profiles ΔT can be negative, indicating a temperature inversion (e.g. due to the presence of a barrier layer; c.f. Anderson et al., 1996); however, in the composites ΔT is positive everywhere (not shown) and vertical entrainment always has a cooling effect.

IV.5 Implications of MLD variations associated with the MJO

Shinoda and Hendon (1998) used a one-dimensional mixed-layer model to show that MJO variations in MLD can affect the mixed-layer heat content of the western Pacific Ocean by way of two mechanisms. First, since the net heat flux anomaly is integrated over the mixed layer, variations in MLD can modulate the heat flux forcing ("scaling effect"); and second, variations in MLD can affect how much of the incoming solar heat flux is lost through the base of the mixed layer (Eq. IV.3; "penetrative effect"). We assess the basin-wide implications of the MJO variations in MLD (Figure IV.3a) by estimating how these two processes modify the heat flux forcing (i.e., term a

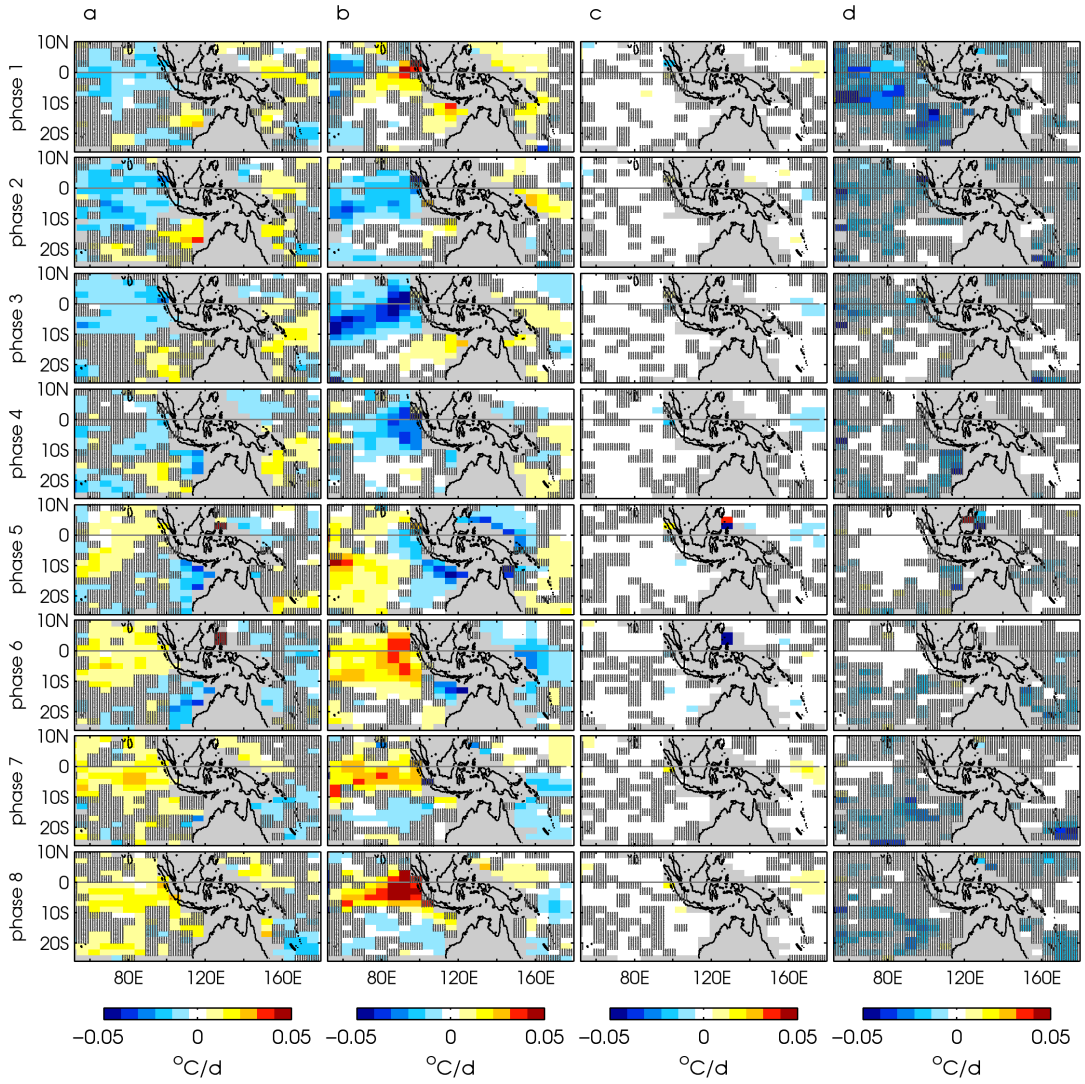

Figure IV.4: Composites of November–April MJO heat budget terms: (a) $\partial T/\partial t$; (b) corrected net heat flux forcing; (c) horizontal advection; and (d) vertical entrainment. Positive values indicate mixed-layer heating. MJO phases 1–8 are based on the Wheeler and Hendon (2004) index. Grid boxes where fewer than 40 profiles were available to compute the regressions have been masked out in grey; regions where the composite value is less than the standard error are stippled.

in Eq. IV.1). The scaling effect is estimated as the difference between the net heat flux forcing computed using only the seasonal mean MLD ($\bar{h}$) and using the seasonal mean plus MJO-varying MLD ($\bar{h}+\hat{h}$). As noted by Shinoda and Hendon (1998), negative net heat fluxes are associated with deep mixed layers and positive heat fluxes with shallow mixed layers (Figure IV.2d and Figure IV.3a), so the scaling effect nearly always results in a warming pattern (Figure IV.5a). The scaling effect is only significant over large spatial scales in the central equatorial Indian Ocean during both the peak active and suppressed MJO (phases 2–4 and 7–8), where it has a magnitude of around $0.01°\mathrm{C\,day^{-1}}$.

In comparison to using a fixed MLD, using a variable MLD to compute Q_{pen} results in a warmer mixed layer during the active MJO and a cooler mixed layer during the suppressed MJO (Figure IV.5b), also consistent with the findings of Shinoda and Hendon (1998). This is because more heat is lost through the bottom of the shallow mixed layers that occur during the suppressed MJO, and less through the deep mixed layers of the active MJO. The penetrative effect is strongest in the central Indian and far western Pacific Oceans, where MLD variations are large (Figure IV.3a). Both the scaling and penetrative effects have the same sign during the active MJO, so the net result of a variable MLD is greater than $+0.01°\mathrm{C\,day^{-1}}$ during the active MJO (phases 2–4 in the Indian Ocean and phases 7–8 in the western Pacific Ocean; Figure IV.5c). In comparison, the total heat flux anomaly is around –0.02°C (Figure IV.4b); in other words, using a fixed MLD in the central Indian and far western Pacific Oceans overestimates the size of the heat flux forcing by up to 50% during the active MJO. During the suppressed MJO, the relative cooling from the penetrative effect is partly mitigated by the warm scaling effect, and so in the central Indian using a variable MLD produces a net corrected heat flux that is up to 0.01°C cooler in comparison to using a fixed MLD. North of around 10°S in the central Indian Ocean, net heat flux forcing is around 0.04°C in phases 7–8 (Figure IV.2d), which implies that using a seasonal-mean mixed layer to estimate the heat flux forcing results in an overestimation of ∼25% here. South of 10°S the MJO heat flux into the mixed layer reverses sign (Figure IV.2d) so using a mean MLD underestimates the negative heat flux forcing. These findings are in contrast to Jayakumar et al. (2010), who found that using a mean MLD did not affect the agreement between heat flux forcing and mixed-layer heat storage by an appreciable amount in the central Indian Ocean.

In this study we have estimated Q_{pen} using seasonal-mean chlorophyll (Eq. IV.3). However, ocean chlorophyll concentration can vary at MJO timescales (Waliser et al., 2005; Vinayachandran and Saji, 2008; Resplandy et al., 2009): the active MJO is associated with an increase in chlorophyll, which tends to decrease Q_{pen} (Eq. IV.3). We estimated this effect by forming MJO composites of the NOBM chlorophyll-a product (Gregg, 2008) and calculating the resulting change in Q_{pen}. In the active phase, MJO chlorophyll variations reduce Q_{pen} by a maximum of around 5%, and in the suppressed phase they increase Q_{pen} by less than 5% (not shown). Since Q_{pen} has around a 10–20%

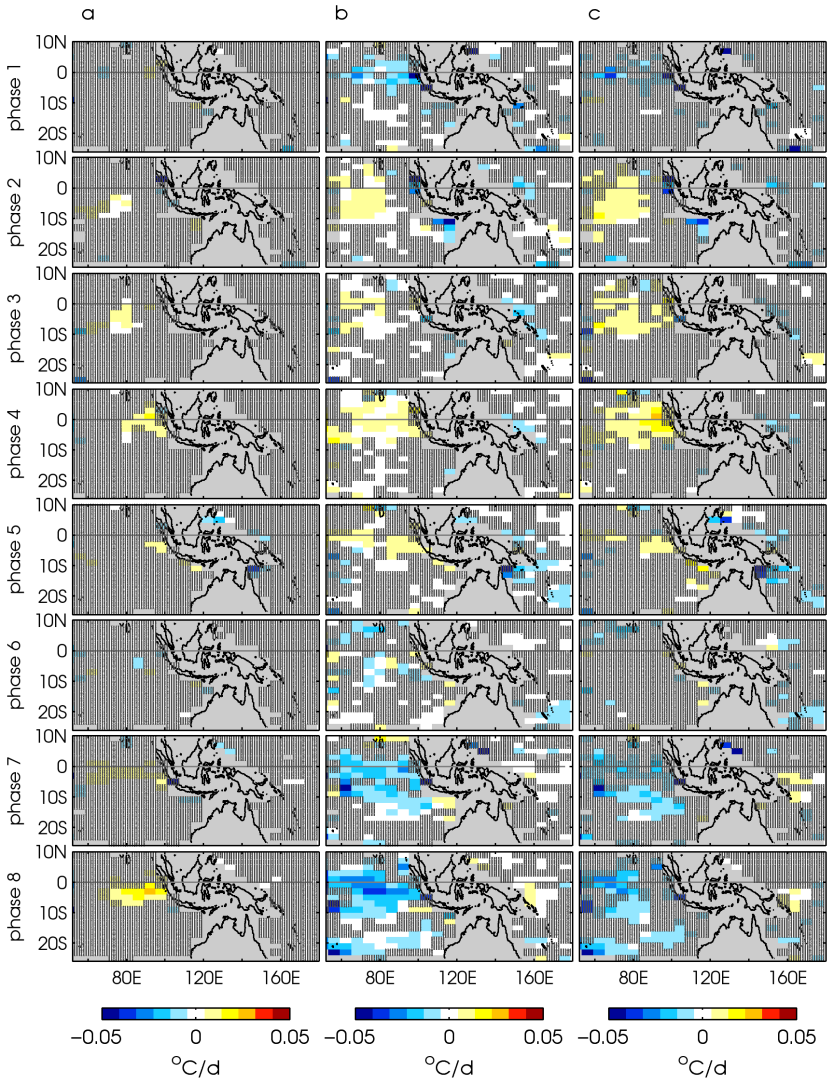

Figure IV.5: Composites illustrating the effect on mixed-layer heat forcing due to MJO MLD variations: (a) difference between $Q_{net}/\rho c_p h$ for variable and fixed MLD; (b) difference between $Q_{pen}/\rho c_p h$ for variable and fixed MLD; (c) sum of these two effects, representing the net effect of MJO MLD variations on the mixed-layer heat budget. Positive values indicate that MLD variations on MJO timescales result in a warmer mixed layer in comparison to a fixed MLD. Grid boxes where fewer than 40 profiles were available to compute the regressions have been masked out in grey; regions where the composite value is less than the standard error are stippled. The color scaling is the same as used in the plots of the heat budget terms (Figure IV.4).

impact on the net heat flux forcing, we conclude that chlorophyll variations do not significantly affect the heat budget on MJO timescales. However, they may have other consequences, for example on fisheries productivity (Waliser et al., 2005).

IV.5.A Sensitivities and uncertainties

IV.5.B Uncertainties on heat budget terms

Figure IV.6a,b show the budget residual (ϵ in Eq. IV.2) and the total error map on the heat budget estimate (advection and entrainment terms in Eq. IV.2). The heat budget is closed where the magnitude of the residual is smaller than the error; over most of the domain, this is not observed. The residual was in many cases on the same order as the mixed-layer temperature tendency itself (Figure IV.4a). This is unsurprising: there are many feedbacks and scale interactions, and the phasing between winds and convection can vary from one event to the next, so mixed-layer temperature variations at MJO timescales are not expected to respond perfectly linearly to MJO forcing. Though the goal of this study was not to close the heat budget but rather to examine the dynamical processes that contribute to mixed-layer temperature variations on MJO timescales, it is still enlightening to explore some of the potential sources of error in the heat budget estimates.

In most cases, the amplitude of the anomalous net heat flux is larger than the observed temperature tendency (Figure IV.4a,b). One possibility is that extracting the temperature tendency from the relatively sparse set of Argo profile data underestimates the variance in comparison to the heat flux composites, which were based on many more data points. We tested this by estimating $\partial T/\partial t$ from the satellite-derived TMI SST data and comparing it to the estimate from Argo (section IV.3IV.3.B), and found that both methods yield results with similar variance. Moreover, the difference between the two estimates of $\partial T/\partial t$ does not vary systematically at MJO timescales. Since these are two completely independent data sets, these findings suggest that in spite of the irregular spatial and temporal distribution of Argo profiles, estimating the temperature tendency using the regression technique does not produce a systematic bias. However, in certain locations (e.g., the far western Pacific warm pool) the fits to Argo mixed-layer temperatures differ significantly from the fits to TMI SST, suggesting that the MJO temperature signal there may be difficult to capture accurately.

The composite budgets do not take diurnal variability into account. Since Argo profiles sample the mixed layer at random times of the day, measurements of mixed-layer temperature and depth may be noisy in regions where diurnal variations are large (for example, between northern Australia and Java and in the western Pacific warm pool; Bellenger and Duvel, 2009). Convection and winds affect the ability of the upper ocean to form diurnal warm layers, so the MJO itself

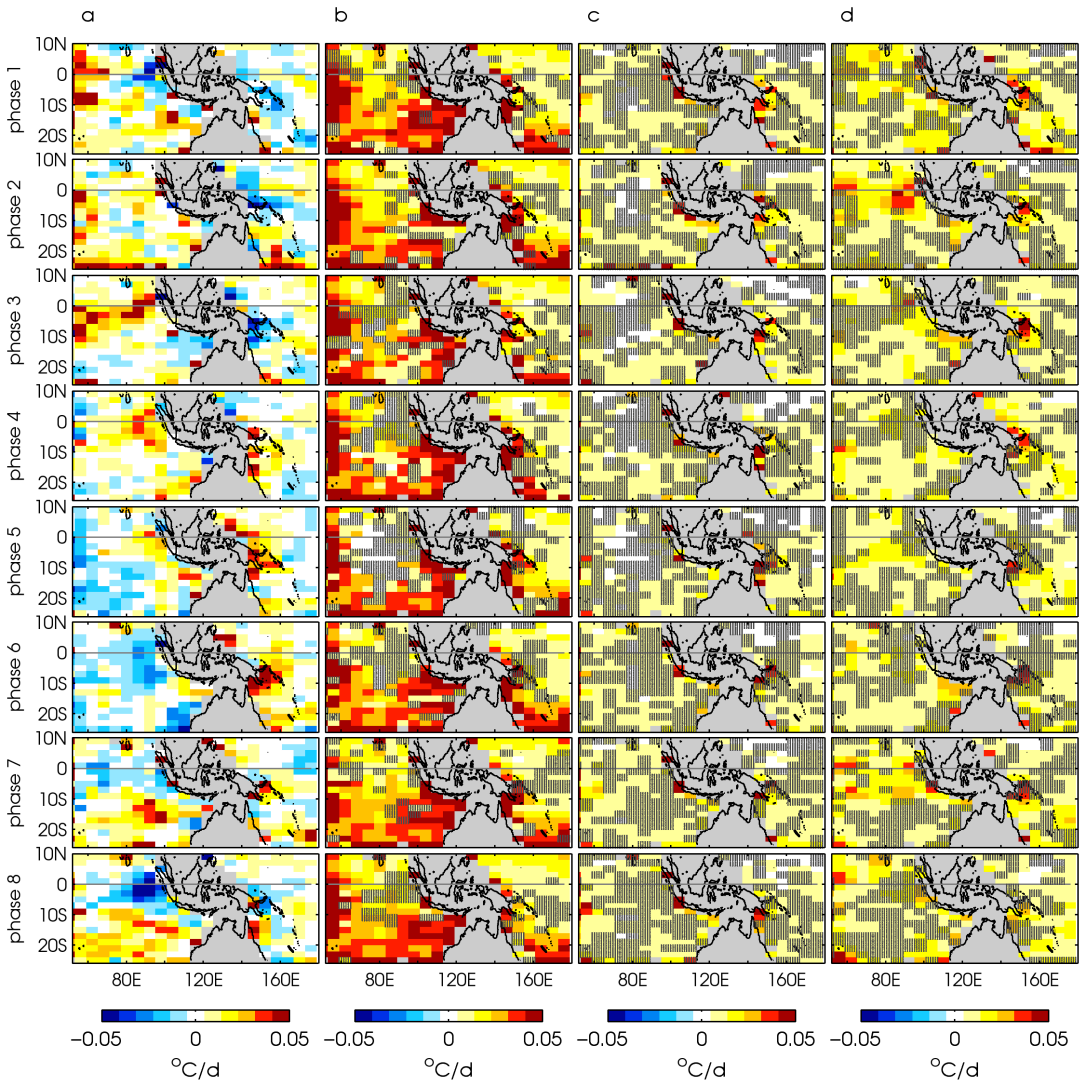

Figure IV.6: Uncertainties associated with the composite November–April MJO heat budget: (a) residual (ϵ); (b) error map for all terms in the MJO heat budget (Eq. IV.2) except for ϵ ($\partial T/\partial t$, heat flux forcing, horizontal and vertical advection, and entrainment). The heat budget is considered to be "closed" when the amplitude of the residual is smaller than this term; (c) same as (b) but excluding the error s from vertical entrainment; (d) same as (c), but instead of representing the uncertainty on net heat flux as the standard error from the composite, the uncertainty was estimated as the standard deviation over four heat flux products. In (b)–(d), regions where the budgets are not closed, based on the error map shown, have been stippled. MJO phases 1–8 are based on the Wheeler and Hendon (2004) index. Grid boxes where fewer than 40 Argo profiles were available have been masked out in grey.

may modulate the amplitude of the diurnal signal, further complicating the picture (Bellenger and Duvel, 2009). The interplay between diurnal and intraseasonal variations is emerging as a potentially important mechanism in MJO dynamics (Shinoda and Hendon, 1998; Bernie et al., 2005; Woolnough et al., 2007; Bernie et al., 2008), but Argo floats do not sample with sufficient vertical resolution or at shallow enough depths to adequately resolve the diurnal signal, so we do not attempt to unravel these processes in the present study.

The uncertainty of the vertical entrainment term is generally larger than the signal itself (Figure IV.4d). This is due to the large errors in the estimate of $\partial h/\partial t$ from the Argo profile data, which likely arise because the climatology used to remove the background signal from the MLD observations (de Boyer Montégut et al., 2004) does not account for interannual variations in MLD. Thus, it is only because of the large uncertainties in entrainment that the heat budget can be closed in most regions (Figure IV.6b). If the entrainment term is removed from the budget entirely, the total uncertainty in the heat budget estimate is substantially lower, and as a result the magnitude of the residual generally exeeds the uncertainty and the budget is not closed (Figure IV.6c).

There also may be large errors on the advection terms. The strength of horizontal advection depends on the location of surface current anomalies relative to the mixed-layer temperature gradient, which can vary interannually (e.g., in the western Pacific Ocean due to ENSO), so averaging reduces the signal considerably. However, since the advection and entrainment terms are generally small (Figure IV.4c,d), it seems unlikely that errors in these terms are large enough to account for the budget residual in all phases and locations.

Alternatively, inaccuracies in how MLD is estimated could introduce a bias into the scaling of the heat flux term (Eq. IV.2). As described in section IV.3IV.3.B, we estimated MLD from each profile based on a density difference of $\Delta\rho$=0.03 kg m^{-3} from a 6 m reference depth. Definining MLD using a larger value of $\Delta\rho$ produces systematically deeper mixed layers, and therefore a smaller net heat flux forcing term. However, close examination of numerous Argo profiles revealed that the 0.03 kg m^{-3} threshold generally captures the MLD well, and larger values of $\Delta\rho$ tend to overestimate MLD. We therefore rule out the choice of $\Delta\rho$ as an important source of error in the heat budget budget.

IV.5.C Comparison of heat flux products

Heat flux estimates are notoriously difficult to estimate accurately, and the various model reanalysis and observations-based products in general suffer from a lack of validation (Kumar et al., 2010). We evaluate the uncertainty in the heat flux term of our heat budget by computing MJO composite net heat flux maps using the NCEP-2 reanalysis, ECMWF ERA-I reanalysis, and J-OFURO, along with the OAFlux product that was used for the budget. All products produce

the same qualitative patterns (i.e., Figure IV.2d, Figure IV.4b), but quantitively they vary. The advection and entrainment terms are generally small compared with $\partial T/\partial t$, so it is reasonable to evaluate the performance of the heat flux product by comparing it to $\partial T/\partial t$. This was done using several statistical tests: relative variance; correlation (R^2); regression coefficient; and root-mean-square difference (RMSD). The results are summarized in Table IV.3. For all products, correlations between heat flux and MJO temperature tendency are low but significant (95% confidence level is R^2=0.05). The variance of the OAFlux product is much higher than that of any other product, suggesting that it most successfully captures the energy of heat flux variations at MJO timescales. The regression coefficients indicate that all products except for ERA-I overestimate the amplitude of the MJO heat flux forcing and that J-OFURO captures the amplitude well; $\partial T/\partial t$ represents ∼80% of the corrected net heat flux for OAFlux. The RMSD values are large for all products (order $0.01^{\circ}\mathrm{C\,day^{-1}}$, comparable to the signal size), but smallest for OAFlux. From this analysis we conclude that OAFlux is a good choice for capturing the mixed-layer temperature signal at MJO timescales, with ERA-I also performing well and NCEP-2 consistently the worst. There were only slight regional variations in the results (not shown); notably, OAFlux was substantially better than all other products in the western Pacific warm pool. These findings are consistent with the study by Kumar et al. (2010), who compared numerous heat flux products in the Seychelles-Chagos thermocline ridge region.

The small uncertainty in the net heat flux term used in the budget (Figure IV.4b) reflects only variability across multiple events and does not take systematic biases into account. A more accurate representation of the uncertainty in the net heat flux can be obtained by first estimating the composite net heat flux using multiple flux products (Table IV.3), then calculating the standard deviation across the different products. When this is done, the error maps for the budget are much larger, and the budget can be closed within the estimated uncertainty (Figure IV.6d). This illustrates that heat flux is the largest unknown in the MJO heat budget.

IV.6 Summary

Composites of mixed-layer temperature, depth, and heat budget terms (Figure IV.3, Figure IV.4) have given some insight into the roles of various dynamical and thermodynamical processes that affect mixed-layer dynamics on MJO timescales in the tropical Indian and western Pacific Oceans. Although many previous studies have addressed similar questions, the present study is novel in that it is the first to use in situ mixed-layer observations to characterize the MJO signal throughout the domain. We have shown that during the boreal winter, the MJO excites coherent variations in mixed-layer depth and temperature throughout the domain, with peak-to-peak com-

Table IV.3: Comparison of net heat flux forcing and mixed-layer temperature tendency for different heat flux products. Computations have been made using MJO composite observations over all regions where the magnitude of the OLR anomaly exceeds 5 $\mathrm{W\,m^{-2}}$ (Figure IV.2a). Relative variance is computed as the variance of $\partial T/\partial t$ divided by the variance of the corrected net heat flux. The 95% significance level is R^2=0.05. The regression coefficient, κ, is computed as $\partial T/\partial t = \kappa(Q_{net} - Q_{pen})(\rho c_p h)^{-1}$. RMSD stands for root-mean-square difference.

	Relative variance ($^\circ\mathrm{C\,day^{-1}}$)	R^2	κ	RMSD ($^\circ\mathrm{C\,day^{-1}}$)
OAFlux	0.44	0.35	0.73	0.013
J-OFURO	0.21	0.19	0.89	0.019
ERA-I	0.21	0.28	1.10	0.018
NCEP-2	0.29	0.12	0.57	0.018

posite amplitudes of more than 15 m and 0.7°C, respectively. MJO MLD variations are largest in the central Indian Ocean and the western Pacific Ocean, and mixed-layer temperature anomalies are largest in the northwestern Australian basin (between Java and Australia) and Seychelles-Chagos thermocline ridge (around 5°S–10°S, 60°E–90°E) regions (Figure IV.3). Our observations are generally consistent with the model that the mixed layer deepens and cools during the active, cloudy-windy phase of the MJO, and shoals and warms during the clear-sky, low-wind conditions of the suppressed phase. This is particularly evident throughout the Indian Ocean, where anomalies in wind stress and net heat flux are nearly in phase and vary systematically throughout the lifecycle of the MJO (Figure IV.2c,d). In contrast, the phasing between MJO anomalies in wind stress and heat flux is more complex in the Pacific Ocean, and as a result the mixed-layer temperature and depth anomalies vary over smaller spatial scales.

The mixed-layer heat budget showed that heat flux forcing dominates variations in mixed-layer temperature at MJO timescales throughout the entire domain, with solar heat flux anomalies making up the bulk of the net heat flux variations and latent heat flux playing a secondary role (Table IV.3). The other terms in the heat budget (horizontal and vertical advection and vertical entrainment), though at times significant, are generally second-order corrections that contribute little to the mixed-layer temperature tendency. However, we emphasize that these composites describe the average MJO, and thus do not preclude advection or entrainment becoming important during individual events. Strong anomalous wind stress and surface heat loss associated with an abrupt shift from suppressed to active MJO conditions over the Indian Ocean in phases 1–2 causes the mixed layer to deepen sharply. This induces significant vertical entrainment cooling throughout much of the basin (Figure IV.4d). This finding may help to resolve the discrepancy between previous studies that examined intraseasonal variations in the heat content of the central Indian Ocean. Han et al. (2007) found that latent heat flux and vertical entrainment control SST changes on MJO timescales,

whereas other authors have shown that heat flux variations alone, in particular shortwave radiation, dominate SST variations at MJO timescales (e.g. Duvel et al., 2004; Saji et al., 2006; Duvel and Vialard, 2007; Vialard et al., 2008; Jayakumar et al., 2010). Our results are more consistent with the latter studies as well as that of Vinayachandran and Saji (2008), who showed that entrainment cooling can also contribute if the thermocline is shallow.

Horizontal advection of heat, which at MJO timescales is primarily due to anomalous currents acting on the mean temperature gradient, is small throughout the domain with the exception of the central Pacific Ocean (Figure IV.4c). Our observations show that horizontal advection only becomes significant east of around 160°E. This illustrates that, moving east in the Pacific Ocean, the dominant forcing at MJO timescales shifts from the direct effects of atmospheric anomalies (Figure IV.2c,d) to the indirect effects of anomalous surface currents and equatorial waves (e.g. Duncan and Han, 2009). Vertical advection (not shown) is negligible: although strong wind stress curl anomalies can arise, producing anomalous Ekman pumping, vertical temperature gradients are generally small.

This study revealed that MLD variations on MJO timescales modulate the heat budget by up to 25–50% in the equatorial Indian and far western Pacific Oceans. This highlights the importance of correctly representing intraseasonal MLD variations in climate models in order to accurately simulate mixed-layer temperature, and thus air-sea interactions, associated with the MJO.

Finally, a close look at the sources of uncertainty showed that the choice of heat flux product can radically affect the heat budget. In order to correctly estimate mixed-layer temperature variations on the intraseasonal timescale, developing and validating more accurate heat flux products should be a priority.

IV.7 Appendix: Methodology for compositing Argo profile data

To estimate the composite MJO signal from Argo measurements, all profiles within a grid box defined by ($x_g \pm \Delta x$, $y_g \pm \Delta y$) and made within $\Delta t = \pm 12$ days of the significant MJO events during a given phase were used, and a model was fit to the data from those profiles. Although not a true oscillation, the MJO signal is roughly sinusoidal in shape over one cycle (e.g. Waliser et al., 2003; Schiller and Godfrey, 2003; Sato et al., 2010). Locally, this can be approximated as quadratic, so for the Argo-based fields we modeled each phase of the MJO signal at each grid point (x_g,y_g) using

$$A = A_o + \alpha_1 t' + \alpha_2 t'^2 + \beta x' + \gamma y' + \eta(\text{soi}). \tag{IV.4}$$

A robust linear least-squares fitting technique was used to evaluate this expression for each of the quantities A that were derived from the Argo profile data (i.e. T, h, $\partial T/\partial z$, ΔT). In Eq. IV.4, t' represents the time difference between each Argo profile and the nearest significant MJO event, and x' and y' give the distance from the center of the grid box (x_g,y_g). The fit yielded the following quantities: A_o, the composite variation of A associated with the MJO; α_1 and α_2, the MJO temporal tendency; β and γ, the MJO-related spatial variation of A over the grid box; and η, which accounted for the interannual variations in A. This last term was multiplied by the Southern Oscillation index (SOI; Trenberth, 1984), to which a 120-day lowpass filter had been applied to exclude high-frequency variations. It was necessary to include this term in Eq. (IV.4) to account for the interannual variations resulting from ENSO. However, because of the relatively short Argo time series, examining the effects of interannual variations on the MJO is beyond the scope of this study (e.g. Zhang and McPhaden, 2000).

The regression procedure is illustrated in Figure IV.7, which shows the Argo mixed-layer temperature data in the grid box centered at (x_g,y_g)=(82.5°E, 2.5°S). The top panels illustrate the typical scatter of profile locations for each phase of the MJO. The middle panels show the deseasonalized temperature of each profile in the grid box, plotted against the time from the profile to the nearest large MJO event (t'). The change in temperature through the progression of the MJO cycle is clear: in phase 1, the temperature anomaly is at a maximum; accordingly, the fit (Eq. IV.4) yields a positive inflection point (Figure IV.7b). Phases 2–3 show decreasing temperatures and, consistent with this, the fits to these data have negative slopes. The minimum MJO temperature anomaly occurs between phases 4 and 5, after which the temperature increases again in phases 6–7. For comparison, the bottom panels in Figure IV.7 show the satellite-derived SST from the Tropical Rainfall Measuring Mission (TRMM) Microwave Imager (TMI) in the same grid box. Although there are many more satellite SST observations than Argo profiles, the fits to both sets of data are similar, illustrating that the Argo dataset does a good job of capturing the MJO temperature signal. A comparison of the fits to the gridded SST with the fits to the Argo mixed-layer temperature, at all grid points and for all MJO phases, gives a significant correlation (R^2=0.5 for the mean and R^2=0.6 for the α_1 term). This shows that Argo data, though sparse, can effectively capture the variability associated with the canonical MJO.

The spatial and temporal derivatives of T and h that emerge from the fit in Eq. IV.4 provide the gradient terms used in the heat budget (Eq. IV.2). From the fits to mixed-layer temperature, α_1, β and γ give the terms $\partial T/\partial t$, $\partial T/\partial x$ and $\partial T/\partial y$, respectively. Similarly, $\partial h/\partial t$ was extracted from the fit to MLD as the α_1 term.

We found that a value of Δt=±12 days, corresponding to around half of the MJO cycle, yielded the best fits to the Argo data. For Δt <12 days, the fit was poor and the temporal evolution

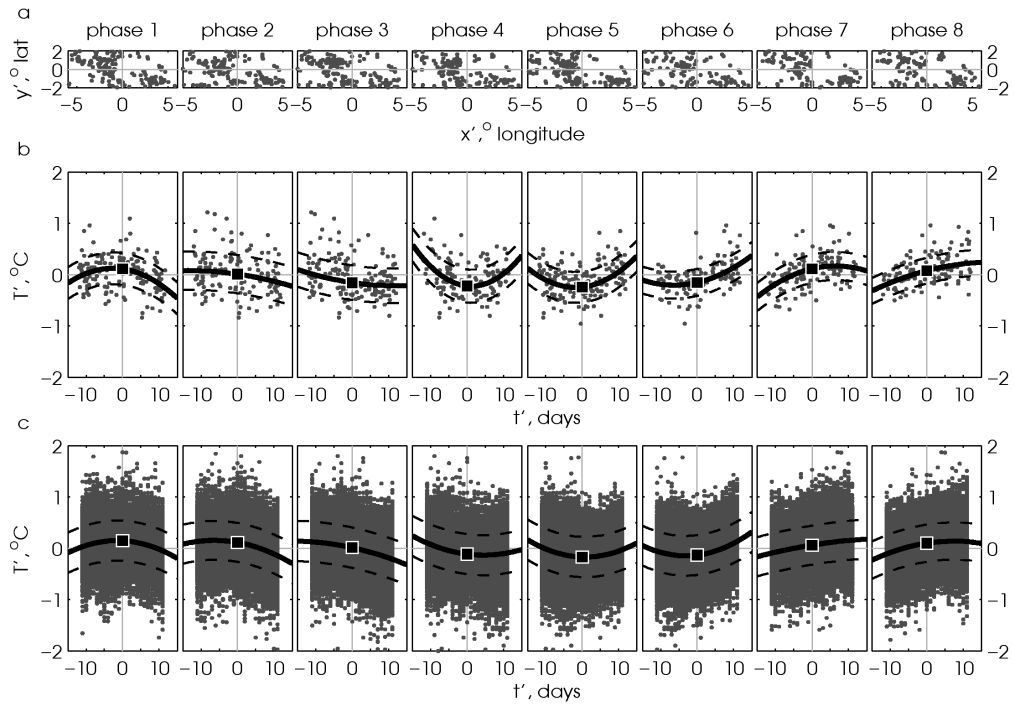

Figure IV.7: Example of regression to Argo data in a grid box (x_g,y_g=82.5° E,2.5° S). Top panels (a) show the geographical scatter of the Argo profiles in the grid box associated with each phase. Middle panels (b) show the deseasonalized mixed-layer temperature anomaly for each profile in the grid box, plotted against the time difference between the profile measurement and the nearest significant MJO event in that phase. The black squares and lines result from the robust fit to the data (Eq. [IV.4]), with the squares indicating the mean temperature anomaly (T_o) and the solid (dashed) lines showing the fit to the data (± the standard deviation). Bottom panels (c) show SST measurements in the same grid box derived from the TMI satellite product, with the fit and standard deviation of the data.

of the MJO signal was not well captured, and conversely for Δt much larger than 12 days, a quadratic fit was not able to adequately capture the variance. We used grid boxes defined by Δx=$\pm$6°and Δy=$\pm$2°, which maximizes the number of data points while capturing the spatial variation of the MJO. In most regions, the results of the analysis were not highly sensitive to the size of the grid box: generally, larger grid boxes resulted in smoother spatial patterns and composite signals with slightly smaller amplitudes. The exception was the far western Pacific Ocean, where the spatial scale of MJO variations is small.

IV.8 Acknowledgments

We gratefully acknowledge the many sources of data that made this study possible. The Argo data were collected and made freely available by the International Argo Project and the national programs that contribute to it (http://www.argo.ucsd.edu, http://argo.jcommops.org). Heat fluxes were obtained from Woods Hole Oceanographic Institution (OAFlux); ISCCP; NOAA / OAR / ESRL PSD, Boulder, Colorado (OLR and NCEP-2 reanalysis); ECMWF (ERA-I reanalysis); and the School of Marine Science and Technology, Tokai University (J-OFURO). The OSCAR data were obtained from the NASA Jet Propulsion Laboratory's Physical Oceanography DAAC and developed by Earth and Space Research. The GPCP combined precipitation data were developed and computed by the NASA/Goddard Space Flight Center's Laboratory for Atmospheres as a contribution to the GEWEX Global Precipitation Climatology Project. Chlorophyll-*a* data are available from the Giovanni online data system, which is developed and maintained by the NASA Goddard Earth Sciences Data and Information Services Center. TMI SST data are produced by Remote Sensing Systems and sponsored by the NASA Earth Science MEaSUREs DISCOVER Project and are available at www.remss.com. Wind data were provided by the Global Modeling and Assimilation Office at the NASA Goddard Space Flight Center, Greenbelt, MD, USA. The first author gratefully acknowledges assistance from the Australian-American Fulbright Commission and the NASA Earth and Space Science Fellowship program. This work was also supported by NSF grants OCE-0725476 (JS) and OCE-0850350 (SG).

Chapter IV, in full, is a manuscript in preparation for publication in the Journal of Climate. I was the primary researcher and author of this material, with contributions from co-authors Susan Wijffels, Sarah Gille, and Janet Sprintall.

V

Summary and discussion

In this thesis I have characterized some of the oceanic and atmospheric links between the tropical Indian and western Pacific Oceans via the Indonesian archipelago. In Chapter II, I showed that tsunami energy originating off the coast of Indonesia radiates into the Indonesian Throughflow (ITF) region. Using observations of two tsunamis made at different locations, this study revealed that the tsunami signal within the archipelago is a resonant amplification of the normal background response to the topography: refraction and reflection "pump" the incoming wave energy into local oscillations. This has implications for predicting local tsunami inundation within the archipelago, and highlights the need for higher-resolution bathymetric data within this region.

Chapters III and IV address energy at intraseasonal timescales. In Chapter III, I used satellite observations to track 40 intraseasonal Kelvin waves from their generation in the central Indian Ocean, eastward along the equator to Sumatra, then poleward along the coast and into the ITF region. In situ observations provided an unprecedented picture of the vertical temperature and velocity structure of Kelvin waves within two topographically-controlled ITF outflow passages. This study demonstrated that Kelvin waves generally propagate with phase speeds and vertical phase angles consistent with those expected of linear first- and second-mode baroclinic waves forced by intraseasonal winds. A large fraction of the incoming Kelvin wave signal enters the internal Indonesian seas, illustrating that remote Indian Ocean winds can influence ocean dynamics within the Indonesian archipelago. A linear wind-forced model experiment showed that wind anomalies along the coast of Sumatra, in addition to those in the central Indian Ocean, contribute significantly to the Kelvin wave signals seen in the ITF region.

In Chapter IV, I used measurements from the Argo profiling float data set, in combination with several satellite and reanalysis products, to characterize the signature of the Madden-Julian Oscillation (MJO) in upper ocean heat content throughout the tropical Indian and western Pacific

Oceans. By forming composites of heat flux forcing, horizontal and vertical advection, and vertical entrainment, I assessed the contribution of each of these terms to the temperature tendency of the mixed layer. This study revealed that heat flux anomalies dominate variations in mixed-layer temperature at MJO timescales, with variations in shortwave radiation making up the bulk of the net flux. To my knowledge this is the first study that has used in situ observations to quantify variations in mixed-layer depth (MLD) throughout the domain in which the MJO is active. I showed that MLD variations forced by the MJO can be large (>10 m amplitude), and that in the Indian Ocean these variations can modulate the heat flux forcing of the mixed layer by up to 50%. This suggests that it is important for models to accurately resolve MLD variations at MJO timescales in order to capture temperature variations associated with the MJO.

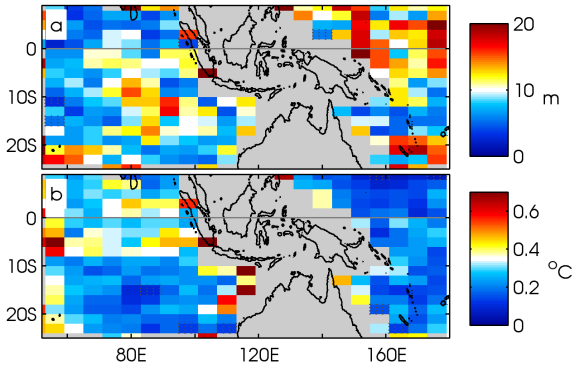

Figure V.1: Peak-to-peak amplitudes of the composite MJO signal, based on observations from Argo during boreal winter (November–April): (a) MLD; (b) mixed-layer temperature. Grid boxes where fewer than 40 profiles were available to estimate the composite signal have been masked out in grey.

Chapter IV brings to light a number of questions about oceanic MJO variations. This study revealed that MJO anomalies in mixed-layer depth and temperature have different spatial patterns (Figure V.1). Both temperature and MLD signals are significant in the central Indian Ocean, but while large temperature anomalies are found in the region northwest of Australia and south of Java, MLD variations there associated with the MJO are relatively weak. Conversely, MLD variations in the western Pacific Ocean are large but mixed-layer temperature varies little. This is curious in light of the fact that variations in both the temperature and the depth of the mixed layer are forced, to first order, by anomalies in surface heat flux and winds, and it illustrates that a "one size fits all" framework for understanding MJO upper ocean dynamics may not be appropriate. The spatial variations in MJO signals points to the importance of background conditions in determining stratification and thus controlling to what extent MJO atmospheric forcing affects the upper ocean.

In some regions, notably west of Sumatra and in the western Pacific warm pool, stratification is controlled by salinity as well as temperature and there exists a "barrier layer", an isothermal layer

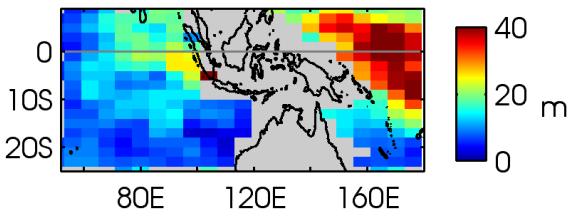

Figure V.2: Boreal winter (November–April) mean barrier-layer thickness estimated from Argo observations. Grid boxes where fewer than 40 profiles were used to estimate the signal are masked out in grey.

that lies below the salt-stratified mixed layer (Figure V.2). In the presence of a barrier layer, surface fluxes of heat, freshwater and momentum are confined to the mixed layer, which is thinner, and thus more reactive to surface forcing, than the isothermal layer (Godfrey and Lindstrom, 1989; Sprintall and Tomczak, 1992; Vialard and Delecluse, 1998; de Boyer Montégut et al., 2007). In addition, barrier layers prevent the entrainment of cold water into the mixed layer by reducing the vertical temperature gradient (Vialard and Delecluse, 1998). The presence or absence of a mean barrier layer may influence how MJO atmospheric anomalies impact the upper ocean and, by extension, may be important for air-sea coupling. Furthermore, it has been shown that the barrier layer itself can vary at MJO timescales (Anderson et al., 1996; Zhang and McPhaden, 2000; Cronin and McPhaden, 2002; Sato et al., 2010), but the mechanisms that control these variations have not been clearly identified and the impacts of barrier layer variations are not well understood. In future work, I will extend the approach used in Chapter IV to investigate regional variations in the mixed-layer response to MJO forcing and their links to background stratification. In particular, I aim to characterize variations in the barrier layer and explore their links to forcing from the MJO.

References

Adler, R., Susskind, J., Huffman, G., Bolvin, D., Nelkin, E., Chang, A., Ferraro, R., Gruber, A., Xie, P., Janowiak, J., et al., 2003: The version-2 global precipitation climatology project (GPCP) monthly precipitation analysis (1979–present). *J. Hydrometeor.*, **4**, 1147–1167.

Anderson, S., Weller, R., and Lukas, R., 1996: Surface buoyancy forcing and the mixed layer of the western Pacific warm pool: Observations and 1D model results. *J. Clim.*, **9**(12), 3056–3085.

Ardizzone, J., Atlas, R., Hoffman, R., Jusem, J., Leidner, S., and Moroni, D., 2009: New multiplatform ocean surface wind product available. *Eos Trans. AGU*, **90**, 27.

Arief, D., and Murray, S., 1996: Low-frequency fluctuations in the Indonesian throughflow through Lombok Strait. *J. Geophys. Res.*, **101**(C5).

Baba, T., Hirata, K., and Kaneda, Y., 2004: Tsunami magnitudes determined from ocean-bottom pressure gauge data around Japan. *Geophys. Res. Lett*, **31**.

Bellenger, H., and Duvel, J., 2009: An analysis of tropical ocean diurnal warm layers. *J. Clim.*, **22**(13), 3629–3646. doi:10.1175/2008JCLI2598.1.

Bernie, D., Guilyardi, E., Madec, G., Slingo, J., Woolnough, S., and Cole, J., 2008: Impact of resolving the diurnal cycle in an ocean–atmosphere GCM. Part 2: A diurnally coupled CGCM. *Clim. Dyn.*, **31**(7), 909–925. doi:10.1007/s00382-008-0429-z.

Bernie, D., Woolnough, S., Slingo, J., and Guilyardi, E., 2005: Modeling diurnal and intraseasonal variability of the ocean mixed layer. *J. Clim.*, **18**(8), 1190–1202.

Bonjean, F., and Lagerloef, G. S. E., 2002: Diagnostic model and analysis of the surface currents in the tropical Pacific Ocean. *J. Phys. Oceanogr.*, **32**(10), 2938–2954.

Cane, M., 1984: Modeling sea level during El Niño. *J. Phys. Oceanogr.*, **14**(12), 1864–1874.

Chong, J., Sprintall, J., Hautala, S., Morawitz, W., Bray, N., and Pandoe, W., 2000: Shallow throughflow variability in the outflow straits of Indonesia. *Geophys. Res. Lett.*, **27**(1), 125–128.

Cravatte, S., Picaut, J., and Eldin, G., 2003: Second and first baroclinic Kelvin modes in the equatorial Pacific at intraseasonal timescales. *J. Geophys. Res*, **108**(C8), 3266. doi: 10.1029/2002JC001511.

Cronin, M., and McPhaden, M., 1997: The upper ocean heat balance in the western equatorial Pacific warm pool during September–December 1992. *J. Geophys. Res*, **102**(C4), 8533–8553.

Cronin, M., and McPhaden, M., 2002: Barrier layer formation during westerly wind bursts. *J. Geophys. Res*, **107**(C12), 2101–2112.

de Boyer Montégut, C., Madec, G., Fischer, A., Lazar, A., and Iudicone, D., 2004: Mixed layer depth over the global ocean: An examination of profile data and a profile-based climatology. *J. Geophys. Res*, **109**, C12003.

de Boyer Montégut, C., Mignot, J., Lazar, A., and Cravatte, S., 2007: Control of salinity on the mixed layer depth in the world ocean: 1. General description. *J. Geophys. Res*, **112**, C06011.

Drushka, K., Sprintall, J., Gille, S., and Pranowo, W., 2008: Observations of the 2004 and 2006 Indian Ocean tsunamis from a pressure gauge array in Indonesia. *J. Geophys. Res*, **113**.

Ducet, N., Le Traon, P., and Reverdin, G., 2000: Global high-resolution mapping of ocean circulation from TOPEX/Poseidon and ERS-1 and -2. *J. Geophys. Res.*, **105**(C8), 19,477–19,498.

Duncan, B., and Han, W., 2009: Indian Ocean intraseasonal sea surface temperature variability during boreal summer: Madden-Julian Oscillation versus submonthly forcing and processes. *J. Geophys. Res*, **114**(C5), C05002. doi:10.1029/2008JC004958.

Durland, T., and Qiu, B., 2003: Transmission of subinertial Kelvin waves through a strait. *J. Phys. Oceanogr.*, **33**, 1337–1350.

Duvel, J., Roca, R., and Vialard, J., 2004: Ocean mixed layer temperature variations induced by intraseasonal convective perturbations over the Indian Ocean. *J. Atm. Sci.*, **61**(9), 1004–1023.

Duvel, J., and Vialard, J., 2007: Indo-Pacific sea surface temperature perturbations associated with intraseasonal oscillations of tropical convection. *J. Clim.*, **20**(13), 3056–3082. doi: 10.1175/JCLI4144.1.

Eriksen, C., Blumenthal, M., Hayes, S., and Ripa, P., 1983: Wind-generated equatorial Kelvin waves observed across the Pacific Ocean. *J. Phys. Oceanogr.*, **13**(9), 1622–1640.

Fine, I., Rabinovich, A., and Thomson, R., 2005: The dual source region for the 2004 Sumatra tsunami. *Geophys. Res. Lett*, **32**.

Flatau, M., Flatau, P., Phoebus, P., and Niiler, P., 1997: The feedback between equatorial convection and local radiative and evaporative processes: The implications for intraseasonal oscillations. *J. Atm. Sci.*, **54**, 2373–2386.

Fu, L., 2007: Intraseasonal variability of the equatorial Indian Ocean observed from sea surface height, wind, and temperature data. *J. Phys. Oceanogr.*, **37**(2). doi:10.1175/JPO3006.1.

Fujii, Y., and Satake, K., 2006: Source of the July 2006 West Java tsunami estimated from tide gauge records. *Geophys. Res. Lett.*, **33**(24), L24317.

Giese, B., and Harrison, D., 1990: Aspects of the Kelvin wave response to episodic wind forcing. *J. Geophys. Res.*, **95**(C5).

Godfrey, J., and Lindstrom, E., 1989: The heat budget of the equatorial western Pacific surface mixed layer. *J. Geophys. Res*, **94**(C6), 8007–8017.

Gordon, A., and Fine, R., 1996: Pathways of water between the Pacific and Indian oceans in the Indonesian seas. *Nature*, **379**(6561), 146–149.

Gordon, A., Susanto, R., Ffield, A., Huber, B., Pranowo, W., and Wirasantosa, S., 2008: Makassar Strait throughflow, 2004 to 2006. *Geophys. Res. Lett.*, **35**(24), L24605. doi:10.1029/2008GL036372.

Gower, J., 2005: Jason 1 detects the 26 December 2004 tsunami. *Eos Trans. AGU*, **86**(4), 37.

Gregg, W., 2008: Assimilation of SeaWiFS ocean chlorophyll data into a three-dimensional global ocean model. *J. Mar. Syst.*, **69**(3-4), 205–225.

Han, W., 2005: Origins and dynamics of the 90-day and 30–60-day variations in the equatorial Indian Ocean. *J. Phys. Oceanogr.*, **35**(5), 708–728.

Han, W., Shinoda, T., Fu, L., and McCreary, J., 2006: Impact of atmospheric intraseasonal oscillations on the Indian Ocean Dipole during the 1990s. *J. Phys. Oceanogr.*, **36**(4), 670–690.

Han, W., Yuan, D., Liu, W., and Halkides, D., 2007: Intraseasonal variability of Indian Ocean sea surface temperature during boreal winter: Madden-Julian Oscillation versus submonthly forcing and processes. *J. Geophys. Res*, **112**, C04001. doi:10.1029/2006JC003791.

Hansen, D., and Poulain, P., 1996: Quality control and interpolations of WOCE-TOGA drifter data. *J. Atmos. Ocean. Tech.*, **13**(4), 900–909. ISSN 1520-0426.

Hautala, S., Potemra, J., Sprintall, J., Chong, J., Pandoe, W., Bray, N., and Ilahude, A., 2001: Velocity structure and transport of the Indonesian Throughflow in the major straits restricting flow into the Indian Ocean. *J. Geophys. Res.*, **106**(C9).

Hayashi, Y., 2008: Extracting the 2004 Indian Ocean tsunami signals from sea surface height data observed by satellite altimetry. *J. Geophys. Res*, **113**.

Hendon, H., and Glick, J., 1997: Intraseasonal air–sea interaction in the tropical Indian and Pacific Oceans. *J. Clim.*, **10**, 647–661.

Hendon, H., and Salby, M., 1994: The life cycle of the Madden-Julian Oscillation. *J. Atmosph. Sci.*, **51**(15), 2225–2237.

Horii, T., Hase, H., Ueki, I., and Masumoto, Y., 2008: Oceanic precondition and evolution of the 2006 Indian Ocean dipole. *Geophys. Res. Lett.*, **35**(3). doi:10.1029/2007GL032464.

Inness, P., and Slingo, J., 2003: Simulation of the Madden–Julian oscillation in a coupled general circulation model. Part I: Comparison with observations and an atmosphere-only GCM. *J. Clim.*, **16**, 345–364.

Iskandar, I., Mardiansyah, W., Masumoto, Y., and Yamagata, T., 2005: Intraseasonal Kelvin waves along the southern coast of Sumatra and Java. *J. Geophys. Res.*, **110**(C04013). doi: 10.1029/2004JC002508.

Iskandar, I., Masumoto, Y., and Mizuno, K., 2009: Subsurface equatorial zonal current in the eastern Indian Ocean. *J. Geophys. Res*, **114**(C6), C06005. doi:10.1029/2008JC005188.

Jayakumar, A., Vialard, J., Lengaigne, M., Gnanaseelan, C., McCreary, J. P., and Kumar, P., 2010: Processes controlling the surface temperature signature of the Madden-Julian Oscillation in the thermocline ridge of the Indian Ocean. *Clim. Dyn.* Submitted.

Johnson, E., Bonjean, F., Lagerloef, G., Gunn, J., and Mitchum, G., 2007: Validation and error analysis of OSCAR sea surface currents. *J. Atmosph. Ocean. Tech.*, **24**(4), 688–701.

Johnson, E., and McPhaden, M., 1993: Structure of intraseasonal Kelvin waves in the equatorial Pacific Ocean. *J. Phys. Oceanogr.*, **23**(4), 608–625.

Johnson, H., and Garrett, C., 2006: What fraction of a Kelvin wave incident on a narrow strait is transmitted? *J. Phys. Oceanogr.*, **36**(5), 945–954.

Kanamitsu, M., Ebisuzaki, W., Woollen, J., Yang, S., Hnilo, J., Fiorino, M., and Potter, G., 2002: NCEP-DOE AMIP-II Reanalysis (R-2). *Bull. Am. Meteorol. Soc.*, **83**(11), 1631–1643.

Kessler, W., and McPhaden, M., 1995: Oceanic equatorial waves and the 1991–93 El Niño. *J. Clim.*, **8**(7), 1757–1774.

Kessler, W., McPhaden, M., and Weickmann, K., 1995: Forcing of intraseasonal Kelvin waves in the equatorial Pacific. *J. Geophys. Res.*, **100**(C6), 10613–10631.

Kowalik, Z., Knight, W., Logan, T., and Whitmore, P., 2005: Numerical modeling of the global tsunami: Indonesian tsunami of 26 December 2004. *Sci. Tsunami Hazards*, **23**(1), 40–56.

Kubota, M., Iwasaka, N., Kizu, S., Konda, M., and Kutsuwada, K., 2002: Japanese ocean flux data sets with use of remote sensing observations (J-OFURO). *J. Oceanogr.*, **58**(1), 213–225.

Kumar, B. P., Vialard, J., Lengaigne, M., Murty, V., and McPhaden, M., 2010: TropFlux: Air-Sea Fluxes for the Global Tropical Oceans – Description and evaluation against observations. *Clim. Dyn.* Submitted.

Large, W., McWilliams, J., and Doney, S., 1994: Oceanic vertical mixing: A review and a model with a nonlocal boundary layer parameterization. *Rev. Geophys.*, **32**(4), 363–403.

Lau, W., and Waliser, D., 2005: *Intraseasonal variability in the atmosphere-ocean climate system*. Springer, Heidelberg, Germany.

Lavigne, F., Gomez, C., Giffo, M., Wassmer, P., Hoebreck, C., Mardiatno, D., Prioyono, J., and Paris, R., 2007: Field observations of the 17 July 2006 Tsunami in Java. *Nat. Hazards Earth Syst.*, **7**, 177–183.

Lay, T., Kanamori, H., Ammon, C., Nettles, M., Ward, S., Aster, R., Beck, S., Bilek, S., Brudzinski, M., Butler, R., et al., 2005: The great Sumatra-Andaman earthquake of 26 December 2004. *Science*, **308**(5725), 1127.

Liebmann, B., and Smith, C. A., 1996: Description of a complete (interpolated) outgoing longwave radiation dataset. *Bull. Amer. Met. Soc.*, **77**, 1275–1277.

Lucas, L., Waliser, D., and Murtugudde, R., 2010: Mechanisms governing sea surface temperature anomalies in the eastern tropical Pacific Ocean associated with the boreal winter Madden-Julian Oscillation. *J. Geophys. Res.*, **115**(C5), C05012. doi:10.1029/2009JC005450.

Lukas, R., and Lindstrom, E., 1991: The mixed layer of the western equatorial Pacific Ocean. *J. Geophys. Res.*, **96**, 3343–3357.

Luyten, J., and Roemmich, D., 1982: Equatorial currents at semi-annual period in the Indian Ocean. *J. Phys. Oceanogr.*, **12**(5), 406–413.

Madden, R., and Julian, P., 1971: Detection of a 40–50 Day Oscillation in the Zonal Wind in the Tropical Pacific. *J. Atm. Sci.*, **28**(5), 702–708.

Madden, R., and Julian, P., 1972: Description of global-scale circulation cells in the tropics with a 40-50 day period. *J. Atm. Sci.*, **29**(6), 1109–1123.

Maloney, E., and Kiehl, J., 2002: MJO-related SST variations over the tropical eastern Pacific during Northern Hemisphere summer. *J. Clim.*, **15**(6), 675–689.

Maloney, E., and Sobel, A., 2004: Surface fluxes and ocean coupling in the tropical intraseasonal oscillation. *J. Clim.*, **17**(22), 3717–3720.

Marks, K., and Smith, W., 2006: An evaluation of publicly available global bathymetry grids. *Mar. Geophys. Res.*, **27**(1), 19–34.

Masumoto, Y., Hase, H., Kuroda, Y., Matsuura, H., and Takeuchi, K., 2005: Intraseasonal variability in the upper layer currents observed in the eastern equatorial Indian Ocean. *Geophys. Res. Lett.*, **32**(2), L02607.

McCreary, J., 1983: A model of tropical ocean-atmosphere interaction. *Mon. Weath. Rev.*, **111**(2), 370–387.

McCreary, J., 1984: Equatorial beams. *J. Mar. Res.*, **42**(2), 395–430.

McPhaden, M., Proehl, J., and Rothstein, L., 1986: The interaction of equatorial Kelvin waves with realistically sheared zonal currents. *J. Phys. Oceanogr.*, **16**(9), 1499–1515.

McPhaden, M. J., 2002: Mixed layer temperature balance on intraseasonal timescales in the equatorial Pacific Ocean. *J. Clim.*, **15**(18), 2632–2647.

Merrifield, M., Firing, Y., Aarup, T., Agricole, W., Brundrit, G., Chang-Seng, D., Farre, R., Kilonsky, B., Knight, W., Kong, L., et al., 2005: Tide gauge observations of the Indian Ocean tsunami, December 26, 2004. *Geophys. Res. Lett.*, **32**(9), L09603.

Molcard, R., Fieux, M., and Syamsudin, F., 2001: The throughflow within Ombai Strait. *Deep Sea Res., Part I*, **48**(5), 1237–1253.

Morel, A., and Antoine, D., 1994: Heating rate within the upper ocean in relation to its bioâĂŞoptical state. *J. Phys. Oceanogr.*, **24**(7), 1652–1665.

Nagarajan, B., Suresh, I., Sundar, D., Sharma, R., Lal, A., Neetu, S., Shenoi, S., Shetye, S., and Shankar, D., 2006: The great tsunami of 26 December 2004: A description based on tide gauge data from Indian subcontinent and surrounding areas. *Earth Planets Space*, **58**, 211–215.

Neetu, S., Suresh, I., Shankar, R., Shankar, D., Shenoi, S., Shetye, S., Sundar, D., and Nagarajan, B., 2005: Comment on "The Great Sumatra-Andaman Earthquake of 26 December 2004". *Science*, **310**(5753), 1431a.

Pawlowicz, R., Beardsley, B., and Lentz, S., 2002: Classical tidal harmonic analysis including error estimates in MATLAB using T_TIDE. *Comput. Geosci.*, **28**(8), 929–937.

Peter, B. N., and Mizuno, K., 2000: Annual cycle of steric height in the Indian Ocean estimated from the thermal field. *Deep Sea Res. I*, **47**(7), 1351 – 1368.

Potemra, J., Hautala, S., Sprintall, J., and Pandoe, W., 2002: Interaction between the Indonesian Seas and the Indian Ocean in observations and numerical models. *J. Phys. Oceanogr.*, **32**(6), 1838–1854.

Potemra, J., Sprintall, J., Hautala, S., and Pandoe, W., 2003: Observed estimates of convergence in the Savu Sea, Indonesia. *J. Geophys. Res.*, **108**(C1), 3001.

Price, J., Weller, R., and Pinkel, R., 1986: Diurnal cycling: Observations and models of the upper ocean response to diurnal heating, cooling, and wind mixing. *J. Geophys. Res.*, **91**(C7), 8411–8427.

Qiu, B., Mao, M., and Kashino, Y., 1999: Intraseasonal variability in the Indo-Pacific Throughflow and the regions surrounding the Indonesian Seas. *J. Phys. Oceanogr.*, **29**(7), 1599–1618.

Qu, T., Du, Y., J.P. McCreary, J., Meyers, G., and Yamagata, T., 2008: Buffering effect and its related ocean dynamics in the Indonesian throughflow region. *J. Phys. Oceanogr.*, **38**(2). doi: 10.1175/2007JPO3759.1.

Qu, T., and Meyers, G., 2005: Seasonal characteristics of circulation in the southeastern tropical Indian Ocean. *J. Phys. Oceanogr.*, **35**(2), 255–267. doi:10.1175/JPO-2682.1.

Rabinovich, A., and Thomson, R., 2007: The 26 December 2004 Sumatra tsunami: Analysis of tide gauge data from the world ocean Part 1. Indian Ocean and South Africa. *Pure Appl. Geophys.*, 261–308.

Rao, S., Masson, S., Luo, J., Behera, S., and Yamagata, T., 2007: Termination of Indian Ocean Dipole events in a coupled general circulation model. *J. Clim.*, **20**(13), 3018–3035. doi: 10.1175/JCLI4164.1.

Resplandy, L., Vialard, J., Lévy, M., Aumont, O., and Dandonneau, Y., 2009: Seasonal and intraseasonal biogeochemical variability in the thermocline ridge of the southern tropical Indian Ocean. *J. Geophys. Res*, **114**(C7), C07024. doi:10.1029/2008JC005246.

Roemmich, D., and Gilson, J., 2009a: The 2004-2008 mean and annual cycle of temperature, salinity, and steric height in the global ocean from the argo program. *Prog. Oceanogr.*, **82**(2), 81 – 100.

Roemmich, D., and Gilson, J., 2009b: The 2004-2008 mean and annual cycle of temperature, salinity, and steric height in the global ocean from the Argo program. *Prog. Oceanogr.*, **82**(2), 81–100.

Romea, R., and Allen, J., 1983: On vertically propagating coastal Kelvin waves at low latitudes. *J. Phys. Oceanogr.*, **13**(7), 1241–1254.

Saji, N., Goswami, B., Vinayachandran, P., and Yamagata, T., 1999: A dipole mode in the tropical Indian Ocean. *Nature*, **401**(6751), 360–363.

Saji, N., Xie, S., and Tam, C., 2006: Satellite observations of intense intraseasonal cooling events in the tropical south Indian Ocean. *Geophys. Res. Lett*, **33**, L14704. doi:10.1029/2006GL026525.

Satake, K., 1988: Effects of bathymetry on tsunami propagation: Application of ray tracing to tsunamis. *Pure Appl. Geophys.*, **126**(1), 27–36.

Sato, N., Yoneyama, K., Takayabu, Y., Shirooka, R., and Yoshizaki, M., 2010: Variability of the oceanic surface and subsurface layers in the warm pool associated with the atmospheric northward-propagating intraseasonal variability. *Deep Sea Res. II*. In press.

Schiller, A., and Godfrey, J., 2003: Indian Ocean intraseasonal variability in an ocean general circulation model. *J. Clim.*, **16**, 21–39.

Schiller, A., Wijffels, S. E., Sprintall, J., Molcard, R., and Oke, P. R., 2010: Pathways of Intraseasonal Variability in the Indonesian Throughflow Region. *Dyn. Atmos. Oceans*, **50**(2), 174–200.

Schneider, N., 1998: The Indonesian Throughflow and the global climate system. *J. Clim.*, **11**(4), 676–689.

Seo, K.-H., Wang, W., Gottschalck, J., Zhang, Q., Schemm, J.-K. E., Higgins, W. R., and Kumar, A., 2009: Evaluation of MJO forecast skill from several statistical and dynamical forecast models. *J. Clim.*, **22**(9), 2372–2388.

Shinoda, T., and Hendon, H., 1998: Mixed layer modeling of intraseasonal variability in the tropical western Pacific and Indian Oceans. *J. Clim.*, **11**(10), 2668–2685.

Shinoda, T., Hendon, H., and Glick, J., 1998: Intraseasonal variability of surface fluxes and sea surface temperature in the tropical western Pacific and Indian Oceans. *J. Clim.*, **11**(7), 1685–1702.

Simmons, A., Uppala, S., Dee, D., and Kobayashi, S., 2007: ERA-Interim: New ECMWF reanalysis products from 1989 onwards. *ECMWF Newsletter*, **110**, 25–35.

Smith, W., and Sandwell, D., 1997: Global sea floor topography from satellite altimetry and ship depth soundings. *Science*, **277**(5334), 1956.

Smith, W., Scharroo, R., Titov, V., Arcas, D., and Arbic, B., 2005: Satellite altimeters measure tsunami. *Oceanography*, **18**(2), 11.

Song, Q., Gordon, A., and Visbeck, M., 2004: Spreading of the Indonesian throughflow in the Indian Ocean. *J. Phys. Oceanogr.*, **34**(4), 772–792.

Sprintall, J., Chong, J., Syamsudin, F., Morawitz, W., Hautala, S., Bray, N., and Wijffels, S., 1999: Dynamics of the South Java Current in the Indo-Australian Basin. *Geophys. Res. Lett.*, **26**(16), 2493–2496.

Sprintall, J., Gordon, A., Murtugudde, R., and Susanto, R. D., 2000: A semiannual Indian Ocean forced Kelvin wave observed in the Indonesian seas in May 1997. *J. Geophys. Res.*, **105**(C7), 17217–17230.

Sprintall, J., and McPhaden, M., 1994: Surface layer variations observed in multiyear time series measurements from the western equatorial Pacific. *J. Geophys. Res*, **99**, 963–979.

Sprintall, J., and Tomczak, M., 1992: Evidence of the barrier layer in the surface layer of the tropics. *J. Geophys. Res.*, **97**(C5), 7305–7316.

Sprintall, J., Wijffels, S., Gordon, A., Ffield, A., Molcard, R., Susanto, R., Soesilo, I., Sopaheluwakan, J., Surachman, Y., and van Aken, H., 2004: INSTANT: A New International Array to Measure the Indonesian Throughflow. *EOS Transactions, AGU*, **85**(39).

Sprintall, J., Wijffels, S., Molcard, R., and Jaya, I., 2009: Direct estimates of the Indonesian Throughflow entering the Indian Ocean: 2004–2006. *J. Geophys. Res.*, **114**(C07001). doi: 10.1029/2008JC005257.

Stammer, D., and Wunsch, C., 1999: Preliminary assessment of the accuracy and precision of TOPEX/POSEIDON altimeter data with respect to the large-scale ocean circulation. *J. Geophys. Res.*, **99**(C12), 24,584âĂŞ–24,604.

Stein, S., and Okal, E., 2005: Seismology: Speed and size of the Sumatra earthquake. *Nature*, **434**(7033), 581–582.

Sweeney, C., Gnanadesikan, A., Griffies, S., Harrison, M., Rosati, A., and Samuels, B., 2005: Impacts of shortwave penetration depth on large-scale ocean circulation and heat transport. *J. Phys. Oceanogr.*, **35**(6), 1103–1119.

Syamsudin, F., Kaneko, A., and Haidvogel, D., 2004: Numerical and observational estimates of Indian Ocean Kelvin wave intrusion into Lombok Strait. *Geophys. Res. Lett.*, **31**(L24307). doi: 10.1029/2004GL021227.

Thompson, R., 1983: Low-pass filters to suppress inertial and tidal frequencies. *J. Phys. Oceanogr.*, **13**(6), 1077–1083.

Torrence, C., and Compo, G., 1998: A practical guide to wavelet analysis. *Bull. Am. Meteorol. Soc.*, **79**(1), 61–78.

Trenberth, K. E., 1984: Signal versus noise in the Southern Oscillation. *Mon. Weather Rev.*, **112**(2), 326–332.

van Aken, H. M., Brodjonegoro, I. S., and Jaya, I., 2009: The deep-water motion through the Lifamatola Passage and its contribution to the Indonesian throughflow. *Deep Sea Res. I*, **56**(8), 1203–1216. doi:10.1016/j.dsr.2009.02.001.

Van Dorn, W., 1984: Some tsunami characteristics deducible from tide records. *J. Phys. Oceanogr.*, **14**(2), 353–363.

Vialard, J., and Delecluse, P., 1998: An OGCM Study for the TOGA decade. Part I: Role of salinity in the physics of the Western Pacific fresh pool. *J. Phys. Oceanogr.*, **28**(6), 1071–1088.

Vialard, J., Foltz, G., McPhaden, M., Duvel, J., and de Boyer Montégut, C., 2008: Strong Indian Ocean sea surface temperature signals associated with the Madden-Julian Oscillation in late 2007 and early 2008. *Geophys. Res. Lett.*, **35**. doi:10.1029/2008GL035238.

Vinayachandran, P., Kurian, J., and Neema, C., 2007: Indian Ocean response to anomalous conditions in 2006. *Geophys. Res. Lett.*, **34**(15).

Vinayachandran, P., and Saji, N., 2008: Mechanisms of south Indian Ocean intraseasonal cooling. *Geophys. Res. Lett.*, **35**(23), L23607. doi:10.1029/2008GL035733.

Waliser, D., Lau, K., and Kim, J., 1999: The influence of coupled sea surface temperatures on the Madden–Julian oscillation: A model perturbation experiment. *J. Atm. Sci.*, **56**, 333–358.

Waliser, D., Murtugudde, R., and Lucas, L., 2003: Indo-Pacific Ocean response to atmospheric intraseasonal variability: 1. Austral summer and the Madden-Julian Oscillation. *J. Geophys. Res*, **108**, 3160. doi:10.1029/2002JC001620.

Waliser, D. E., Murtugudde, R., Strutton, P., and Strutton, P., 2005: Subseasonal organization of ocean chlorophyll: Prospects for prediction based on the Madden-Julian Oscillation. *Geophys. Res. Lett.*, **32**(L23602). doi:10.1029/2005GL024300.

Wheeler, M., and Hendon, H., 2004: An all-season real-time multivariate MJO index: Development of an index for monitoring and prediction. *Mon. Weather Rev.*, **132**, 1917–1932.

Wijffels, S., and Meyers, G., 2004: An intersection of oceanic waveguides: variability in the Indonesian Throughflow region. *J. Phys. Oceanogr.*, **32**(5), 1232–1253.

Woolnough, S., Vitart, F., and Balmaseda, M., 2007: The role of the ocean in the Madden-Julian Oscillation: Implications for MJO prediction. *Q. J. Roy. Meteor. Soc.*, **132**(622), 117–128.

Woolnough, S. J., Slingo, J. M., and Hoskins, B. J., 2000: The relationship between convection and sea surface temperature on intraseasonal timescales. *J. Clim.*, **13**(12), 2086–2104. doi: 10.1175/1520-0442(2000).

Wyrtki, K., 1973: An equatorial jet in the Indian Ocean. *Science*, **181**(4096), 262–264.

Yu, L., and Rienecker, M., 1999: Mechanisms for the Indian Ocean warming during the 1997-98 El Niño. *Geophys. Res. Lett.*, **26**(6), 735–738.

Yu, L., and Rienecker, M., 2000: Indian Ocean warming of 1997–1998. *J. Geophys. Res.*, **105**(C7).

Yu, L., and Weller, R., 2007: Objectively analyzed air-sea heat fluxes for the global ice-free oceans (1981-2005). *Bull. Am. Meteorol. Soc.*, **88**(4), 527–539.

Zhang, C., 2005: Madden-Julian Oscillation. *Rev. Geophys*, **43**, 1–36.

Zhang, C., and Dong, M., 2004: Seasonality in the Madden–Julian Oscillation. *J. Clim.*, **17**(16), 3169–3180.

Zhang, C., and McPhaden, M. J., 2000: Intraseasonal surface cooling in the equatorial western Pacific. *J. Clim.*, **13**(13), 2261–2276.

Zhang, G. J., and McPhaden, M. J., 1995: The Relationship between sea surface temperature and latent heat flux in the equatorial Pacific. *J. Clim.*, **8**(3), 589–605.